DYNAMIC MODELLING AND ANALYSIS OF GUN TURRET ELEVATION DRIVE SYSTEM

A THESIS SUBMITTED TO
THE GRADUATE SCHOOL OF NATURAL AND APPLIED SCIENCES
OF
MIDDLE EAST TECHNICAL UNIVERSITY

BY

ÇAĞIL ÇİLOĞLU

IN PARTIAL FULFILLMENT OF THE REQUIREMENTS
FOR
THE DEGREE OF MASTER OF SCIENCE
IN
MECHANICAL ENGINEERING

JUNE 2016

Approval of the thesis:

DYNAMIC MODELLING AND ANALYSIS OF GUN TURRET ELEVATION DRIVE SYSTEM

submitted by **ÇAĞIL ÇİLOĞLU** in partial fulfillment of the requirements for the degree of **Master of Science in Mechanical Engineering Department, Middle East Technical University** by**,**

Prof. Dr. Gülbin Dural ÜNVER
Dean, Graduate School of **Natural and Applied Sciences** _____

Prof. Dr. Tuna BALKAN
Head of Department, **Mechanical Engineering** _____

Prof. Dr. M.A. Sahir Arıkan
Supervisor, **Mechanical Engineering Dept., METU** _____

Mr. Oykun Eren (MSc.)
Co-Supervisor, **FNSS Savunma Sistemleri A.Ş.** _____

Examining Committee Members:

Prof. Dr. Metin AKKÖK
Mechanical Engineering Dept., METU _____

Prof. Dr. M.A. Sahir ARIKAN
Mechanical Engineering Dept., METU _____

Prof. Dr. Tuna BALKAN
Mechanical Engineering Dept., METU _____

Assist. Prof. Dr. Ulaş YAMAN
Mechanical Engineering Dept., METU _____

Assist. Prof. Dr. Ender YILDIRIM
Mechatronics Engineering Dept., ÇANKAYA UNI _____

Date: _____

I hereby declare that all information in this document has been obtained and presented in accordance with academic rules and ethical conduct. I also declare that, as required by these rules and conduct, I have full cited and referenced all material and results that are not original to this work.

Name, Last name: Çağıl ÇİLOĞLU

Signature:

ABSTRACT

DYNAMIC MODELLING AND ANALYSIS OF GUN TURRET ELEVATION DRIVE SYSTEM

Çiloğlu, Çağıl

M.Sc., Department of Mechanical Engineering

Supervisor: Prof. Dr. M.A. Sahir Arıkan

Co-Supervisor: Mr. Oykun Eren

June 2016, 125 pages

In this thesis, dynamic models for the elevation axis of a gun turret are developed by using MATLAB/Simulink and the multi-body dynamics software MSC-Adams. The developed models include the driveline stiffnesses of individual components as well as the viscous damping of the bearings in the elevation drive-train. State space representations of gun turret model with different degrees of freedoms are presented and compared. Both time and frequency domain analyses are conducted in order to get a basic idea about the behavior of the system.

The theory of gear dynamics is introduced as a first step for integrating the flexibilities of gear pairs into the gun turret model. For this purpose, different gear mesh stiffness and gear mesh damping models available in the literature are investigated. The elastic contact forces in the gear-train are computed by taking into account the gear deformations due to bending, shear, foundation deflection and Hertzian contact of the gear teeth. The existing Hertzian contact models in the literature are compared and differences between them are investigated.

With the help of the contact parameters, the gear dynamics model is constructed that takes into account backlash and gear impact. Furthermore, a realistic friction model which takes into account the lubricant characteristics is added to the developed gear dynamics model. The effect of gear dynamics on the overall

performance characteristics is then investigated in both time and frequency domains. A controller is designed via MATLAB for tracking a reference input speed by using the developed model.

All of the analytical formulations that are developed in MATLAB-Simulink, are verified by the multi-body dynamics software MSC-Adams.

Finally, dynamic effects of the compliant adjustment type anti-backlash mechanism, which is commonly used in gun turret drives, is investigated by means of the developed multibody dynamics model. Various target tracking scenarios are constructed and different simulations are conducted in MSC-Adams.

Keywords: Gun turret dynamics, gear dynamics, target tracking, backlash, multi-body dynamics, gear mesh stiffness, gear friction, compliant adjustment type anti-backlash mechanisms

ÖZ

SİLAH KULESİ YÜKSELİŞ TAHRİK SİSTEMİNİN DİNAMİK MODELLENMESİ VE ANALİZİ

Çiloğlu, Çağıl
Yüksek Lisans, Makina Mühendisliği Bölümü
Tez Danışmanı:Prof. Dr. M.A. Sahir Arıkan
Tez Yardımcı Danışmanı: Oykun Eren
Haziran 2016, 125 sayfa

Tez kapsamında, silah kulesi yükseliş ekseni için MATLAB/Simulink ve çoklu cisim dinamiği yazılımı MSC-Adams kullanılarak dinamik modeller geliştirilmiştir. Modelleme esnasında eksen tahriki için kullanılan elemanların esneklikleri ile, rulmanlardaki viskoz sönümleme göz önünde bulundurulmuştur. Silah kulesini temsilen oluşturulan farklı serbestlik derecelerine sahip dinamik modeller, durum uzayı modeli şeklinde tanımlanmış ve birbirleri ile karşılaştırma amaçlı kullanılmıştır. Sistem hakkında temel fikir sahibi olma amacı ile zaman ve frekans düzlemlerinde analizler sunulmuştur.

Diş/dişli esnekliklerini hesaplamalara dahil edebilmek için dişlilerin dinamik davranışlarını içeren bir model geliştirilmiştir. Modelleme esnasında, dişlilerin arasındaki yay direngenliği ve sönümleme katsayısı ile ilgili farklı yaklaşımlar karşılaştırılmıştır. Diş teması sırasında oluşan deformasyonlar bulunurken bir diş üzerindeki eğilme, kesme ve dişli gövdesindeki deformasyonlar ile Hertz deformasyonları ayrı ayrı hesaplanmıştır. Literatürdeki farklı Hertz teması modelleri kullanılarak hesaplamalar yapılmış, sonuçlar karşılaştırılmış ve aralarındaki farklar gözlemlenmiştir.

Açıklanan temas parametreleri kullanılarak oluşturulan dişli dinamiği dinamik modelinde, diş boşluğu ve darbe yükleri hesaba katılmıştır. Ayrıca

kullanılan yağlayıcının özelliklerine bağlı, gerçekçi bir dişli sürtünme modeli oluşturulan dinamik modele dahil edilmiştir. Geliştirilen dişli dinamiği modeli, silah kulesi modeline entegre edilerek dişlilerdeki esnekliklerin tüm sisteme olan etkileri zaman ve frekans düzlemlerinde incelenmiştir. Oluşturulan model ve MATLAB kullanılarak, verilen bir referans hız girdisini takip eden bir kontrolcü tasarlanmıştır.

MATLAB ve Simulink ortamlarında oluşturulan tüm modeller çoklu cisim benzetim yazılımı MSC-Adams kullanılarak doğrulanmıştır.

Son olarak; silah kulelerinde yaygın olarak kullanılan esnek ayarlamalı tipte bir diş boşluğu alma mekanizmasının sistem üzerindeki etkileri, geliştirilmiş olan çoklu cisim modeli kullanılarak araştırılmıştır.

Anahtar Kelimeler: Silah kulesi dinamiği, dişli dinamiği, hedef takibi, diş boşluğu, çoklu cisim dinamiği, dişli direngenliği, dişli sürtünmesi, esnek ayarlamalı diş boşluğu alma mekanizması

To My Parents

Fatma and Tahsin Çiloğlu

ACKNOWLEDGEMENTS

I would like to express my gratitude to my supervisor Prof. Dr. M.A. Sahir Arıkan for his supervision, patience and helpful critics throughout the thesis.

I would also like to thank my co-advisor and department manager Mr. Oykun Eren for his engineering insight to problems and for his valuable comments on MSC Adams.

I sincerely appreciate the invaluable comments of my colleague Ergin Kurtulmuş from weapon systems development group.

I acknowledge FNSS Savunma Sistemleri A.Ş. for allowing me to pursue a graduate degree while working as a full time R&D engineer.

My special thanks are due to my dear girlfriend Neslihan Taş, who kept me going at difficult times.

Finally, last but not least, I would like to thank Fatma and Tahsin Çiloğlu for each and every page of this thesis. Without a doubt, this work would not have been completed if it were not for their endless support, encouragement and belief in me.

TABLE OF CONTENTS

ABSTRACT v

ÖZ vii

ACKNOWLEDGEMENTS x

TABLE OF CONTENTS xi

LIST OF TABLES xiv

LIST OF FIGURES xv

LIST OF SYMBOLS xix

CHAPTER 1 1

1 INTRODUCTION 1

1.1 Introduction to the Problem 1

1.2 Review of Literature 3

1.3 Objective and Scope of the Thesis 11

2 SIMPLIFIED DYNAMIC MODEL OF THE GUN TURRET ELEVATION AXIS 13

2.1 Introduction 13

2.2 Dynamic Modeling 13

2.3 Lagrange Equations of Motions 16

2.4 Open Loop System Simulations 20

3 DETERMINATION OF CONTACT PARAMETERS FOR GEAR DYNAMICS 25
3.1 Introduction 25
3.2 Gear Mesh Stiffness 25
3.2.1 Local Deflection Models 26
3.2.2 Gear Body Deflection Models 37
3.3 Gear Damping Coefficient 46
4 FIXED CENTER DISTANCE GEAR DYNAMICS 49
4.1 Introduction 49
4.2 Equations of Motion of a Gear Pair with Backlash-Forward Dynamics 49
4.3 Development of MATLAB-Simulink and MSC-Adams models 54
4.4 Simulation Results for Forward Dynamics 56
4.4.1 Free Oscillations 56
4.4.2 Constant Load 58
4.5 Incorporation of Friction into Model 61
4.6 Equations of Motions for Inverse Dynamics 64
4.7 Simulation Results for Inverse Dynamics 67
5 DYNAMIC MODELLING OF THE GUN TURRET ELEVATION AXIS 73
5.1 Incorporation of Gear Dynamics to the Model 73
5.2 The Improved Dynamic Model in Simulink 75
5.3 Construction of the Dynamic Model in MSC-Adams 76
5.4 Contact friction in MSC-Adams 78

5.5 Integration of the anti-backlash mechanism 79
5.6 Target Tracking in MATLAB - Simulink 81
5.7 Target Tracking in MSC-Adams 82
5.8 Simulation Results 83
5.8.1 Open Loop Frequency Domain Results in MATLAB-Simulink 83
5.8.2 Open Loop Time Domain Results in MATLAB-Simulink 85
5.8.3 Closed Loop Results in MATLAB-Simulink 87
5.8.4 MSC-Adams Verifications 91
5.8.5 Simulations with Anti-backlash Mechanism 96
6 CONCLUSION AND FUTURE WORK 99
6.1 Conclusions 99
6.2 Future Work 102
REFERENCES 103
APPENDIX A 107
APPENDIX B 111
APPENDIX C 123

LIST OF TABLES

TABLES

Table 1 Gun turret parameters 20
Table 2 Example gear pair parameters 34
Table 3 Simulated gear parameters for inverse dynamics 70
Table 4 System parameters 77

LIST OF FIGURES

FIGURES

Figure 1-1 Effect of stabilization [1] 1
Figure 1-2 Backlash definition along the line of action 2
Figure 1-3 Dynamic model of the gun turret elevation axis [4] 3
Figure 1-4 Flexible beam and an equivalent driveline stiffness [6] 4
Figure 1-5 Barrel and actuation mechanism [7] 5
Figure 1-6 Split pinion type anti-backlash gear train [3, 8] 6
Figure 1-7 Dual pinion type anti-backlash gear train [9] 7
Figure 1-8 Magnetic backlash eliminator [10] 7
Figure 1-9 Harmonic drive illustration [13] 8
Figure 1-10 Compliant adjustment type anti-backlash gear pair [8] 8
Figure 1-11 Run-out measurement [11] 9
Figure 1-12 CAD models of traverse motors with anti-backlash mechanism [1,12]. 10
Figure 1-13 Image of a traverse drive [12] 10
Figure 2-1 FNSS medium caliber one man turret SABER 13
Figure 2-2 A schematic of a gun turret 14
Figure 2-3 Elevation axis model with the notations 15
Figure 2-4 Dynamic model of the gear train reflected to motor side 18
Figure 2-5 $\boldsymbol{\theta L}$ vs. time (low frequency excitation) 20
Figure 2-6 $\boldsymbol{\theta L}$ vs. time (high frequency excitation) 21
Figure 2-7 Bode plot (input: motor torque, output: load speed) 22
Figure 2-8 Bode plot (input: motor torque, output: motor speed) 22
Figure 2-9 Bode plot (input: motor speed, output: load speed) 23
Figure 3-1 Schematic view of cylinder to cylinder contact in gears 26
Figure 3-2 Cylinder to cylinder contact 27
Figure 3-3 Contact points along the line of action [13] 29
Figure 3-4 Instantaneous pressure angle and roll angle 31
Figure 3-5 Illustration of pressure angle subscripts 32

Figure 3-6 Rotation angle, pressure angle and roll angle relation [18] 33
Figure 3-7 Different Contact Models vs. $\boldsymbol{\theta 1}$(rad) 35
Figure 3-8 Non-dimensionalized Hertzian deflection [23] 36
Figure 3-9 Hertzian Deflections for $\boldsymbol{ie = 7}$ 37
Figure 3-10 Deformation of a gear tooth [18] 38
Figure 3-11Cantilever trapezoidal beam approximation 39
Figure 3-12 Contact height h_{ci} 41
Figure 3-13 Deflection variations of the 1st tooth of the driver gear 42
Figure 3-14 Deflection variations of the 1st tooth of the driver gear [18] 42
Figure 3-15 Stiffness variations vs. roll angle - Shing and Tsai 43
Figure 3-16 Stiffness variations vs. roll angle - Kuang and Yang 44
Figure 3-17 Combined stiffness variation of a tooth pair 45
Figure 4-1 Gear meshing 50
Figure 4-2 Illustration of front and back side contact 51
Figure 4-3 Rotational sign convention 52
Figure 4-4 Double tooth contact region 54
Figure 4-5 Screenshot of the MSC-Adams model [29] 55
Figure 4-6 3D contact schematic in MSC Adams [30] 56
Figure 4-7 Angular velocity of gear 1 for free oscillation - MATLAB - Simulink ... 57
Figure 4-8 Angular velocity of gear 2 for free oscillation - MATLAB – Simulink .. 57
Figure 4-9 Angular velocities: MSC-Adams, Ref. [18] 58
Figure 4-10 Angular velocity of gear 1for constant load - MATLAB - Simulink 59
Figure 4-11 Angular velocity of gear 2 for constant load - MATLAB - Simulink 59
Figure 4-12 Angular velocities: MSC-Adams, Ref. [18] 60
Figure 4-13 Forces acting on the pinion-double tooth zone 61
Figure 4-14 Forces acting on the pinion-single tooth zone before the pitch point 62
Figure 4-15 Forces acting on the pinion-single tooth zone after the pitch point 62
Figure 4-16 Free body diagram of gears 65
Figure 4-17 Variation of dynamic load on pinion tooth for 2000 rpm pinion speed . 68
Figure 4-18 Variation of dynamic load on pinion tooth for 2000 rpm pinion speed, Ref. [16] 68
Figure 4-19 Variation of dynamic load on pinion tooth for 4000 rpm pinion speed . 69

Figure 4-20 Variation of dynamic load on pinion tooth for 4000 rpm pinion speed, Ref. [16] 69
Figure 4-21 Required motor torque for 2000 rpm 70
Figure 4-22 Required motor torque for 4000 rpm 71
Figure 4-23 Friction coefficient for different driver angular velocities- for inverse dynamics 72
Figure 5-1 Schematic of the improved dynamic model 74
Figure 5-2 Isometric view of the turret (turret hull top and front not shown for clarity) 76
Figure 5-3 Isometric view of the turret in MSC Adams 77
Figure 5-4 Side view of the elevation axis 78
Figure 5-5 Friction model in MSC Adams [30] 78
Figure 5-6 Isometric view of the integrated anti-backlash mechanism 79
Figure 5-7 Isometric view of the integrated anti-backlash mechanism in 80
Figure 5-8 Side view of the anti-backlash mechanism 80
Figure 5-9 Free-body diagram of the anti-backlash mechanism 81
Figure 5-10 SISO tool screenshot 82
Figure 5-11 Target tracking in MSC-Adams 82
Figure 5-12 Controls toolkit interface in MSC-Adams 83
Figure 5-13 Bode plot of motor torque to load speed 84
Figure 5-14 Bode plot of motor torque to motor speed 84
Figure 5-15 Bode plot of motor speed to load speed 85
Figure 5-16 Comparison of different friction models on load speed vs. time 86
Figure 5-17 Comparison of different load side stiffness values 87
Figure 5-18 Block diagram of the system 88
Figure 5-19 Load speed vs. time for zero and 0.02 mm backlash 88
Figure 5-20 Motor torque vs. time for zero and 0.02 mm backlash 89
Figure 5-21 Load speed vs. time (b=0.0001 m) 90
Figure 5-22 Power consumption vs. time 91
Figure 5-23 MSC-Adams for no friction and Adams contact friction 92
Figure 5-24 Comparison of different friction models in Matlab 92
Figure 5-25 MSC-Adams plot for different load side stiffness values 93

Figure 5-26 Matlab plot for different load side stiffness values 93
Figure 5-27 Step response of load side in MSC-Adams 94
Figure 5-28 Step response of load side in Matlab 94
Figure 5-29 Power consumption plot in MSC-Adams 95
Figure 5-30 Power consumption plot in Matlab 95
Figure 5-31 Isometric view of MSC-Adams model 96
Figure 5-32 Reference target velocity 97
Figure 5-33 Tracking error vs. time for different anti-backlash mechanism preload values 97
Figure 5-34 Power consumption vs. time for different anti-backlash mechanism preload values 98

LIST OF SYMBOLS

SYMBOLS

b : Backlash

C_{Ravgx} : Surface roughness constant

c_{eq} : Equivalent viscous damping coefficient reflected to motor side

c_g : Gear mesh damping coefficient

c_L : Load side viscous damping coefficient

c_m : Motor side viscous damping coefficient

$[C]$: Viscous damping matrix

D : Dissipation function

E : Modulus of elasticity

f : Coulomb coefficient of friction

f : Face width of the gear

F_n : Normal force on the gear tooth

G : Modulus of rigidity

h_{ci} : Contact height

inv : Involute function

I_L : Load inertia

I_{LR} : Load inertia reflected to motor side

I_m : Motor shaft inertia

I_1 : Motor pinion inertia

I_2 : Sector gear inertia

J : Polar moment of inertia

K : Kinetic energy of the system

k_g : Average gear mesh stiffness

$k_{1,2}$: Combined mesh stiffness of individual gear tooth stiffnesses

k_{eq} : Equivalent torsional stiffness reflected to motor side

k_L : Load side torsional stiffness

k_m : Motor side torsional stiffness

$[K]$: Stiffness matrix

L : Face width of the cylinder

m : Module of gear

$[M]$: Mass matrix

N : Gear ratio

P : Power consumption from the motor

p_b : Base circle pitch

p_k : k^{th} generalized momentum

r_a : Tip circle radius

r_b : Base circle radius

r_p : Pitch circle radius

t_{pi} : Circular tooth thickness of the i^{th} gear at the pitch diameter

T_m : Applied torque by the motor

T_1 : External torque on gear 1

T_2 : External torque on gear 2

U : Potential energy of the system

Q_k : k^{th} generalized force

q_k : k^{th} generalized coordinate

V_{ei} : Entraining velocity of the i^{th} gear tooth pair

V_{rij} : Rolling velocity of the i^{th} gear of the j^{th} tooth

V_{si} : Sliding velocity of the i^{th} gear tooth pair

x_i : Addendum modification coefficient of the i^{th} gear

α_{ij} : Instantaneous roll angle of the i^{th} gear of the j^{th} tooth

δ_H : Deformation due to Hertzian contact

δ_b : Deformation due to bending

δ_s : Deformation due to shear

δ_f : Deformation due to shear

δ_T : Total deformation along the line of action

η_m : Dynamic viscosity of the lubricant

θ_L : Angular position of the load

θ_{LR} : Angular position of the load reflected to motor side

θ_m : Angular position of the motor shaft

$\dot{\theta}_{ref}$: Reference angular velocity

θ_1 : Angular position of the pinion gear

θ_2 : Angular position of the sector gear

μ_{mi} : Benedict-Kelley coefficient of friction

v : Poisson's ratio

ξ : Damping ratio

ρ_{ij} : Instantaneous radius of curvature of the i^{th} gear of the j^{th} tooth

$\emptyset_{ij}$: Instantaneous pressure angle of the i^{th} gear of the j^{th} tooth

$\emptyset^c$: Rack cutter pressure angle

$X_{\Gamma i}$: Load sharing factor

ω_n : Normal load per unit length

CHAPTER 1

INTRODUCTION

1.1 Introduction to the Problem

Today, most of the modern infantry fighting vehicles or main battle tanks use electrical drives in order to operate the turrets in azimuth and elevation axes. Utilization of gear pairs along with those electrical drives is unavoidable in order to comply with the mobility requirements within the limited space in the interior volume of a gun turret. These electrical drive systems need to provide a smooth operation platform with the help of weapon control systems in order to provide a better engagement capability and higher first round hit probability for the gunner. The objective of these control systems can be classified into two major categories. First objective is to keep the gun barrel at a desired orientation regardless of the disturbances coming from the ground. This mode of operation is called stabilization as shown in Figure 1-1.

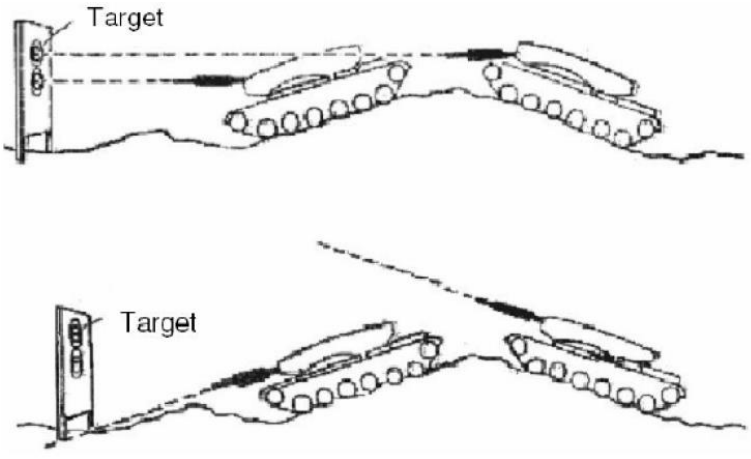

Figure 1-1 Effect of stabilization [1]

Second objective is to operate the gun barrel at a desired angular velocity. This objective is called target tracking or gun laying. It is primarily used for surveillance

of moving targets or to engage moving targets. It can be performed by the gunner or by automatic target tracking systems.

In reality, there are many adverse effects that may degrade the performance of any weapon control system. These are non-linear friction, backlash or play in the driveline, noise from the sensors, driveline compliance and saturation.

Backlash [2] is defined as the amount of distance between mating gears along the line of action as shown in Figure 1-2. There is also a corresponding angular backlash definition, however this linear definition of the backlash will be used throughout the thesis because of its mathematical significance.

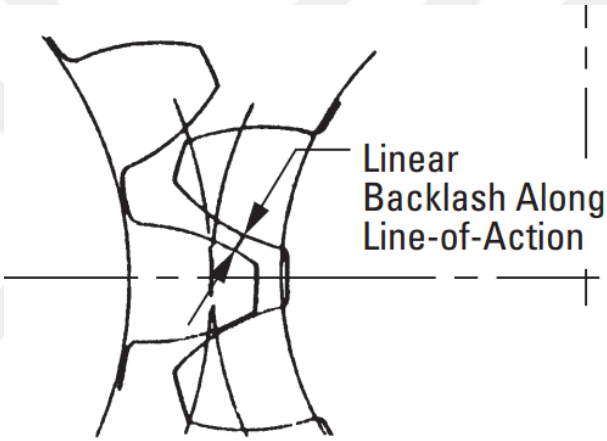

Figure 1-2 Backlash definition along the line of action

Backlash may become a significant problem in applications where there are strict accuracy requirements. Hale et al. [3] states that:

"Although required for proper tooth action, too much backlash may lead to limit cycling for systems with output position feedback, unacceptable position errors for systems with motor position feedback, or chatter for systems excited by time-varying loads."

Considering the sudden direction changes of the motor pinion in order to synchronize itself to load side gear under high frequency disturbances on a bumpy terrain, backlash elimination becomes vital in order to provide satisfactory control performance in weapon systems.

Backlash elimination can be achieved via mechanical solutions, advanced non-linear control algorithms or both. In turret drives, regardless of the control system

architecture, there is almost always a mechanical form of backlash elimination device.

1.2 Review of Literature

Accurate dynamic modeling of gun turrets constitutes the basis of any weapon control system. As expected, number of papers directly about dynamic modeling of gun turrets is scarce due to the military nature of the topic. The existing know-how is usually kept within the companies who build drives for gun turrets.

Many of the work that was conducted after 2000's take Purdy [4] as reference and use his model as a basis for improvement. The purpose of the mentioned study is to use a feed-forward controller by measuring the angular velocity of the vehicle hull, and to demonstrate that it yields a better stabilization performance. The dynamic model in the paper consists of the motor and trunnion viscous friction in the bearings, the flexibility of the gun barrel by a torsional spring, proportional servo motor gain and the stiffnesses of the entire elevation mass is assumed as a lumped linear driveline stiffness of the elevation axis as shown in Figure 1-3. The gearbox in the system is treated as a speed reducer element.

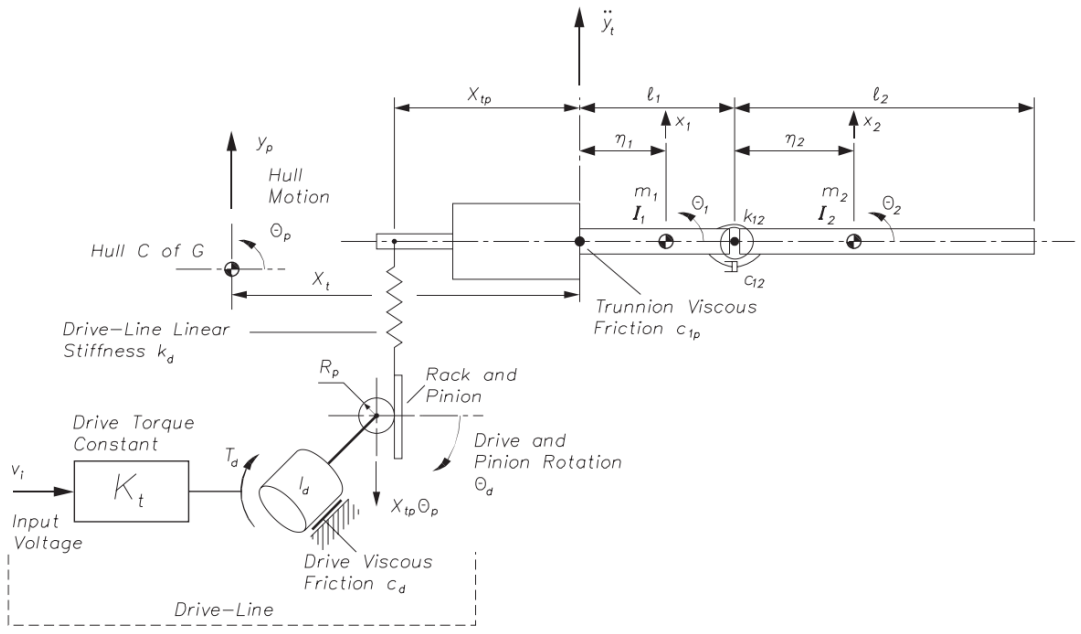

Figure 1-3 Dynamic model of the gun turret elevation axis [4]

In another study; Purdy [5], included the effect of out of balance in his model and demonstrated that stabilization can still be achieved. A very similar dynamic model to that used in [4] has been used in that work.

Different gun barrel models have been investigated in another study by Purdy [6]. The purpose of this study is to model the gun barrel more accurately as a flexible element. The compliances in the system are a lumped driveline stiffness and the gun barrel as a Euler-Bernoulli type flexible beam as shown in Figure 1-4. The gearbox in this model is again assumed as a rigid speed reducing element.

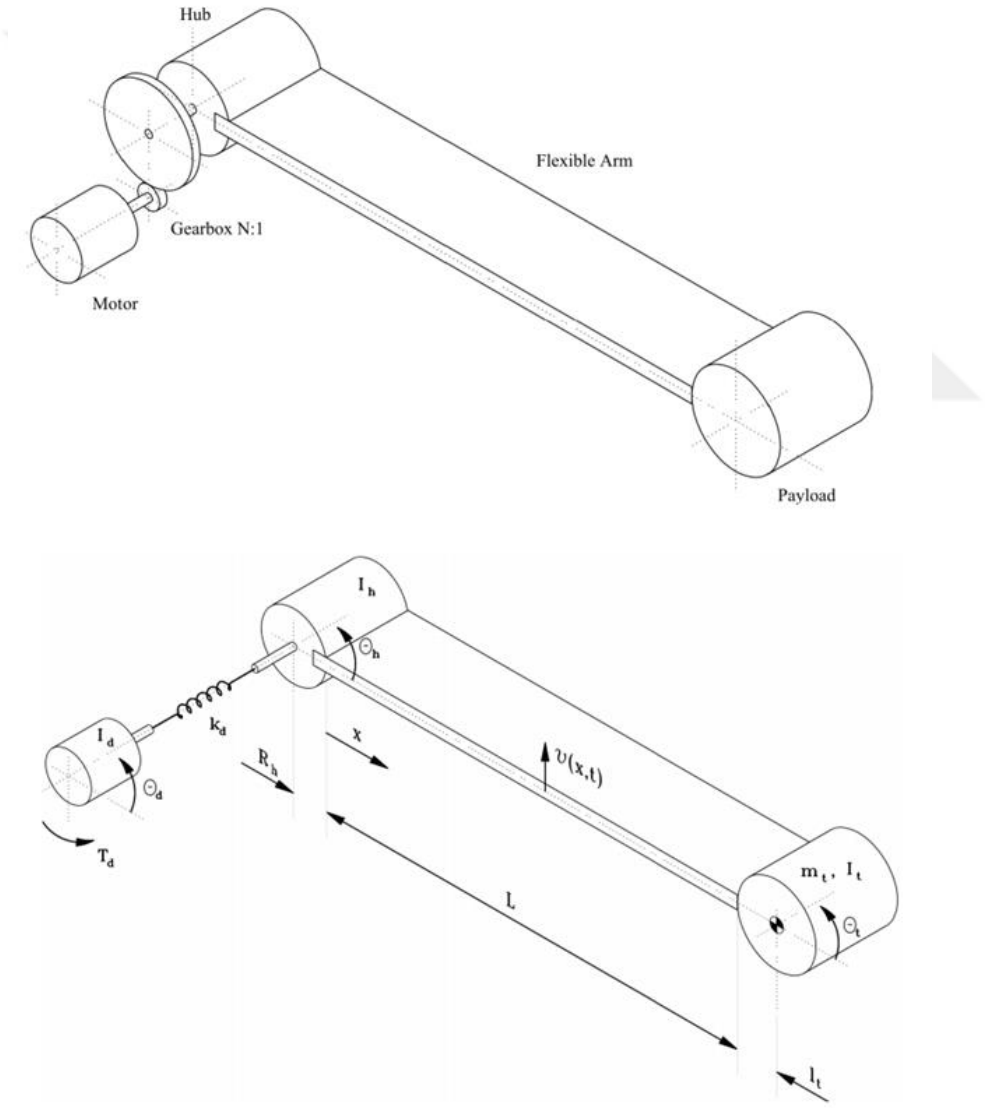

Figure 1-4 Flexible beam and an equivalent driveline stiffness [6]

In a modeling and control thesis performed in Aselsan Inc., Afacan [7], models the gun turret elevation axis including hydraulic actuator dynamics, orifice flow characteristics, Coulomb friction with emphasis on stick-slip and the compressibility of the hydraulic fluid (Figure 1-5). Drive-line compliances are not included in the mentioned study.

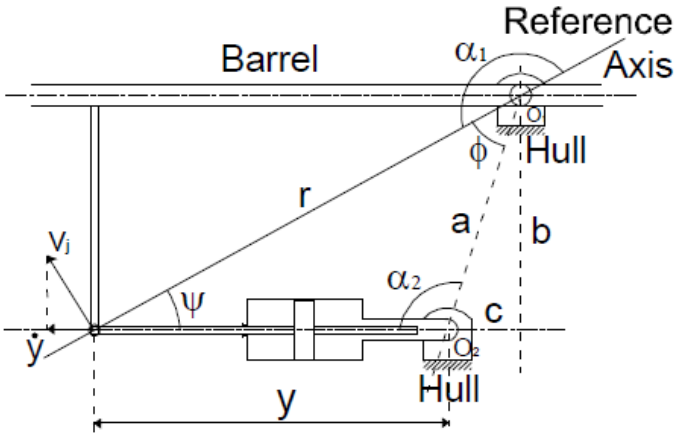

Figure 1-5 Barrel and actuation mechanism [7]

In a more recent study performed by Karayumak [1], both azimuth and elevation axes of a weapon system are modeled. A coincidence window algorithm which takes into account the gun barrel flexibilities is constructed. The elevation axis model used in that study is based on the dynamic model explained in [4]. The gun barrel is assumed to be connected by a series of torsional springs and dampers.

One of the studies, that take into account the gear dynamics and gear backlash, in the overall turret dynamics is performed by Yumrukçal [12]. Structural parameters such as stiffness and damping are modeled and identified by means of experimental frequency sweeps. However, the equations of motion that govern the overall dynamics are not explicitly given in the presence of driveline compliances and backlash.

Another scope of the thesis study is backlash elimination and its implementation on the elevation axis of a gun turret. For this purpose, backlash elimination techniques are presented in the subsequent parts. In the most general sense, backlash elimination by means of mechanical means can be classified into three major categories:

1. Fixed center distance gears

2. Unconventional methods
3. Variable center distance gears

First category is the anti-backlash gear trains with fixed center distance gear pairs. Split pinion gears, as the name implies, consist of two halves. The halves are able to rotate relative to each other [3, 8] and they are preloaded against each other by means of springs (Figure 1-6). This preloading essentially increases the effective tooth thickness so that while the output gear is changing its direction of rotation; it encounters the resistance of the spring loaded half instead of encountering a clearance. These systems are preferable for light loading and low angular velocity operations.

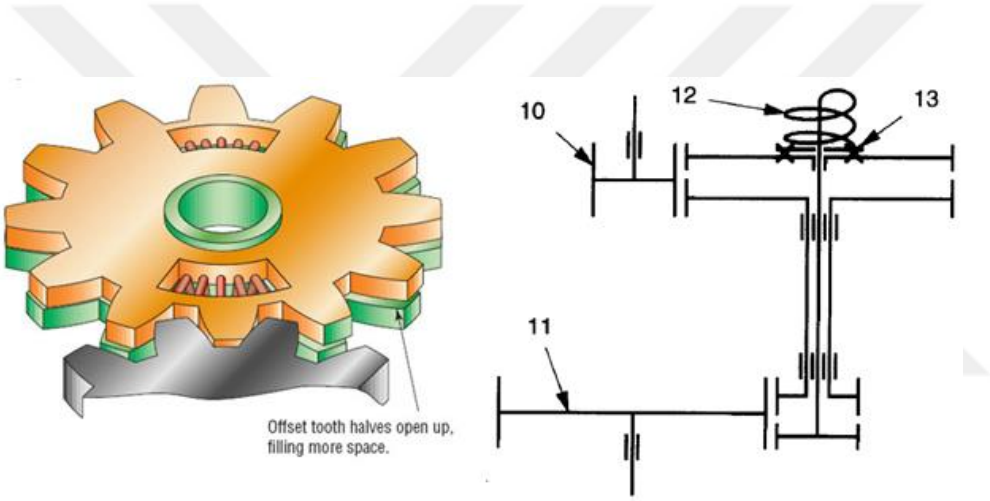

Figure 1-6 Split pinion type anti-backlash gear train [3, 8]

The other type of anti-backlash gear train type which has a fixed center distance, is the dual pinion [3]. Dual pinion anti-backlash gears have two separate transmission paths from the input shaft to the output shaft. With the aid of the preloaded elements one transmission path opposes the other in a similar fashion as the split pinion.

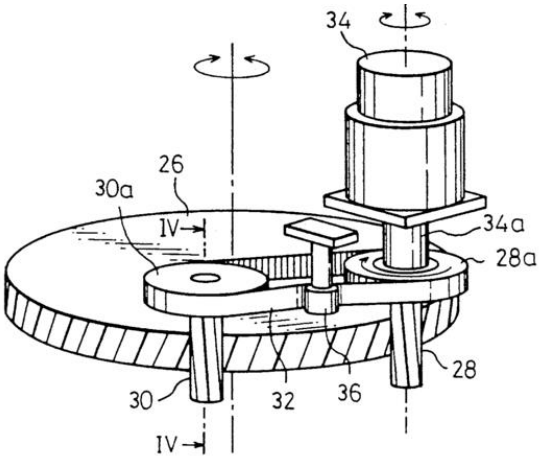

Figure 1-7 Dual pinion type anti-backlash gear train [9]

Note that both in dual pinion and split pinion type systems the input shaft needs to overcome an additional preload torque in addition to the load side inertia and driveline friction. It also induces extra friction torque on the input in the preloaded direction. Furthermore, they are prone to assembly and manufacturing errors because of their fixed center distance nature.

Another possible solution technique is magnetic backlash elimination. By placing the north pole of one gear magnet at an intermediate position of the north and south poles of the opposing gear magnets, Figure 1-8, a backlash free operation without excessive friction is claimed in [10]. This solution is not utilized in practice very much though it sounds promising for light loaded, low speed operations.

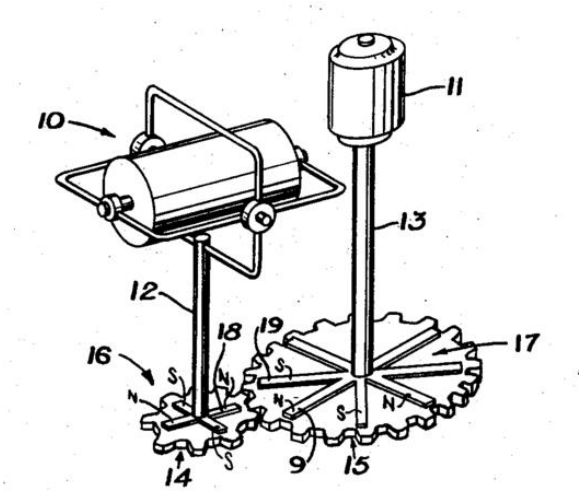

Figure 1-8 Magnetic backlash eliminator [10]

In addition to the conventional backlash elimination techniques, there are unconventional backlash elimination techniques such as harmonic drives, epicyclic drives and cycloidal drives [8]. Due to their high cost, they are restricted to mainly aviation and space applications when there are severe performance and weight requirements. One example of a harmonic drive with internal flexible spline is shown in Figure 1-9 [13].

Figure 1-9 Harmonic drive illustration [13]

The final category of anti-backlash gear trains, which is the main scope of this thesis, is *compliant adjustment type* anti-backlash mechanisms. In these systems, the center distance between gears (hence the operating pressure angle between the meshing gear teeth) becomes variable. Usually the input pinion is pushed against or pulled towards the load side gear by means of a preloaded spring and it has a freedom to rotate around an independent rotation axis. A simple schematic of this system is shown in Figure 1-10.

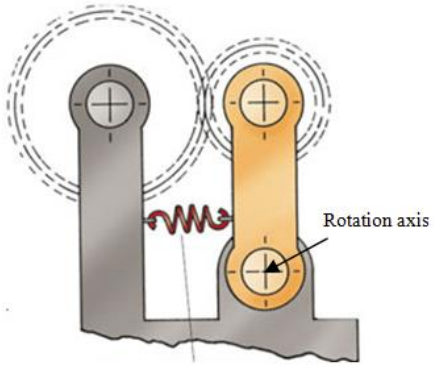

Figure 1-10 Compliant adjustment type anti-backlash gear pair [8]

At this point it is important to note that compliant adjustment type anti-backlash gear pairs can compensate radial run-out in addition to backlash. Radial run-out can be

described as "*the variations in the distance perpendicular to the axis of rotation between the indicated surface and a datum surface*" [11]. It is a result of combined error sources such as deviation from the ideal tooth thicknesses during manufacturing, the distortion due to heat treatment of gears, general machining limitations etc. It is usually measured by placing an indicator over a pin and recording the variations as shown in Figure 1-11.

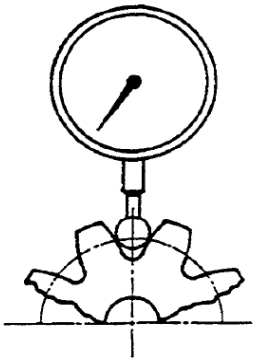

Figure 1-11 Run-out measurement [11]

Since the gear train in turrets usually consist of large diameter gears both in azimuth and elevation axes; the amount of radial run-out is non-negligible in these systems. Hence the ability to compensate run-out becomes critical. Furthermore, by avoiding fixing the rotation center of the motor pinion in a certain position in the turret hull allows the designers to relax the machining tolerances for gear mounting provisions which is imperative in order to reduce manufacturing costs. Finally, by changing the spring coefficient and the amount of preload, a wide range of dynamic forces can be achieved so that friction forces can be adjusted as low as possible while keeping backlash zero. Of course this would require a detailed dynamic analysis.

In the following figures CAD images (Figure 1-12) of a traverse drive that actuates the turret in azimuth axis and the real physical system (Figure 1-13) are shown. The preloading element applies a torque which pushes the pinion against the ring gear. Note that the working principles are very similar for both elevation and traverse axes.

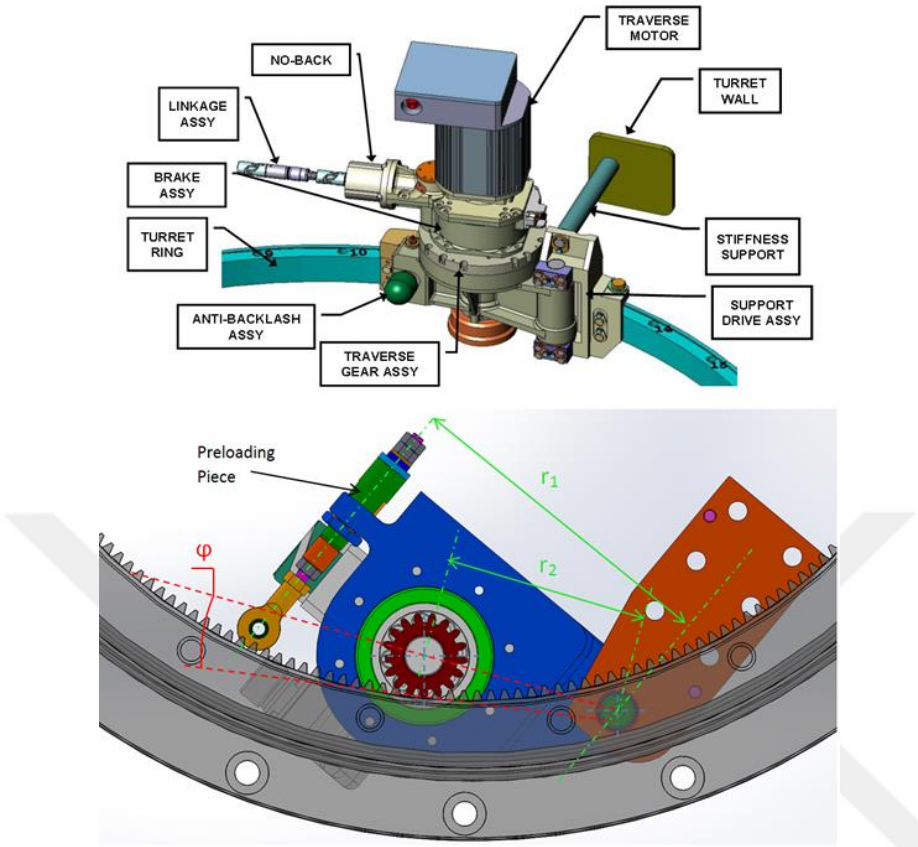

Figure 1-12 CAD models of traverse motors with anti-backlash mechanism [1,12]

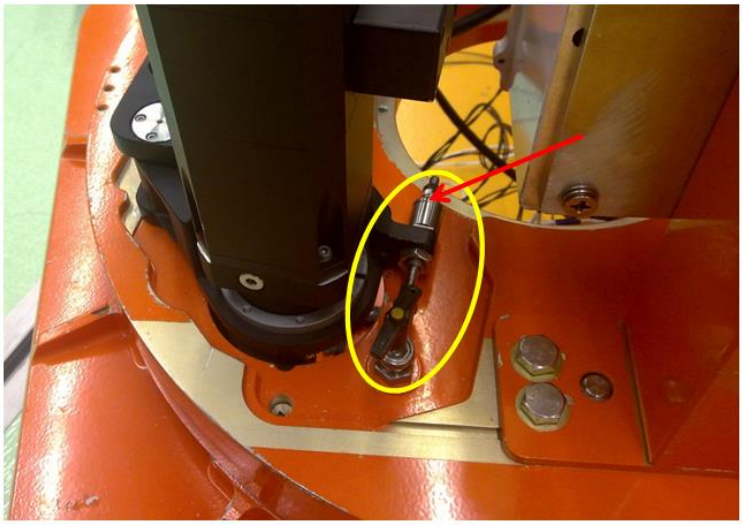

Figure 1-13 Image of a traverse drive [12]

It is interesting to note that despite the widely utilization of these mechanisms in the military, there is no reported dynamic simulation study that investigates the

performance characteristics of these mechanisms and their effect on the overall turret dynamics.

1.3 Objective and Scope of the Thesis

The main contribution of this thesis to literature is the application of the gear dynamics to the overall gun turret dynamics. The developed dynamic model that includes gear dynamics, can be used to design more advanced controllers that take into account gear impact, the backlash and gear mesh friction. For this purpose, three independent modeling paradigms have been used; namely MATLAB, MATLAB-Simulink and MSC-Adams. The MATLAB and the Simulink models are constructed by the solution of the differential equations of motion. Whereas the model in multibody dynamics program MSC-Adams is constructed by connecting the physical parts in the correct kinematic sequence and determining the correct contact parameters.

In chapter 2, the groundwork of the thesis has been laid with the introduction of the basic elements of a gun turret and their kinematic relations with each other. Two simple state space models are constructed that treat the gear pair simple speed reduction elements. First model is the 3 degree of freedom (d.o.f.) model where the motor shaft and load stiffnesses and damping are considered. The equations of motion are derived by using Lagrange method. Then, as is commonly done in the literature, a simplified equivalent 2 d.o.f. system where the drive-line stiffnesses and the inertias are reflected to motor side is constructed. Open loop Bode plots are constructed for various transfer functions of interest. Time domain simulations are also performed.

In chapter 3, the contact parameters of gears which constitute the foundation of the gear dynamics, namely gear mesh stiffness and mesh damping are explained in a detailed manner. The complicated variation of gear deflection as the point of contact travels along the line of action is computed with different gear deflection models available in the literature. The contributions of gear bending, shear, foundation and Hertzian deflections are all included in the calculations. These models are then compared with the formulation given in the ISO standard which is considered as the benchmark.

In chapter 4, the equations of motions for a fixed center distance gear pair are derived. The possible front side contact, back side contact and separation modes are considered. A MATLAB-Simulink model and a MSC-Adams model is constructed. The developed models are compared among themselves and with the literature as well. Then a realistic gear friction model which is used in AGMA standards, is inserted into the developed model while considering various contact scenarios. The inverse dynamics model which can capture the force variation on a single tooth is also constructed for verification purposes.

In chapter 5, the final dynamic model which includes, driveline compliances as well as gear flexibilities is constructed both in MATLAB-Simulink and MSC-Adams environment. After having the open loop system in MATLAB, the angular velocity of the gun is controlled for target tracking purposes. The required controller is designed by adjusting the closed loop poles of the system via root locus diagram in MATLAB SISO toolbox. The controls toolkit is used for target tracking in MSC-Adams environment. Finally, a compliant adjustment type anti-backlash mechanism commonly used in military applications is inserted to the developed multi-body dynamics model. Various target tracking performance criteria are compared for different preload values.

CHAPTER 2

SIMPLIFIED DYNAMIC MODEL OF THE GUN TURRET ELEVATION AXIS

2.1 Introduction

This chapter introduces a simple 3 d.o.f. dynamic model of a gun turret elevation axis upon which the rest of the thesis is going to be built. The compliance of the driving shaft as well as the compliance of the load side has been taken into account. The equations of motion are derived from Lagrange equations. The open loop time domain and frequency responses are plotted.

2.2 Dynamic Modeling

Any gun turret that is used in military vehicles should have some similar elements in order to fulfill the mobility requirements in a military environment. These are the drive systems (i.e. motors), gear pair(s), trunnions, gun mounts, rotor structure, turret hull, bearings that allow rotation in elevation axis, and the guns.

Figure 2-1 FNSS medium caliber one man turret SABER

- Turret hull: It acts as the main frame for the non-elevating components. It is fixed to the vehicle chassis.

- Rotor: It acts as the main frame for all of the elevating components. The rotor is connected to the turret hull by means of bearings, therefore by a revolute joint.
- Pinion shaft: Pinion shaft is the geared part of the elevation motor. It is where the motor torque is transmitted to the load side. It is connected to the turret hull by bearings therefore a revolute joint. Pinion shaft's internal compliance is included therefore, there is a torsional spring that connects the driving part of the shaft to the driven part.
- Sector gear: Sector gear meshes with the pinion gear to increase the torque reflected to the load side. it is to be connected to the rotor by means of a torsional spring since the driveline compliance is considered.
- Gun barrel: Gun barrel is the tube where the ammunition exits the weapon. In the scope of this thesis, it is assumed to be rigidly connected to the gun body.

A simplified isometric view of the turret which shows the aforementioned elements is shown in Figure 2-2.

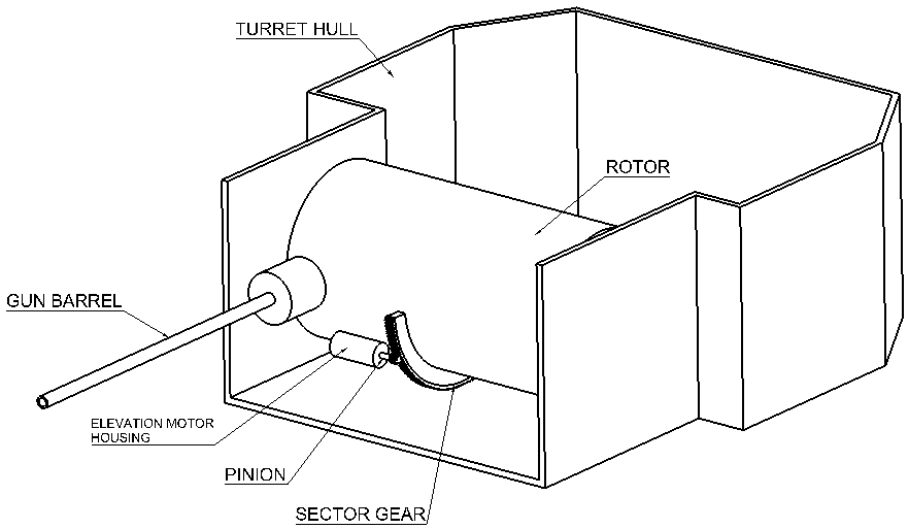

Figure 2-2 A schematic of a gun turret

An illustration with the scientific notation used is given in Figure 2-3. Note that all of the elevated mass is lumped as a single unit. This lumped mass is referred as the "load".

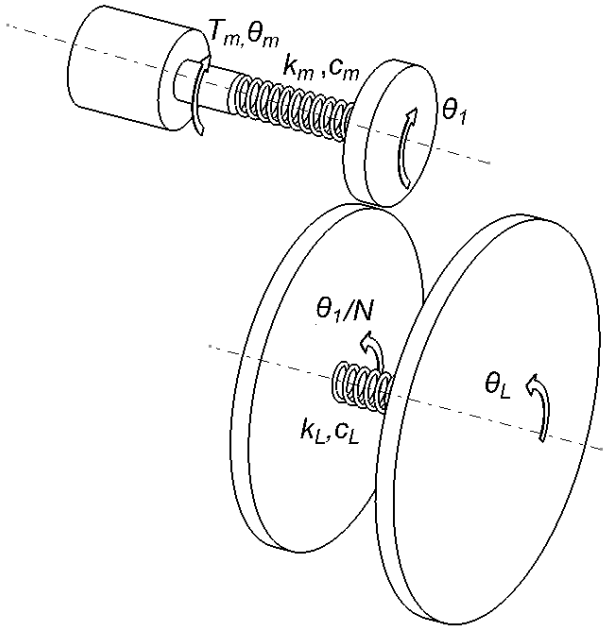

Figure 2-3 Elevation axis model with the notations

In the above notation, the torque applied by the motor is given as T_m. The discs have the following inertias, I_m, I_1, I_2, I_L to represent motor inertia, pinion inertia (gear 1), sector gear inertia (gear 2) and the load inertia respectively. N is the gear ratio given as d_2/d_1 where d_2 is the pitch diameter of gear 2 and d_1 is the pitch diameter of gear 1. The pinion shaft compliance is given as k_m and the load side compliance is given as k_L. The viscous friction coefficient on the motor side is given as c_m whereas the viscous friction coefficient on the load side is given as c_L.

The motor shaft stiffness can be calculated from elementary strength theory as;

$$k_m = \frac{G J}{L} \tag{2.1}$$

Where G is the shear modulus of rigidity, J is the polar moment of inertia and L is the length of the motor shaft.

The load side stiffness needs to be determined either by a finite element analysis or system identification. Within the scope of this thesis, it is treated as known.

Viscous damping coefficients of the bearings can be determined from the related bearing catalogues.

The gear train is modeled as rigid for the time being, therefore it only acts as a speed reduction element. The motion constraints are;

$$N = \frac{\theta_1}{\theta_2} = \frac{\dot{\theta}_1}{\dot{\theta}_2} = \frac{\ddot{\theta}_1}{\ddot{\theta}_2} \tag{2.2}$$

2.3 Lagrange Equations of Motions

Lagrange equations of motion with the generalized coordinates q_k for any system is given as follows [14].

$$\dot{p}_k - \frac{\partial K}{\partial q_k} + \frac{\partial U}{\partial q_k} + \frac{\partial D}{\partial q_k} = \bar{Q}_k \tag{2.3}$$

With the selection of generalized coordinates as $\theta_m, \theta_1, \theta_L$ the kinetic energy of the system is;

$$K = \frac{1}{2} I_m \dot{\theta}_m^2 + \frac{1}{2} I_1 \dot{\theta}_1^2 + \frac{1}{2} I_2 \left(\frac{\dot{\theta}_1^2}{N^2} \right) + \frac{1}{2} I_L \dot{\theta}_L^2 \tag{2.4}$$

The potential energy of the system is given as;

$$U = \frac{1}{2} k_m (\theta_m - \theta_1)^2 + \frac{1}{2} k_L \left(\frac{\theta_1}{N} - \theta_L \right)^2 \tag{2.5}$$

The dissipation function is given as;

$$D = \frac{1}{2} c_m \left(\dot{\theta}_m - \dot{\theta}_1 \right)^2 + \frac{1}{2} c_L \left(\frac{\dot{\theta}_1}{N} - \dot{\theta}_L \right)^2 \tag{2.6}$$

The necessary symbolic derivatives are given as;

$$\dot{p}_k = \frac{d}{dt} \left(\frac{\partial K}{\partial \dot{q}_k} \right) \tag{2.7}$$

$$\dot{p}_{\theta_m} = \frac{d}{dt} \left(\frac{\partial K}{\partial \dot{\theta}_m} \right) = I_m \ddot{\theta}_m \tag{2.8}$$

$$\dot{p}_{\theta 1} = \frac{d}{dt} \left(\frac{\partial K}{\partial \dot{\theta}_1} \right) = \left(I_1 + \frac{I_2}{N^2} \right) \ddot{\theta}_1 \tag{2.9}$$

$$\dot{p}_{\theta_L} = \frac{d}{dt} \left(\frac{\partial K}{\partial \dot{\theta}_L} \right) = I_L \ddot{\theta}_L \tag{2.10}$$

$$\frac{\partial U}{\partial \theta_m} = k_m(\theta_m - \theta_1) \tag{2.11}$$

$$\frac{\partial U}{\partial \theta_1} = -k_m\theta_m + (k_m + \frac{k_L}{N^2})\theta_1 - \frac{k_L}{N}\theta_L \tag{2.12}$$

$$\frac{\partial U}{\partial \theta_L} = -k_L(\frac{\theta_1}{N} - \theta_L) \tag{2.13}$$

$$\frac{\partial D}{\partial \dot{\theta}_m} = c_m(\dot{\theta}_m - \dot{\theta}_1) \tag{2.14}$$

$$\frac{\partial D}{\partial \dot{\theta}_1} = -c_m\dot{\theta}_m + (c_m + \frac{c_L}{N^2})\dot{\theta}_1 - \frac{c_L}{N}\dot{\theta}_L \tag{2.15}$$

$$\frac{\partial D}{\partial \dot{\theta}_L} = -c_L(\frac{\dot{\theta}_1}{N} - \dot{\theta}_L) \tag{2.16}$$

$$\overline{Q}_m = T_m \tag{2.17}$$

When the Lagrange equations are applied to individual generalized coordinates and presented in matrix form, the following equations is obtained;

$$\begin{pmatrix} I_m & 0 & 0 \\ 0 & (I_1 + \frac{I_2}{N^2}) & 0 \\ 0 & 0 & I_L \end{pmatrix} \begin{bmatrix} \ddot{\theta}_m \\ \ddot{\theta}_1 \\ \ddot{\theta}_L \end{bmatrix} + \begin{pmatrix} c_m & -c_m & 0 \\ -c_m & (c_m + \frac{c_L}{N^2}) & \frac{-c_L}{N} \\ 0 & \frac{-c_L}{N} & c_L \end{pmatrix} \begin{bmatrix} \dot{\theta}_m \\ \dot{\theta}_1 \\ \dot{\theta}_L \end{bmatrix} + \begin{pmatrix} k_m & -k_m & 0 \\ -k_m & (k_m + \frac{k_L}{N^2}) & \frac{-k_L}{N} \\ 0 & \frac{-k_L}{N} & k_L \end{pmatrix} \begin{bmatrix} \theta_m \\ \theta_1 \\ \theta_L \end{bmatrix} = \begin{bmatrix} 1 \\ 0 \\ 0 \end{bmatrix} T_m \tag{2.18}$$

Or more generally it becomes;

$$[M]\left[\ddot{\theta}\right] + [C]\left[\dot{\theta}\right] + [K][\theta] = [I_d][u] \tag{2.19}$$

The above system can be converted to state space equation form;

$$\begin{aligned} \dot{x} &= Ax + Bu \\ y &= Cx + Du \end{aligned} \tag{2.20}$$

The output matrix *C* given in Eqn. (2.20) should not be confused with the damping matrix *[C]* given in Eqn. (2.19).

The system matrices can be obtained from;

$$A = \begin{bmatrix} [0]_{3x3} & [I]_{3x3} \\ -[M]^{-1}[K] & -[M]^{-1}[C] \end{bmatrix} \tag{2.21}$$

$$B = \begin{bmatrix} [0]_{3x1} \\ -[M]^{-1}[I_d] \end{bmatrix} \tag{2.22}$$

Where the state vector is;

$$x = \begin{bmatrix} \theta_m & \theta_1 & \theta_L & \dot{\theta}_m & \dot{\theta}_1 & \dot{\theta}_L \end{bmatrix}^T \tag{2.23}$$

The motor torque is the only input of the system, and the selection of the output state determines the remaining *C* and *D* matrices. The possible logical outputs that can be selected are the motor position, motor speed, load position or load speed. As an example, if the load speed is selected as the output;

$$C = \begin{bmatrix} 0 & 0 & 0 & 0 & 0 & 1 \end{bmatrix} \tag{2.24}$$

$$D = 0 \tag{2.25}$$

It is conventional [4, 6] to simplify the developed model in Figure 2-3 to a 2 d.o.f. system by reflecting all of the driven inertias, stiffness and damping terms to the motor side as shown in Figure 2-4; if the inertias of the gear 1 and gear 2 are small compared to inertias of the motor and load sides.

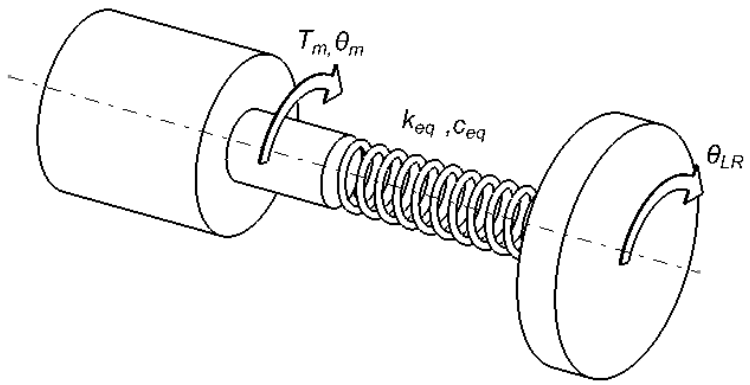

Figure 2-4 Dynamic model of the gear train reflected to motor side

In the above figure, equivalent stiffness k_{eq} and equivalent damping c_{eq} terms reflected to the motor side can be calculated as;

$$\frac{1}{k_{eq}} = \frac{1}{k_m} + \frac{1}{k_L / N^2}$$
$$k_{eq} = \frac{k_m k_L}{k_m N^2 + k_L} \tag{2.26}$$

$$c_{eq} = c_m + \frac{c_L}{N^2} \tag{2.27}$$

The inertia of the load and the angular position reflected to the motor side is;

$$I_{LR} = I_L / N^2 \tag{2.28}$$

$$\theta_{LR} = \theta_L / N \tag{2.29}$$

With the simplified configuration the matrix equation of motions become;

$$\begin{bmatrix} I_m & 0 \\ 0 & I_{LR} \end{bmatrix} \begin{bmatrix} \ddot{\theta}_m \\ \ddot{\theta}_{LR} \end{bmatrix} + \begin{bmatrix} c_{eq} & -c_{eq} \\ -c_{eq} & c_{eq} \end{bmatrix} \begin{bmatrix} \dot{\theta}_m \\ \dot{\theta}_{LR} \end{bmatrix} + \begin{bmatrix} k_{eq} & -k_{eq} \\ -k_{eq} & k_{eq} \end{bmatrix} \begin{bmatrix} \theta_m \\ \theta_{LR} \end{bmatrix} = \begin{bmatrix} 1 \\ 0 \end{bmatrix} T_m \tag{2.30}$$

$$A = \begin{bmatrix} [0]_{2x2} & [I]_{2x2} \\ -[M]^{-1}[K] & -[M]^{-1}[C] \end{bmatrix} \tag{2.31}$$

$$B = \begin{bmatrix} [0]_{2x1} \\ -[M]^{-1}[I_d] \end{bmatrix} \tag{2.32}$$

Where the state vector is;

$$x = \begin{bmatrix} \theta_m & \theta_{LR} & \dot{\theta}_m & \dot{\theta}_{LR} \end{bmatrix}^T \tag{2.33}$$

Similarly, with the motor torque as the input and reflected load speed as the output the remaining state matrices become;

$$C = \begin{bmatrix} 0 & 0 & 0 & 1 \end{bmatrix} \tag{2.34}$$

$$D = 0 \tag{2.35}$$

It should be noted that, reflecting the values to the motor side causes losing a 1 d.o.f. in the system. This is due to the fact that load and gear 2 inertias are lumped together.

2.4 Open Loop System Simulations

Results of the model given by Figure 2-3 is referred to as the 3 d.o.f. model whereas the results of the model given by Figure 2-4 is referred to as the 2 d.o.f. model. The following representative parameters are used for the simulation purposes of the thesis.

Table 1 Gun turret parameters

Motor inertia- I_m (kgm^2)	3×10^{-4}
Pinion inertia-I_1 (kgm^2)	3×10^{-4}
Gear inertia-I_2 (kgm^2)	1.5
Load inertia-I_L (kgm^2)	50
Motor shaft stiffness (Nm/rad)	5×10^4
Load side torsional stiffness (Nm/rad)	5×10^7
Motor shaft viscous damping coefficient (Nms/rad)	0.3
Trunnion bearings viscous damping coefficient (Nms/rad)	10

For a sinusoidal motor torque input, $T_m(t) = 10\sin(10 \times 2\pi t) + 5\sin(5 \times 2\pi t)$, the load side speeds for two models are plotted in Figure 2-5.

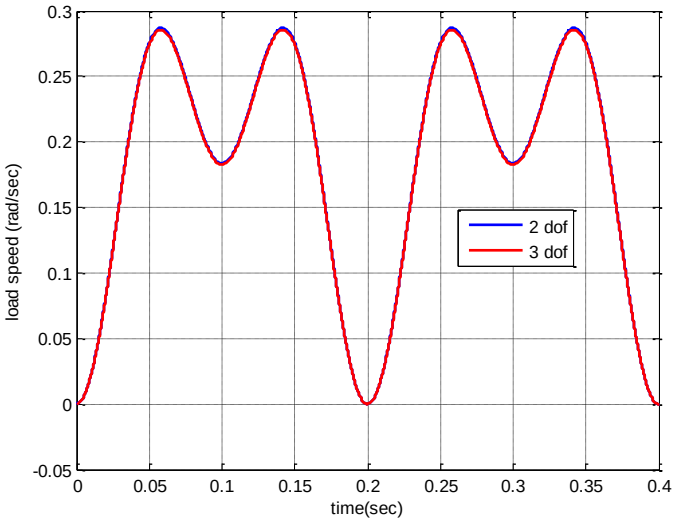

Figure 2-5 $\dot{\theta}_L$ vs. time (low frequency excitation)

The results look quite similar. However when the frequency of excitation is increased such that $T_m(t) = 10\sin(1500 \times 2\pi t) + 5\sin(50 \times 2\pi t)$, Figure 2-6 is obtained.

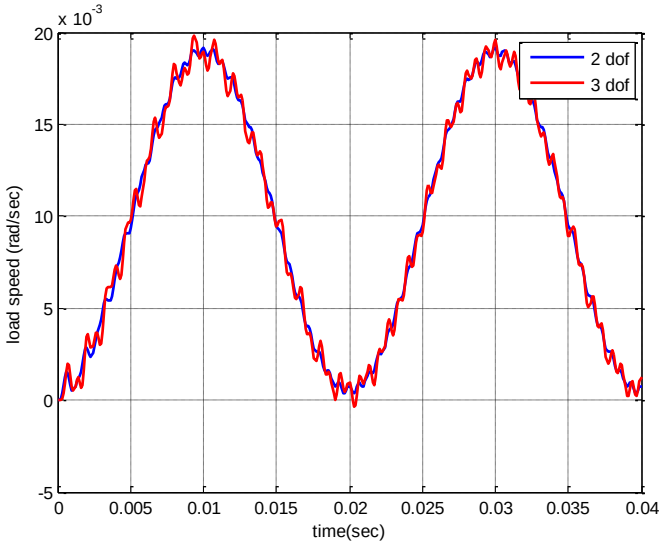

Figure 2-6 $\dot{\theta}_L$ vs. time (high frequency excitation)

A significant difference in the load speed is predicted by the two models. This is due to the fact that one degree of freedom was lost while reflecting the load side parameters to the motor side.

For the increased frequency of excitation, this difference can be observed in the frequency domain much more easily. Bode plots of the possible transfer functions are plotted in Figure 2-7, Figure 2-8 and Figure 2-9 respectively.

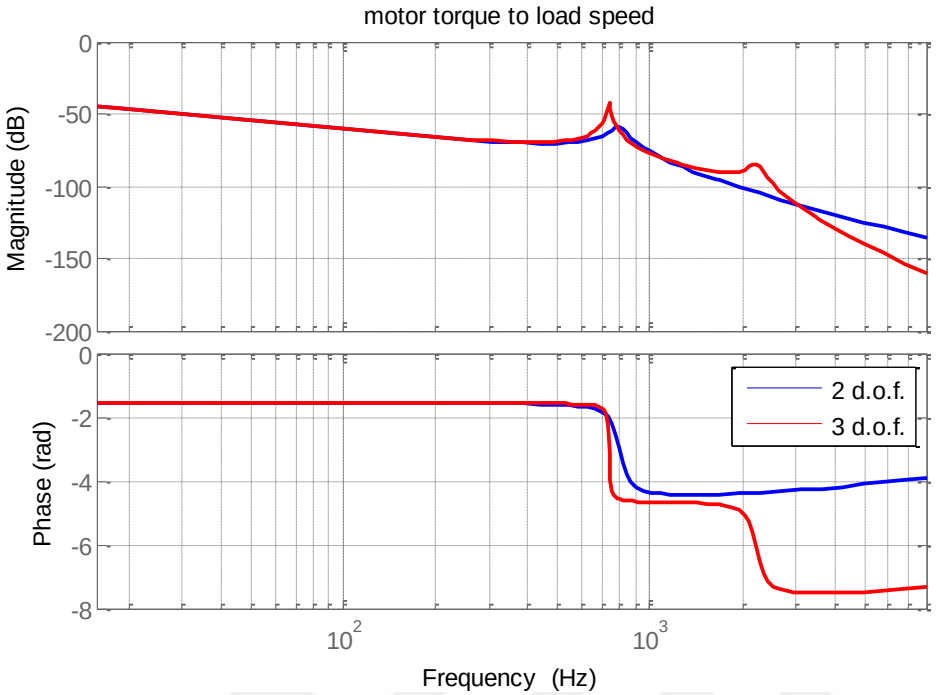

Figure 2-7 Bode plot (input: motor torque, output: load speed)

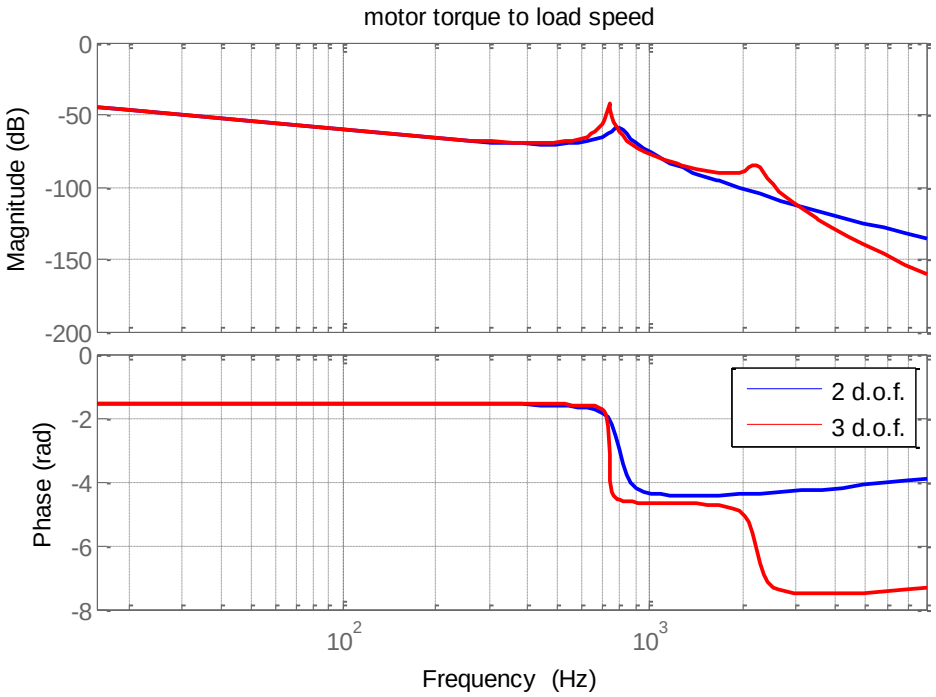

Figure 2-8 Bode plot (input: motor torque, output: motor speed)

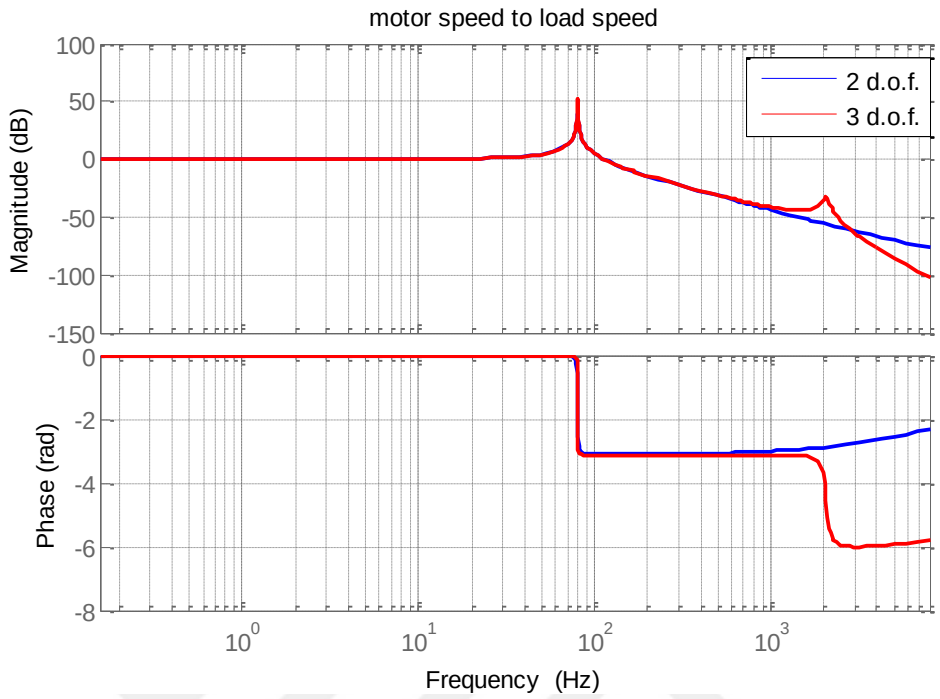

Figure 2-9 Bode plot (input: motor speed, output: load speed)

Inspection of the above figures indicate that there is an extra resonance around 2200 Hz predicted by the 3 d.o.f. model.

$$f = \frac{1}{2\pi}\sqrt{eig(M^{-1}K)} \tag{2.36}$$

$$f_{2dof} = \begin{bmatrix} 786 \\ 0 \end{bmatrix} \tag{2.37}$$

$$f_{3dof} = \begin{bmatrix} 2199 \\ 727 \\ 0 \end{bmatrix} \tag{2.38}$$

The extra peak predicted by the 3 d.o.f. model is at 2199 Hz. Since this frequency is outside the bandwidth for most controllers, it does not have a practical significance.

The following conclusions can be deducted by investigation of the open loop responses of the gun turret for different parameters.

- Higher stiffness at motor side and load side give higher resonance frequency.
- Higher load inertia gives a lower resonance frequency.

- Viscous damping coefficients have little effect on the resonant frequencies, however higher damping coefficients make the resonant "smoother".
- Gear ratio has a complex behavior for the resonant frequency. Although increasing the gear ratio would decrease the equivalent stiffness, it also decreases the equivalent inertia reflected to the motor side.

CHAPTER 3

DETERMINATION OF CONTACT PARAMETERS FOR GEAR DYNAMICS

3.1 Introduction

The contact force between a meshing gear pair is expressed as,

$$F_n = k\delta + c\dot{\delta} \tag{3.1}$$

where δ is the penetration depth of driving gear into the driven gear and $\dot{\delta}$ is the penetration velocity. The first term on the right hand side of Eq. (3.1) is the elastic portion of the force term and the second is related to the gear friction damping. This chapter explains how to determine the gear mesh stiffness *k* and gear mesh damping *c* for different spur gears.

3.2 Gear Mesh Stiffness

Computation of the gear mesh stiffness values along the line of action which is the most dominant factor that affects gear contact force is a fundamental research area. There have been many different approaches to this problem. First approach is to use the classical finite element method (FEM) in order to compute deflections along the line of action as is done in [15, 16]. Even though this method is the most accurate, it is computationally expensive since for each gear pair of interest, a new FEM model is necessary. To overcome this difficulty there have been numerous analytical attempts to calculate the mesh stiffness, in addition to semi-analytical or empirical estimations that give close approximations with the FEM models.

Almost all of the studies divide the mesh stiffness problem into finding the two types of deflections, namely localized deflections and gear body deflections, and superimposing them. Localized deflections are calculated by using the Hertzian contact theory by assuming two contacting cylinders. Other deflections, namely tooth

deflections due to bending and shear, and foundation deflection of the gear body are found by assuming the gear tooth as a trapezoidal beam.

3.2.1 Local Deflection Models

In their renowned rotary model paper which includes effects such as backlash and impact in the equations of motion; Yang and Sun [17] estimated the penetration by considering an external cylinder to cylinder contact as shown in Figure 3-1.

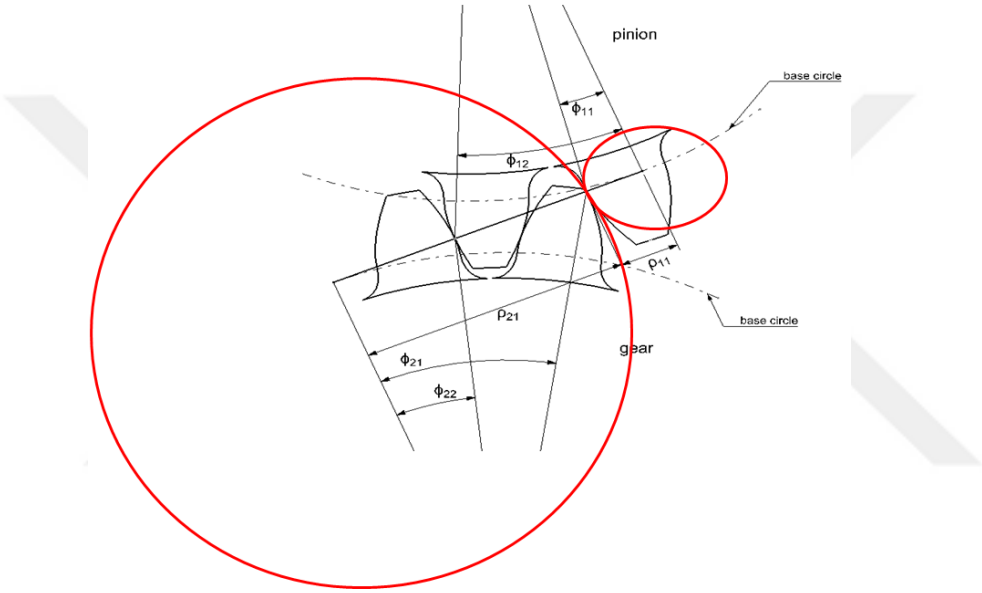

Figure 3-1 Schematic view of cylinder to cylinder contact in gears

By applying the Hertzian theory, they estimated the interpenetration formula as,

$$\delta = \frac{4(1-\nu^2)}{\pi E L} F \tag{3.2}$$

from which the stiffness can be calculated as:

$$K = \frac{\pi E L}{4(1-\nu^2)} \tag{3.3}$$

In the above equation; F is the normal load acting on the teeth, E is the modulus of elasticity, ν is the Poisson's ratio and L is the face width of the gear. This formula which implies a constant stiffness for the gear pair has been widely accepted and used by the gear dynamics researchers [18, 19, 20] as a convenient way of calculating the Hertzian deflection portion of the overall deflection.

However, the problem of cylinder to cylinder contact deserves a more rigorous treatment because of the fact that many different contact models have been proposed by researchers and are available in literature. A good overview of these models is given in [21].

Johnson derived a formula for external cylinder to cylinder contact based on the Hertz theory. The indentation δ is expressed as,

$$\delta = \frac{F}{\pi E^{*} L} \ln\left[\left(\frac{4\pi E^{*} \Delta R}{F / L}\right) - 1\right] \tag{3.4}$$

$$\frac{1}{E^{*}} = \frac{1-\nu_1^2}{E_1} + \frac{1-\nu_2^2}{E_2} \tag{3.5}$$

$$\Delta R = R_i + R_j \tag{3.6}$$

In the above set of equations, F is the load acting on the bodies. L is the length of the cylinders, E^{*} is the equivalent modulus of elasticity which can be calculated if Poisson's ratios ($\nu_1$and ν_2) and elasticity moduli (E_1 and E_2) of the corresponding materials are known. R_i and R_j are the radii of the contacting cylinders (Figure 3-2).

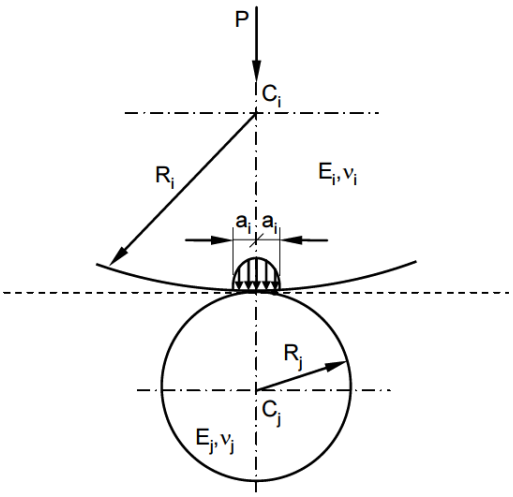

Figure 3-2 Cylinder to cylinder contact

In another set of formulas proposed by Radzimovsky indentation δ is given as,

$$\delta = \frac{F}{\pi E^{*} L}\left[\frac{2}{3} + \ln\left(\frac{4R_i}{b}\right) + \ln\left(\frac{4R_j}{b}\right)\right] \tag{3.7}$$

$$b = 1.60\left(\frac{(F/L)R}{E^{*}}\right)^{1/2} \tag{3.8}$$

$$R = \frac{R_i R_j}{R_i + R_j} \tag{3.9}$$

Lankarani and Nikravesh suggested the following explicit formula with a force exponent $n = 1$ to 1.5 for cylindrical contact.

$$\delta = \left\lceil \frac{3(F/L)}{4\pi E^* R^{1/2}} \right\rceil^{1/n} \tag{3.10}$$

Note that, deflections are all implicit functions of the term unit *F/L* (force per length). Furthermore, they are functions of the radii of the corresponding curvatures. These radii correspond to radii of curvature of the pinion and the gear teeth in a meshing spur gear pair. However, the radii of curvature of both pinion and gear change as the contact point travels along the line of action. This means that the Hertzian stiffness is not constant but changes its value as the point of contact travels along the line of action.

In order to compute the variation of the radii of curvatures, some background information regarding involute gear geometry needs to be introduced.
The derivations that follow are applicable to gear pairs that have a contact ratio which is less than two. The gear pairs that have a higher contact ratio than two are called high contact ratio gears. High contact ratio gear pairs are not in the scope of this study.

During a complete mesh cycle, gear pairs undergo different contact regimes which are double tooth contact and single tooth contact. As the names imply, the single tooth contact zone refers to the zone where one pair of gear tooth is engaged whereas in the double tooth contact zone, there are two pairs of gear tooth that are engaged. Note that in Figure 3-3, gear 1 is taken as the driver and gear 2 is taken as the driven gear. For the common speed reduction application, gear 1 is also called the pinion and gear 2 is called the gear.

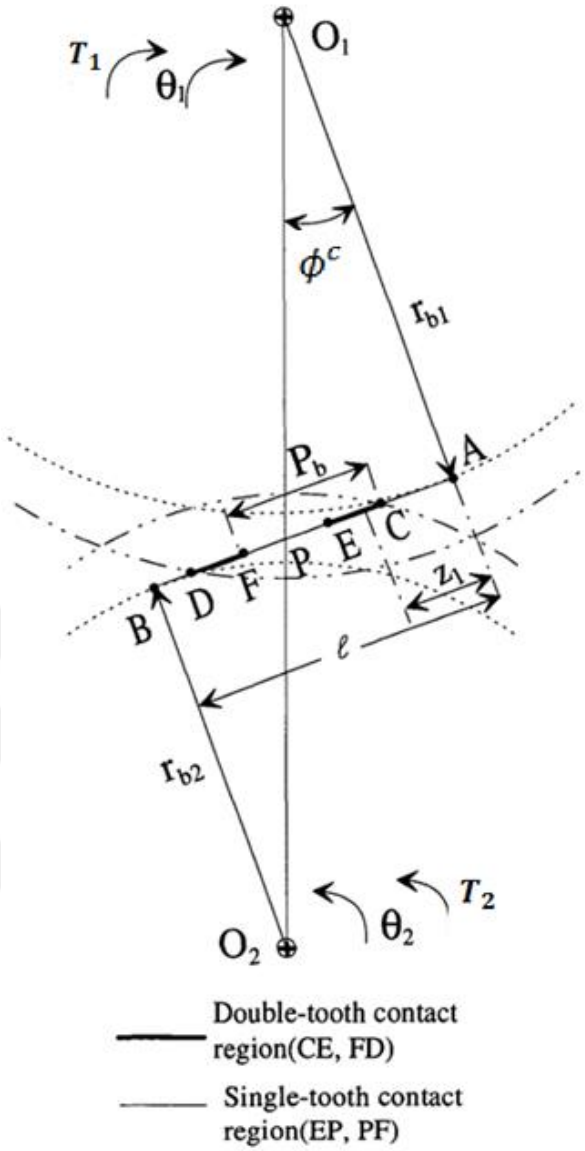

Figure 3-3 Contact points along the line of action [13]

The radii of base circles of gear 1 and gear 2 are designated as r_{b1} and r_{b2}; the radii of addendum circles are designated as r_{a1} and r_{a2} respectively. The angle ϕ^c is called the rack cutter pressure angle. This angle is usually 20° for common applications.

The location of single tooth and double tooth contact points can be determined by simple geometry.

$$AB = (r_{b1} + r_{b2}) \tan \phi^c \tag{3.11}$$

$$AC = AB - \sqrt{r_{a2}^2 - r_{b2}^2} \tag{3.12}$$

$$AD = \sqrt{r_{a1}^2 - r_{b1}^2} \tag{3.13}$$

$$AE = AD - p_b \tag{3.14}$$

$$AF = AC + p_b \tag{3.15}$$

In the above equations p_b is called the base circle pitch and it is given as,

$$p_b = \pi m \cos \phi^c \tag{3.16}$$

where m is the module.

Referring to Figure 3-3, the contact of a driver gear tooth with the driven gear tooth starts at point C. At this instant, there is another tooth pair in contact at point F. As the contact point, which was at point C, travels along the line of action, it comes to point E where the double tooth zone ends. At this instant, the tooth pair at point D have been separated from each other hence the single tooth contact zone begins. Single tooth contact zone continues from point E to point F. When the tooth arrives at point F, another gear tooth has made contact at point C, hence there is another double tooth contact zone until the tooth separates at point D. One complete mesh cycle of a gear tooth refers to the travelling of one gear tooth from point C to point D. Based on this explanation, regions CE and FD are called double tooth contact zones and region EF is called the single tooth contact zone. There is another important point called the pitch point P. It is the point where the pitch diameters intersect. Pitch point has a special kinematic importance which will be explained in Chapter 4.

In order to determine the instantaneous radii of curvatures along the line of action, two new angle definitions are needed.ϕ_{ij} is called the instantaneous pressure angle and α_{ij} is called the roll angle. The instantaneous pressure angle should not be confused with the rack cutter pressure angle ϕ^c which is constant and usually 20°.

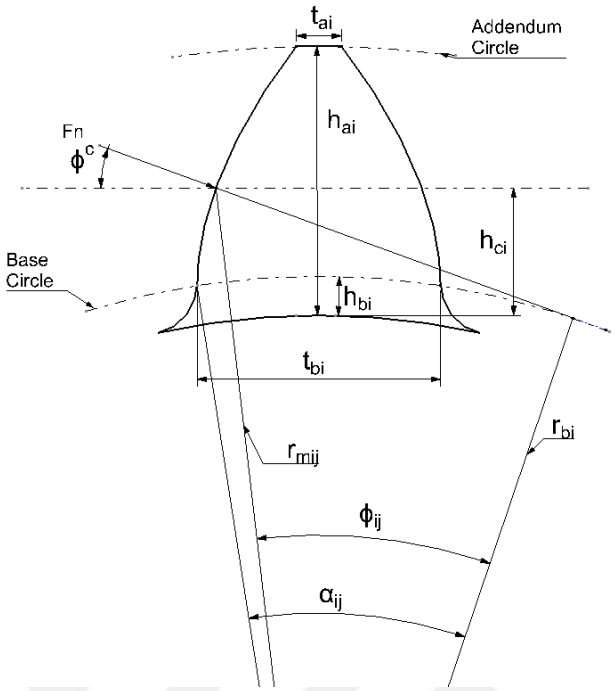

Figure 3-4 Instantaneous pressure angle and roll angle

From the above figure,

$$\cos \phi_{ij} = \frac{r_{bj}}{r_{mjj}} \tag{3.17}$$

Furthermore, the involute property relations give [13],

$$\alpha_{ij} = \tan \phi_{ij} \tag{3.18}$$

During a mesh cycle in a double tooth contact instant; there are four possible pressure angles and consequently roll angles: Two roll angles for the driver gear teeth and two roll angles for the driven gear teeth. The subscripts are used to differentiate which tooth of the mentioned gear is specified. According to the notation followed in [18] and also in this thesis, the subscript "*i*" refers to the gear number of interest and the subscript "*j*" refers to the tooth number of interest (Figure 3-5). Driver gear is represented as gear 1 hence the corresponding "*i*" subscript of the driver is 1. Consecutively "*i*" subscript of the driven gear is gear 2.

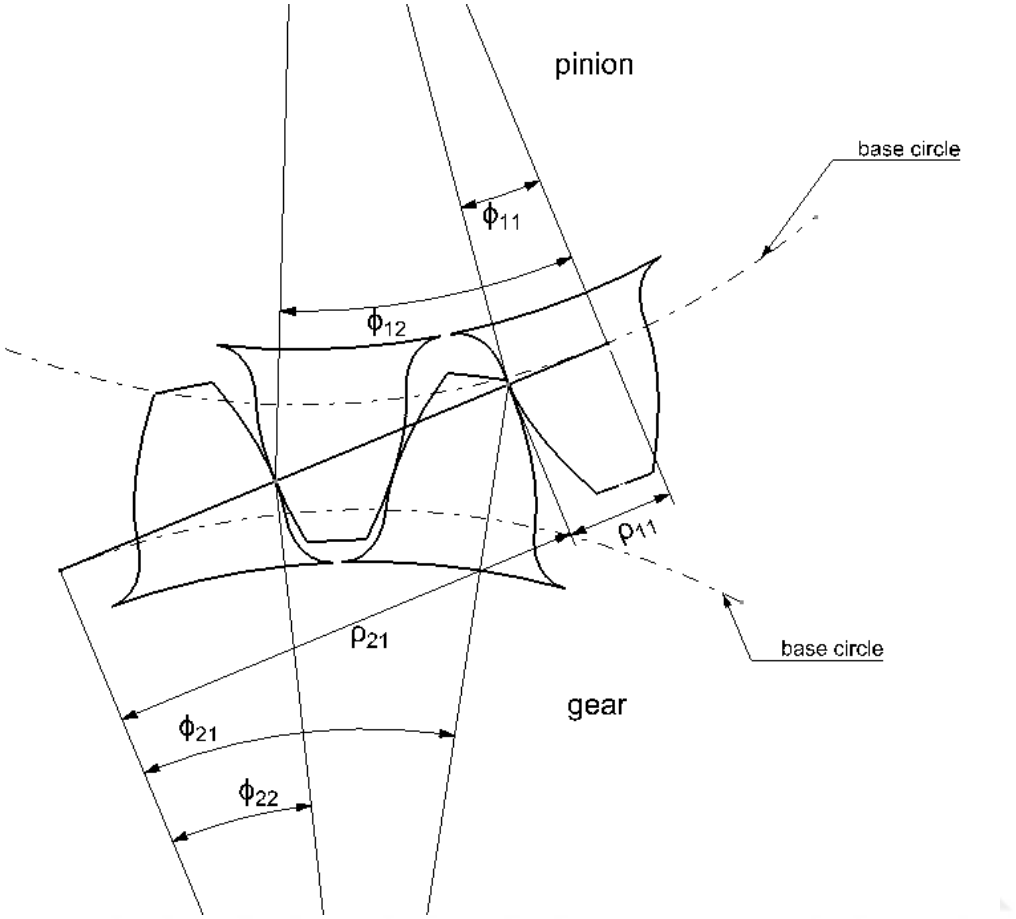

Figure 3-5 Illustration of pressure angle subscripts

In Figure 3-5, ρ_{11} and ρ_{21} represent the pinion and gear radii of curvatures of the first contacting teeth respectively. The following formulas can be used to calculate their value [22]:

$$\rho_{11} = (r_{m11}^2 - \frac{d_b^2}{4})^2 \tag{3.19}$$

$$\rho_{21} = (r_{m21}^2 - \frac{D_b^2}{4})^2 \tag{3.20}$$

The roll angle and the corresponding rotation angle θ_1 relation can be found with the aid of Figure 3-6 as;

$$\alpha_{11} = \theta_1 + \frac{AC}{r_{b1}} \tag{3.21}$$

$$\alpha_{21} = \frac{AB - \alpha_{11} r_{b1}}{r_{b2}} \tag{3.22}$$

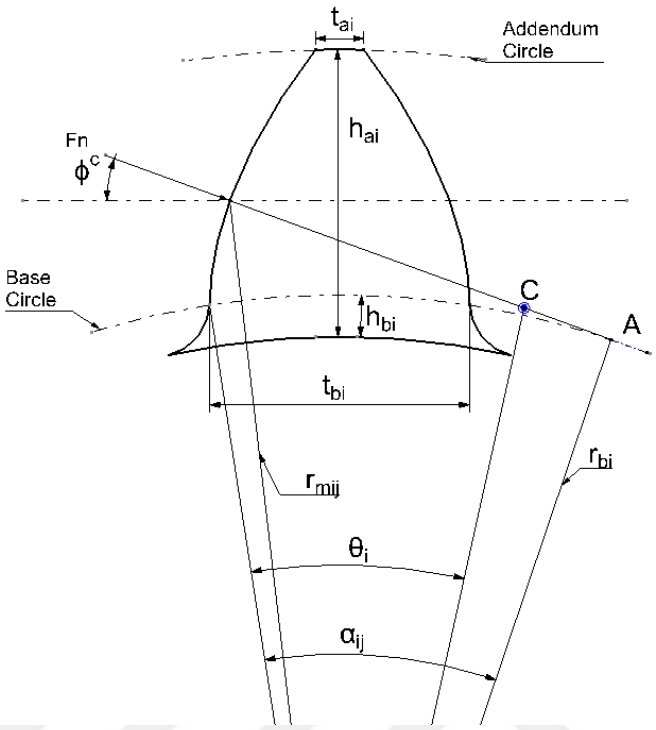

Figure 3-6 Rotation angle, pressure angle and roll angle relation [18]

Furthermore, due to base pitch definition;

$$\alpha_{12} = \alpha_{11} + \frac{p_b}{r_{b1}} \tag{3.23}$$

$$\alpha_{22} = \alpha_{21} - \frac{p_b}{r_{b2}} \tag{3.24}$$

However, note that Equation (3.23) and (3.24) are valid only when α_{11} is in approach section.

To sum up, if the angular position θ_1 of the driver gear is known for every instant, (which is usually obtained during a simulation) the corresponding roll angles α_{ij} of all four contacting teeth can be obtained via Eqs. (3.21)-(3.24). Then; by using Eqs. (3.18) and (3.17), one can compute the corresponding pressure angles ϕ_{ij} and the instantaneous radial distances r_{mij} respectively. Substitution of r_{mij} values into Eqs. (3.19) and (3.20) will yield the instantaneous variation of radii of curvatures of the pinion and gear along the line of action.

In order to demonstrate the difference of various contact models, an example gear pair from [18] will be used as a benchmark case study. The gear parameters are given in Table 2.

Table 2 Example gear pair parameters

	Pinion, Gear
Module (mm)	2
Number of teeth	20, 80
Addendum modification coefficient	0,0
Inertia (kg-m^2)	1.5285E-5, 3.9E-4
Elasticity modulus (GPa)	206.8
Poisson's ratio	0.3
Rack cutter pressure angle (°)	20
Face-width (m)	0.01
Backlash (m)	0.00005
Contact ratio	1.69
Damping ratio	0.05

The deflections given by different models under a unit load ($F_n = 1$) are computed with respect to the rotation angle $\theta_1$as given in Figure 3-7. Instantaneous $R_i$and R_j values required in these equations are computed by using Eqs. (3.19) and (3.20).

The driver gear 1 is rotated such that it undergoes a complete mesh cycle. In other words, contact point starts at point C and ends at point D.

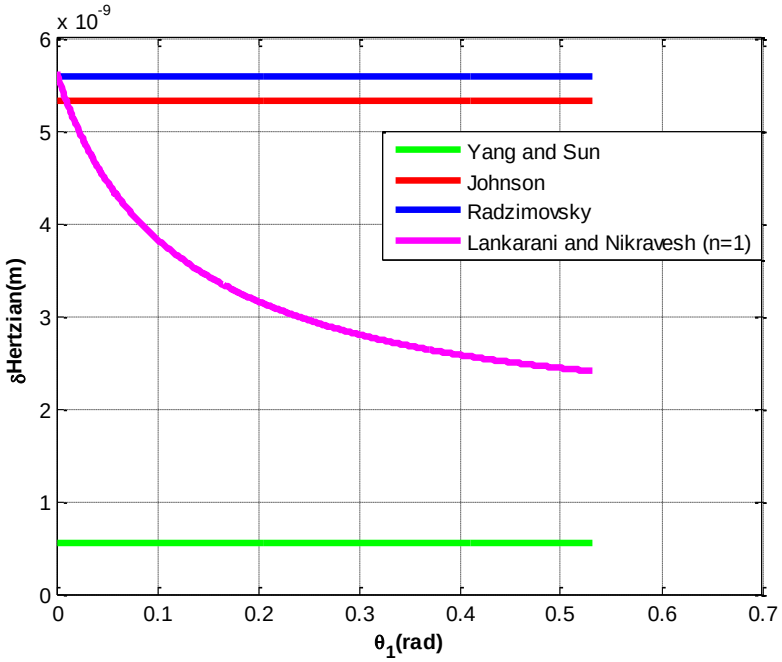

Figure 3-7 Different Contact Models vs. $\boldsymbol{\theta_1}$(rad)

It is interesting to note that despite both the pinion and gear radii of curvature are treated as variable, both Johnson and Radzimovsky models predict a constant deflection like Yang and Sun. What is more interesting is the fact that the amount of deflection predicted by Yang and Sun is almost ten times less than these aforementioned models. This means that these models which are more specifically tailored for cylinder to cylinder contact, predict a significantly lower Hertzian stiffness. Lankarani and Nikravesh model is the only model that predicts a deflection variation due to variable radii of curvature. However, the force exponent term $n = 1$ to $n = 1.5$ in this model causes a wide range of deflection values and it is difficult to judge which value for *n* should be used.

Due to the fact that the discrepancy among these four contact models is substantial, another verification with the literature is necessary in order to be able to select and justify a contact model to be used in the dynamic analysis. Another analytical Hertzian deflection formulation specifically derived for spur gears in a PhD thesis conducted at MIT in 1956 [23] uses complex potential functions and integration of stresses and strains along the common normal. The results of this study is given in Figure 3-8. The deflection values are plotted for various equivalent gear numbers of

teeth i_e. Note that both horizontal and vertical axes are non-dimensionalized. The vertical axis is the amount of Hertzian deflection divided by the base pitch p_n. The horizontal axis is the non dimensional normal load where the term W_o is the force per unit length and *E* is the modulus of elasticity. The linear approximations for different i_e values are also tabulated.

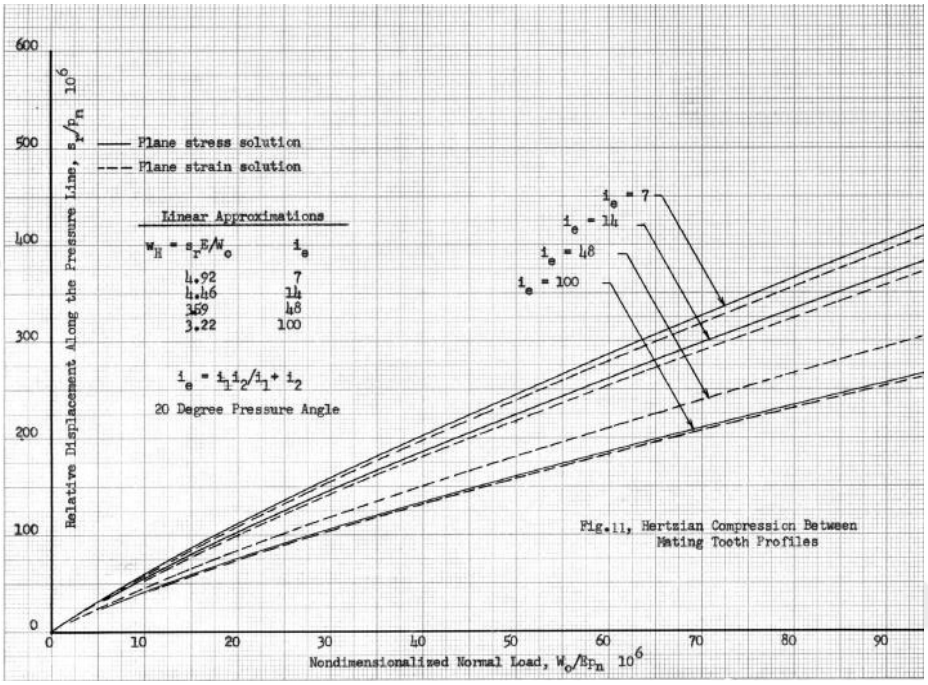

Figure 3-8 Non-dimensionalized Hertzian deflection [23]

For comparison purposes, the formulations of Johnson, Radzimovsky and Yang-Sun are also plotted in this non dimensional form by performing the necessary manipulations. As can be seen in Figure 3-9, Radzimovsky's and Johnson's predictions behave more similar to the results shown in Figure 3-8.

In the light of the given data and comparisons, the following conclusions can be deducted.

- For all of the contact points along the line of action, the total contact deformation for a tooth pair can be considered as constant under a constant load. During rotation, at the contact point, radius of curvature of the driver tooth increases, and radius of curvature of the driven tooth decreases; their sum being constant. This results in a constant deformation along the line of action, when deformations are calculated by using the equations which have *sum of the radius of curvature* values as input parameters.

- Thus, the stiffness values for practical range can be treated as constant which is a result of the fact that deformation and normal load variation is almost linear as seen in Figure 3-8 and 3-9.
- Johnson's and Radzimovsky's deformation models, although they are for general cylinder to cylinder contact, predict the gear mesh deformation values in accordance with [23], hence it can be concluded that, while constructing the dynamical model, one of these models should be selected rather than Lankarani-Nikravesh or Yang-Sun deformation formulations.

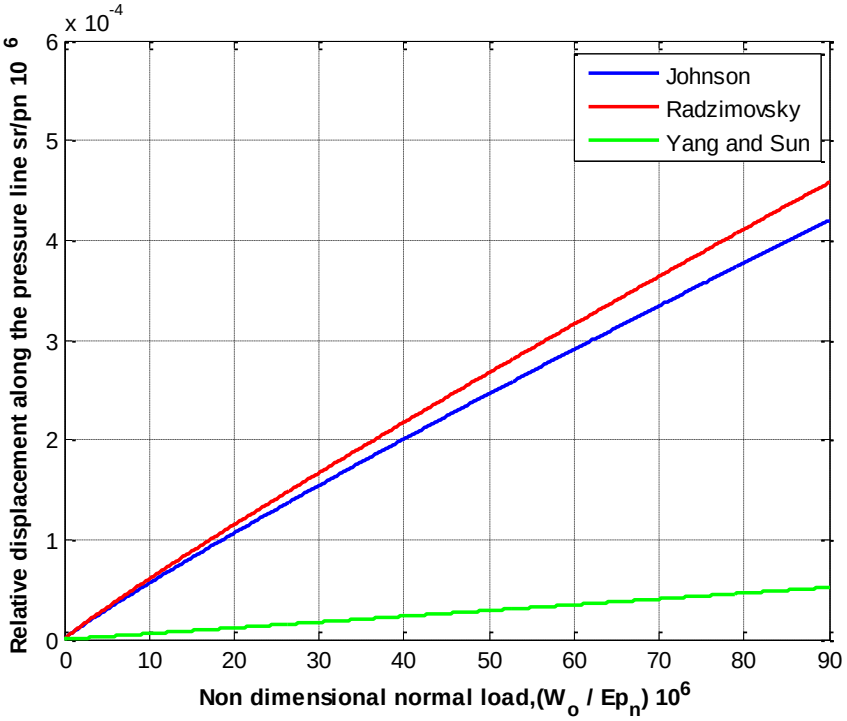

Figure 3-9 Hertzian Deflections for $\boldsymbol{i_e = 7}$

3.2.2 Gear Body Deflection Models

A gear tooth under a normal load F_n, will deflect as shown in Figure 3-10.

The factors that contribute to gear body deformations can be classified into four categories [23].

- Tooth bending as a cantilever beam
- Shear deformation due to tangential load
- Compression deformation due to radial load
- The deformations of the foundation (gear hub or rim)

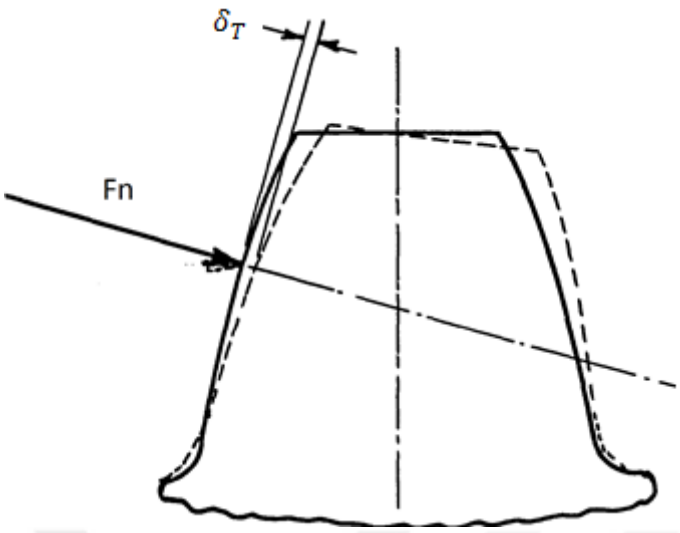

Figure 3-10 Deformation of a gear tooth [18]

The deflection contributions from each category need to be superimposed onto the Hertzian local deflection value to find the overall deformation δ_T along the line of action. The total deflection amount under a unit load of 1 N, is defined as the mesh compliance of a single gear tooth. Compliance is again a function of the rotation angle because as the point of contact travels along the line of action, different deflections are going to be obtained. Hence this variation of compliance for different contact positions will be elaborated.

The gear tooth can be approximated as a cantilever trapezoidal beam plus a cantilever rectangular beam as is done in [18]. The rectangular section is the portion between the dedendum circle and base circle. Trapezoidal section is the portion between addendum circle and base circle (Figure 3-11). Note however that, if the dedendum diameter is greater than the base circle diameter the rectangular portion vanishes.

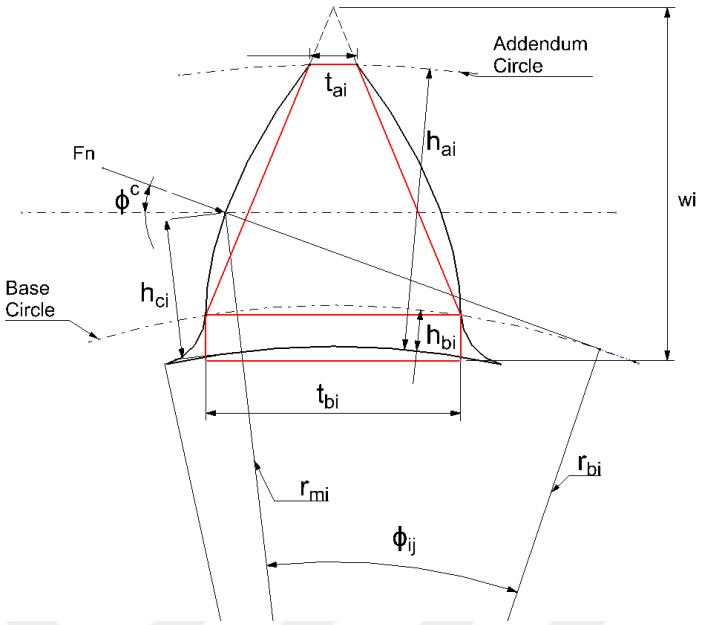

Figure 3-11 Cantilever trapezoidal beam approximation

The total deformation amount along the line of action is found by superposition of each deformation.

$$\delta_T = \delta_{bp} + \delta_{bn} + \delta_s + \delta_f + \delta_H \tag{3.25}$$

In the above equation, δ_{bp} is the deformation due to bending from $F_n cos\phi^c$ component.

δ_{bn} is the deformation term due to bending from $F_n sin\phi^c$ component.

δ_s is the deformation term due to shear force.

δ_f is the deformation of the foundation.

δ_H is the deformation term due to Hertzian contact.

$$\delta_{bpj} = \frac{12F_n cos\varnothing_c^2 h_{bi}}{Eft_{bi}^3}\left(h_{ci}^2 + \frac{h_{bi}^2}{3} - h_{ci}h_{bi}\right) + \frac{6F_n \cos\varnothing_c^2 (w_i - h_{bi})^3}{Eft_{bi}^3}$$

$$\times\left[\frac{w_i - h_{ci}}{w_i - h_{bi}}\left(4 - \frac{w_i - h_{ci}}{w_i - h_{bi}}\right) - 2\ln\frac{w_i - h_{ci}}{w_i - h_{bi}} - 3\right] \tag{3.26}$$

$$\delta_{bni} = \frac{3F_n \cos\varnothing_c \sin\varnothing_c h_{bi}}{Eft_{bi}^2}\left[\frac{h_{bi}(h_{bi} - 2h_{ci})(w_i - h_{ci})}{w_i - h_{bi}} - (h_{ci} - h_{bi})^2\right] \tag{3.27}$$

$$\delta_{si} = \frac{1.2F_n \cos\varnothing_c^2}{G f t_{bi}} \left[h_{bi} + (w_i - h_{bi}) \ln \frac{w_i - h_{ci}}{w_i - h_{bi}} \right] \tag{3.28}$$

$$\delta_{fi} = \frac{24F_n \cos\varnothing_c^2 h_{ci}^2}{\pi E f t_{bi}^3} \tag{3.29}$$

In the above equations, E is the modulus of elasticity, f is the face width of the related gear, G is the modulus of rigidity and δ_H is the Hertzian deflection contribution as explained in section 2.2.1. Furthermore, note that $w_i, h_{ai}, h_{bi}, \phi_c$ are constants whereas h_{ci} varies as the point of contact travels along the line of action.

$$w_i = \frac{h_{ai}t_{bi} - h_{bi}t_{ai}}{t_{bi} - t_{ai}} \tag{3.30}$$

The variation of the contact height h_{ci} can be computed again using gear geometry (Figure 3-12) with the following equation.

$$h_{ci} = r_{mi} \cos\gamma_m - r_{di} \tag{3.31}$$

In the above equation, r_{mi} is obtained via Eq (2.7), and r_{di} is the dedendum radius. The angle γ_m can be computed as follows.

$$\gamma_{mi} = \frac{1}{2} \left[\frac{t_{pi}}{r_{pi}} + 2(inv\phi^c - inv\phi_{ij}) \right] \tag{3.32}$$

$$t_{pi} = \frac{\pi m}{2} + 2mx_i \tan\phi^c \tag{3.33}$$

$$r_{pi} = \frac{mN_i}{2} \tag{3.34}$$

$$inv(x) = \tan(x) - x \tag{3.35}$$

In the above set of equations, *inv* is the involute function, r_{pi} is the radius of the pitch circle of the i^{th} gear, N_i is the number of teeth of the i^{th} gear, t_{pi} is the circular tooth thickness of the i^{th} gear at the pitch diameter, x_i is the addendum modification coefficient of the i^{th} gear.

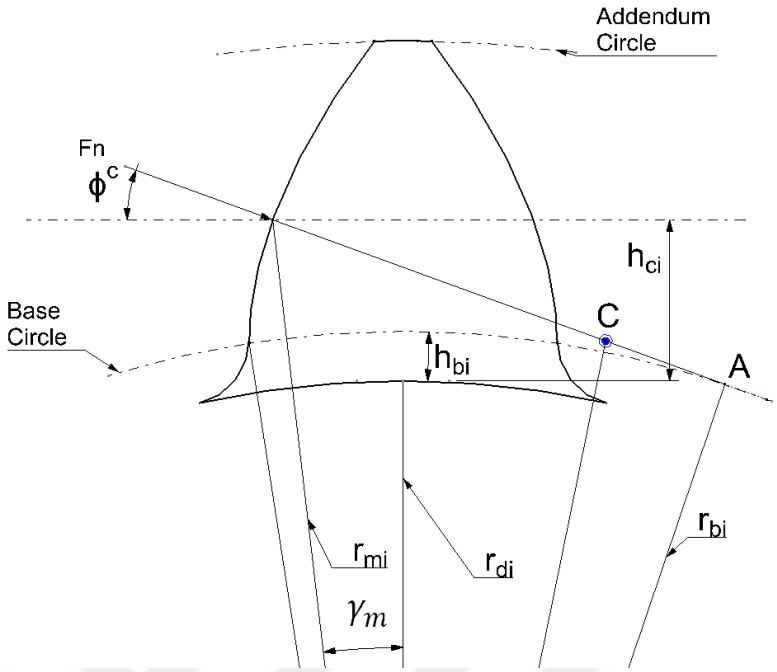

Figure 3-12 Contact height h_{ci}

Based on the above information; the variation of h_{ci} can be computed along the line of action for each contact position. By implementing this variation to the deflection Eqs. (3.25)-(3.29); one can find the deflection for each contact position. Finally, stiffness of i^{th} gear can be computed as;

$$k_i = \frac{F_n}{\delta_T} \tag{3.36}$$

The deflection variations from point C to point F for the example gear pair given in Table 2 are computed and plotted as was done in [18].

As can be seen in Figure 3-13 and Figure 3-14 the results are in excellent agreement which shows that the complicated deflection equations were implemented correctly.

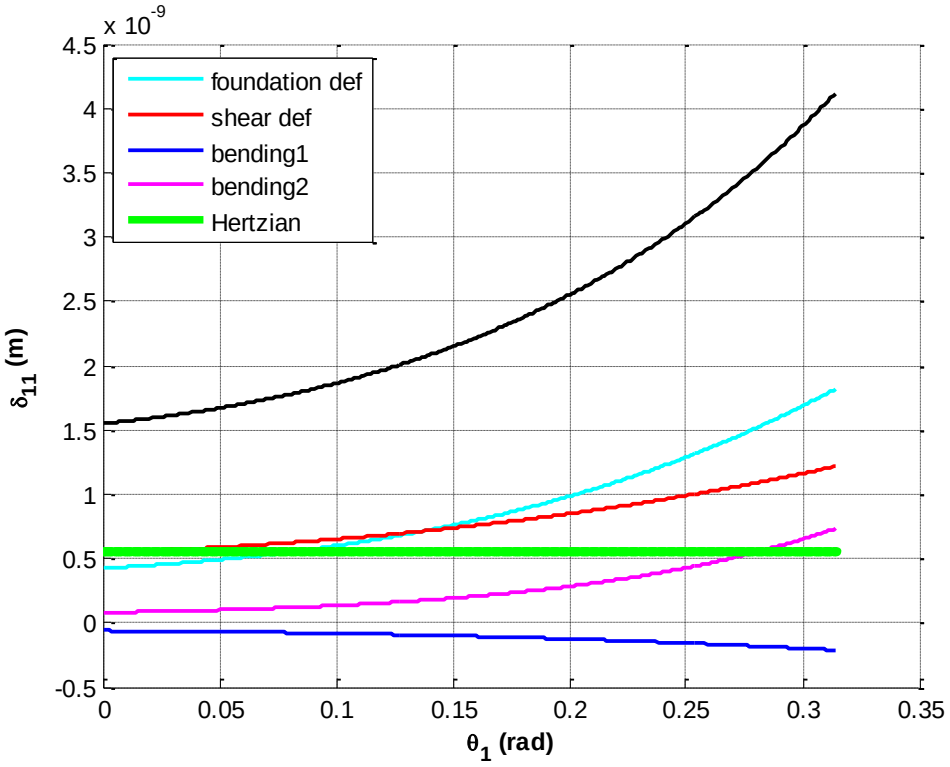

Figure 3-13 Deflection variations of the 1st tooth of the driver gear

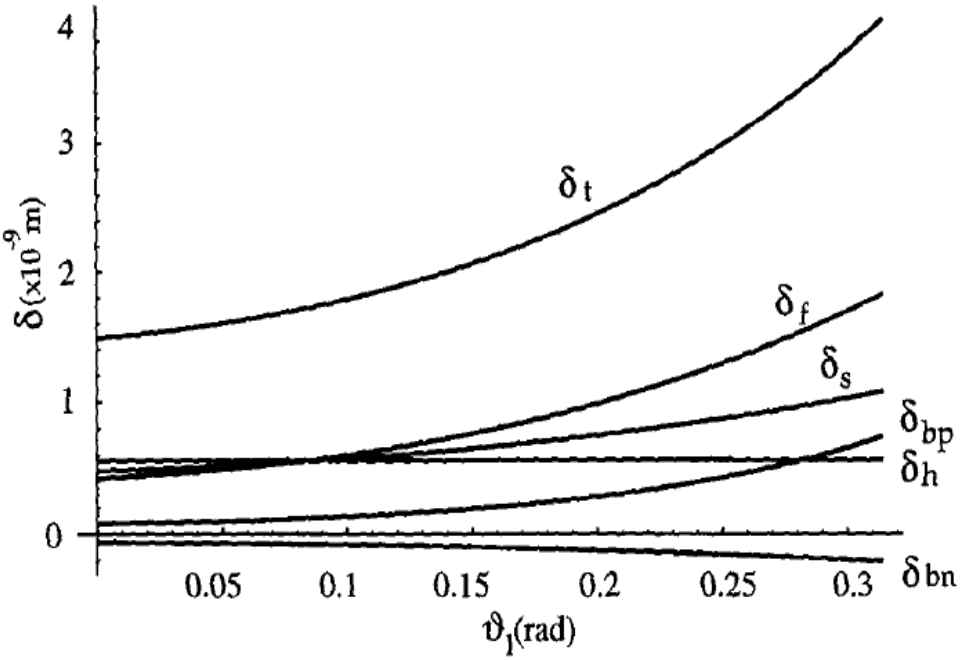

Figure 3-14 Deflection variations of the 1st tooth of the driver gear [18]

Under a unit normal load F_n, the reciprocal of the total deflection gives the stiffness of a single tooth. Since the variation of the stiffness values can be calculated for both

driver and driven gears, the combined stiffness of the contacting tooth pair can also be computed since they behave as springs which are connected in series.

$$k_{combined1} = \frac{k_{11}k_{21}}{k_{11} + k_{21}} \tag{3.37}$$

In gear dynamics literature, the variations are computed with respect to roll angle of the 1st tooth of the first gear traditionally. This is due to fact that the roll angle reveals the starting and ending points of single tooth contact and double tooth contact zones. In Figure 3-15, the variation of these stiffness values for the example gear pair of Table 2 can be seen.

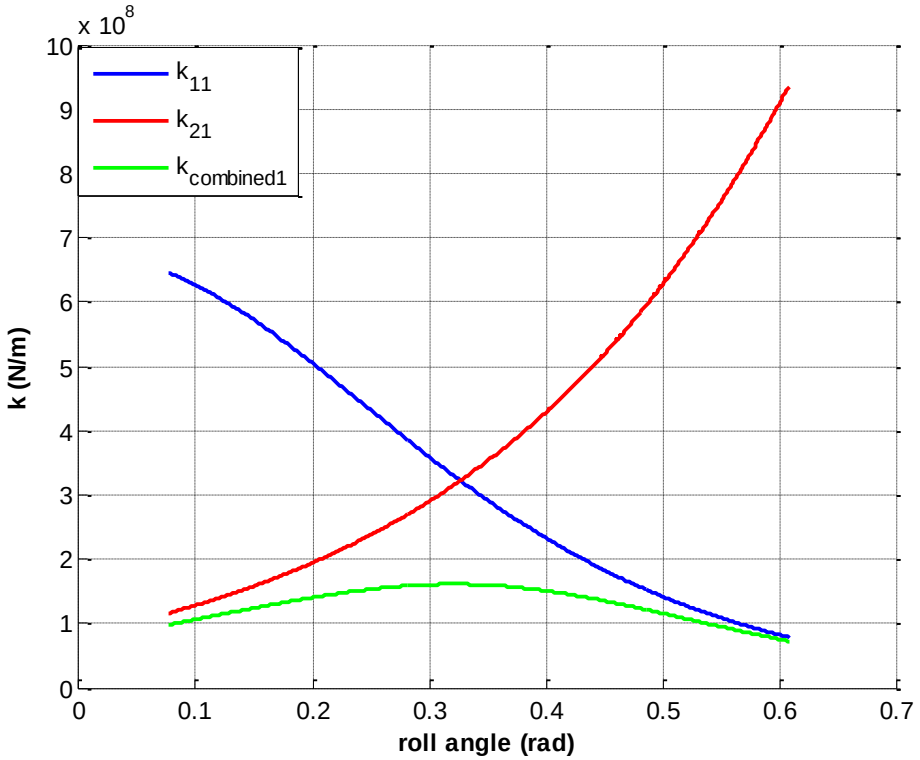

Figure 3-15 Stiffness variations vs. roll angle - Shing and Tsai

Another mesh stiffness formula which was obtained via curve fitting by Kuang and Yang [24] as cited in [12, 20] in terms of the radial distance of the contacting point to the rotation center (r_{mi}) is given.

$$k_i(r_{mi}) = (A_0 + A_1 X_i) + (A_2 + A_3 X_i)\left[\frac{r_{mi} - r_{pi}}{(1 + X_i)m}\right] \tag{3.38}$$

$$A_0 = 3.867 + 1.612 N_i - 0.02916 N_i^2 + 0.0001553 N_i^3 \tag{3.39}$$

$$A_1 = 17.06 + 0.729N_i - 0.01728N_i^2 + 0.0000999N_i^3 \quad (3.40)$$

$$A_2 = 2.637 - 1.222N_i + 0.02217N_i^2 - 0.0001179N_i^3 \quad (3.41)$$

$$A_3 = -6.330 - 1.033N_i + 0.02068N_i^2 - 0.0001130N_i^3 \quad (3.42)$$

In the above set of equations, r_{pi} is the pitch radius of the i^{th} gear in mm, X_i is the addendum modification coefficient of the i^{th} gear, m is the module in mm, N_i is the number of teeth of the i^{th} gear. As always, the 1st gear is the driver gear and the second gear is the driven gear. Implementation of the mesh stiffness model to the benchmark example gear pair of Table 2, the following variations are achieved.

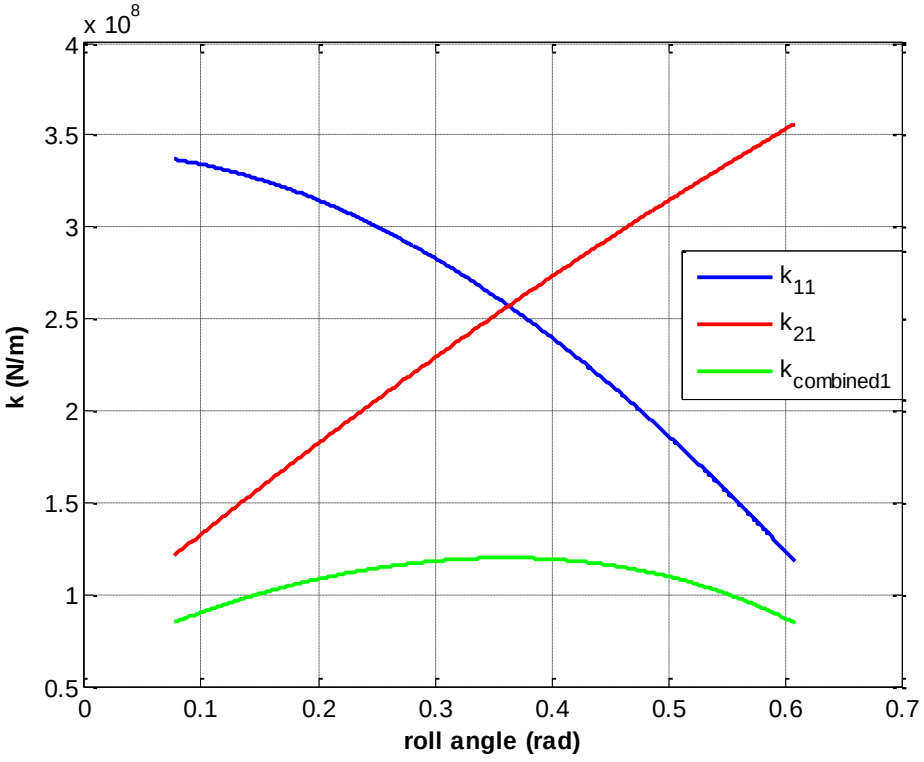

Figure 3-16 Stiffness variations vs. roll angle - Kuang and Yang

By comparing Figure 3-15 and Figure 3-16, it can be seen that the stiffness predictions of the models are significantly different from each other.

Fortunately, ISO 6336-1 International Standard [25] also gives equations for estimation of the average constant mesh stiffness of any given combined tooth pair. Based on the theory of elasticity and previous works of several authors, the standard also incorporates correction factors that enable better accuracy. The formula is valid

for external cylindrical gears that have a basic rack profile according to ISO 53. The reader can refer to ISO 6336-1 clause 9.3 for the equations that are used to calculate the mesh stiffness. ISO 6336-1 equations are implemented to the benchmark gear pair (Table 2) and the results are compared with the previous mesh stiffness models as shown in Figure 3-17.

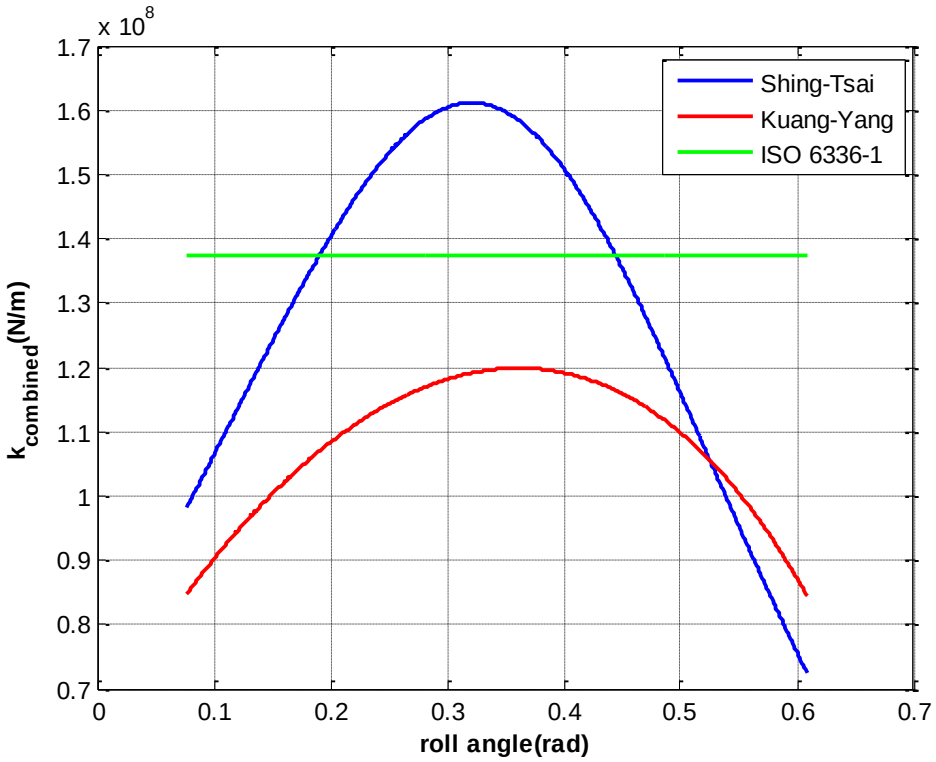

Figure 3-17 Combined stiffness variation of a tooth pair

As can be seen in the above figure, Kuang-Yang model predicts a smaller stiffness than Shing-Tsai model. Furthermore Shing-Tsai model is closer to ISO 6336-1 if the average values of both models are considered. It can be concluded that all three models predict the mesh stiffness' order of magnitude as 10^8 N/m. These models need to be investigated independently for particular applications and their compliance with the ISO 6336-1 formulation should be checked for individual gear pairs accordingly. However it is concluded that ISO 6336-1 can be taken as the benchmark for further dynamic studies.

3.3 Gear Damping Coefficient

This term takes into account the energy dissipation which occurs during impact and it produces a corresponding contact force which is a function of the relative penetration velocity $\dot{\delta}$.

Like stiffness, there are also many different models that estimate the damping coefficient however due to the complexity of the energy dissipation phenomenon, the formulas are usually empirical or they depend on the coefficient of restitution.

Lankarani and Nikravesh [26] propose the following damping hysteresis coefficient, which is a function of the penetration depth δ, initial impact velocity $\dot{\delta}^{(-)}$, coefficient of restitution c_e and stiffness *K*.

$$D = X \delta^{n} \tag{3.43}$$

$$X = \frac{3K(1 - c_e^2)}{4\dot{\delta}^{(-)}} \tag{3.44}$$

Then the total contact force based on the above expression becomes:

$$F = K\delta^{n} + D\dot{\delta} \tag{3.45}$$

Note that this expression produces a non-zero dissipative force at zero penetration depth, at the time of separation. Hence Azar and Crossley [27] proposed a non-linear relation in the form of

$$F = K\delta^{n} + D\delta\dot{\delta} \tag{3.46}$$

Yang and Sun [17] extended that model for spur gears and came up with the following formula where they fit a curve to Goldsmith's coefficient of restitution experimental data.

$$D = \frac{6(1 - c_e)}{\left[(2c_e - 1)^2 + 3\right]} \frac{K}{\dot{\delta}^{(-)}} \tag{3.47}$$

$$c_e = 1 - 0.022\dot{\delta}^{(-)0.36} \tag{3.48}$$

The above equation implies that the relative impact velocities at the instant of impact should be known in order to calculate the dissipative force values for forward dynamic analysis. The determination of the instantaneous penetration velocity is computationally expensive during a dynamical simulation. Considering this; a simple

damping model which was developed by Dubowsky and Freudenstein [28] is used in the gear dynamics study of Shing [18];

$$c = 2\xi\sqrt{k\,\frac{I_2 r_{b1}^2 + I_1 r_{b2}^2}{I_2 I_1}} \tag{3.49}$$

The above equation assumes that damping coefficient is constant and time independent. In the above equation, ξ is damping ratio, r_{b1} and r_{b2} are base circle radii of the gears, k is the mesh stiffness value, I_1 and I_2 are the mass moments of inertia of the gears.

CHAPTER 4

FIXED CENTER DISTANCE GEAR DYNAMICS

4.1 Introduction

In this chapter, gear dynamics will be investigated for gear pairs operating at fixed center distance. Even though the utilization of multi body dynamics programs such as MSC-Adams make complex dynamical simulations possible, a theoretical investigation is necessary to be used as a comparison tool in order to check the validity of the developed multibody dynamics models.

Two distinct MATLAB Simulink models have been developed for this purpose. The first model can be considered as a forward dynamics problem in which the torque values at the input and output shafts are known. The angular acceleration, angular velocity and angular displacements of the gears need to be computed for the given torques. In this problem the non-linearity induced by the backlash needs to be included in the model.

The second developed model is an inverse dynamics model in which the input angular velocity is constant regardless of the excitation from the mesh stiffness and there is a constant resistance torque at the output shaft. In order to realize this motion, the torque at the input shaft needs to vary with respect to time. This model is used for the computation of dynamic factor for different input angular velocities and used for frequency response characteristics.

4.2 Equations of Motion of a Gear Pair with Backlash-Forward Dynamics

In the subsequent equations I_1 and I_2 are the mass moments of inertia of the gears, T_1 is the driving motor torque, T_2 is the resistance torque, θ_1 and θ_2 are the angular positions of the driving and driven gear and r_{b1} and r_{b2} are the base circle radii of the driving and driven gears respectively.

In Figure 4-1, a schematic of a gear pair that has an amount of backlash "*b*" is shown.

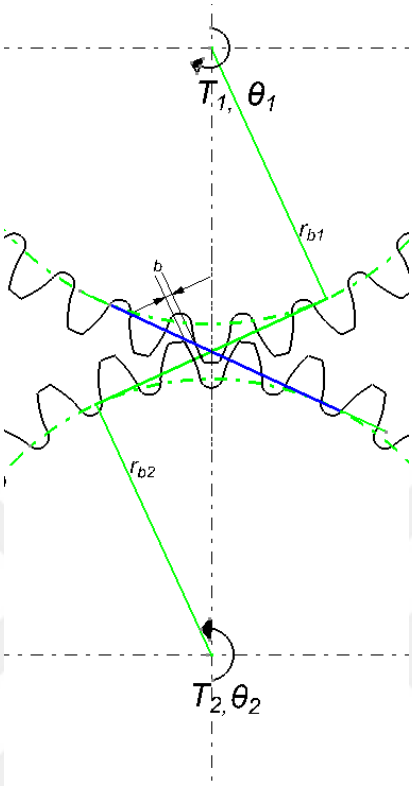

Figure 4-1 Gear meshing

Due to existence of backlash, there are three possible modes of operation depending on the location of the point of contact. If the driving gear rotates in the clock-wise direction and the driven gear rotates in the counter-clock wise direction, the contact is named as front side contact (Figure 4-2). On the contrary, if the driving gear rotates in the counter-clockwise direction while the driven gear rotates in the clock wise direction, back side contact occurs. When there is no contact among gear teeth, the gear pair is said to be in the separation region.

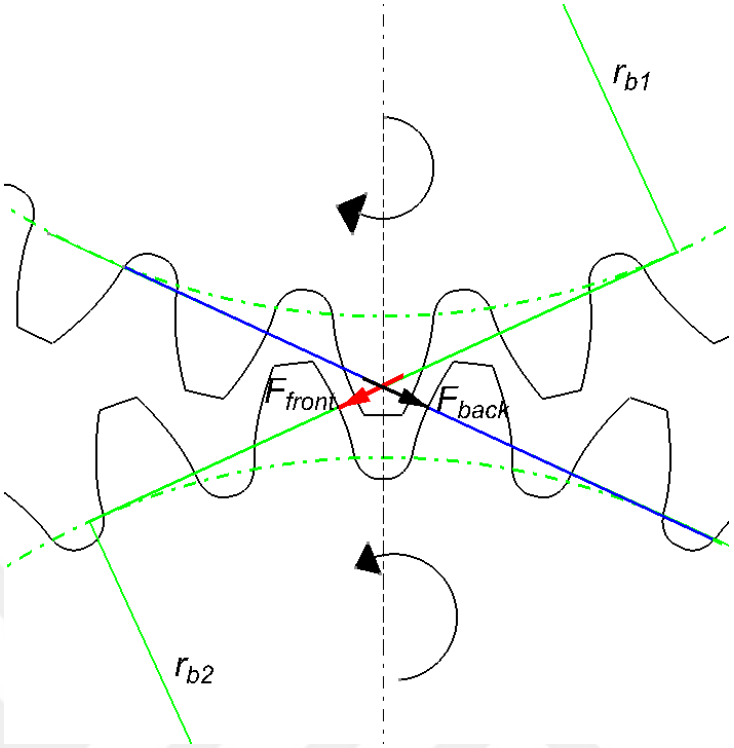

Figure 4-2 Illustration of front and back side contact

In the absence of backlash, when a gear rotates by an angle ϑ, the point of contact travels along the line of action by an amount of $r_b\vartheta$. Consequently, the penetration of one gear tooth into the corresponding gear tooth can be expressed as

$$\delta = r_{bi}\theta_i - r_{bj}\theta_j \tag{4.1}$$

For front side contact;

$$\delta_f = r_{b1}\theta_1 - r_{b2}\theta_2 \tag{4.2}$$

Whereas for backside contact;

$$\delta_b = r_{b2}\theta_2 - r_{b1}\theta_1 \tag{4.3}$$

When there is backlash, it can be incorporated into the equations as shown.

$$\delta_f = r_{b1}\theta_1 - r_{b2}\theta_2 - b \tag{4.4}$$

$$\delta_b = r_{b2}\theta_2 - r_{b1}\theta_1 - b \tag{4.5}$$

The contact force on gear teeth can then be expressed as explained in chapter 2.

$$F_n = k\delta + c\dot{\delta} \tag{4.6}$$

The equations of motions can be written for the three cases as shown.

- If $r_{b1}\theta_1 - r_{b2}\theta_2 > b$: front side contact occurs

$$T_1 - F_n r_{b1} = I_1 \ddot{\theta}_1 \tag{4.7}$$

$$T_2 + F_n r_{b2} = I_1 \ddot{\theta}_2 \tag{4.8}$$

- If $r_{b1}\theta_1 - r_{b2}\theta_2 < -b$: back side contact occurs

$$T_1 + F_n r_{b1} = I_1 \ddot{\theta}_1 \tag{4.9}$$

$$T_2 - F_n r_{b2} = I_1 \ddot{\theta}_2 \tag{4.10}$$

- If $-b < r_{b1}\theta_1 - r_{b2}\theta_2 < b$: separation occurs

$$T_1 = I_1 \ddot{\theta}_1 \tag{4.11}$$

$$T_2 = I_2 \ddot{\theta}_2 \tag{4.12}$$

Recall that a complete mesh cycle of a gear pair includes single tooth and double tooth contact zones. This effect must also be taken into account while deriving the equations of motion. For the sake of clarity, Figure 3-3 is repeated here as Figure 4-3. Regions CE and DF are double tooth contact regions; whereas region EF is the single tooth contact region.

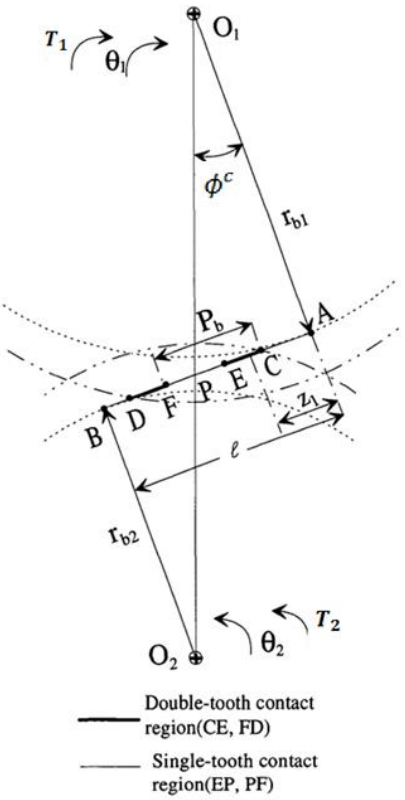

Figure 4-3 Rotational sign convention

During a dynamical simulation, the instantaneous position $\vartheta_1$is usually obtained by solving the coupled differential equations. By using Eqns. (3.18) and (3.21) the instantaneous pressure angle ϕ_{11} can be found. Then this angle can be used to determine whether a given instant is a single tooth or double tooth contact region. Using the geometrical relations developed in chapter 2;

$$\phi_C = \operatorname{atan}\left(\frac{AC}{r_{b1}}\right) \tag{4.13}$$

$$\phi_E = \operatorname{atan}\left(\frac{AE}{r_{b1}}\right) \tag{4.14}$$

$$\phi_F = \operatorname{atan}\left(\frac{AF}{r_{b1}}\right) \tag{4.15}$$

$$\phi_D = \operatorname{atan}\left(\frac{AD}{r_{b1}}\right) \tag{4.16}$$

- If $\phi_C < \phi_{11} < \phi_E$: double tooth zone

$$F_n = (k_1\delta + c\dot{\delta}) + (k_2\delta + c\dot{\delta}) \tag{4.17}$$

- If $\phi_E < \phi_{11} < \phi_F$: single tooth zone

$$F_n = (k_1\delta + c\dot{\delta}) \tag{4.18}$$

- If $\phi_F < \phi_{11} < \phi_D$: double tooth zone

$$F_n = (k_1\delta + c\dot{\delta}) + (k_2\delta + c\dot{\delta}) \tag{4.19}$$

It should be noted that the instantaneous pressure angle is a periodic function. After one complete mesh cycle, the point of contact returns to point C, where another tooth pair has started contact. This periodicity can be computed from

$$\alpha_{11} = \alpha_C + \operatorname{mod}(\alpha_{11}, \alpha_D) \tag{4.20}$$

By using the above equations, and by utilizing the methods explained in Chapter 3, MATLAB-Simulink model can be constructed.

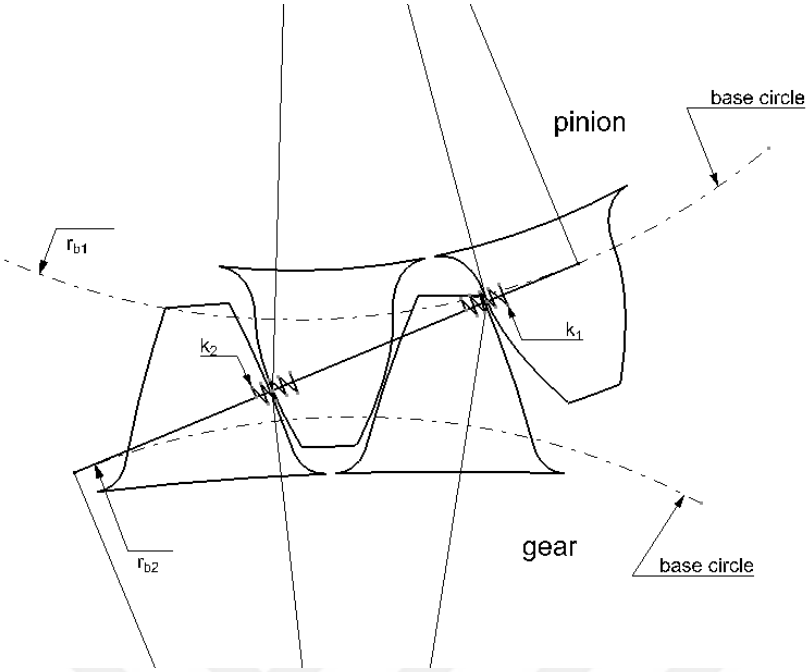

Figure 4-4 Double tooth contact region

4.3 Development of MATLAB-Simulink and MSC-Adams models

The same set of gear parameters given in Table 2 are used for comparing the developed dynamic model with the literature. There are two types of simulations performed, namely free oscillations and constant load. In the free oscillation mode, the driver gear has an initial angular velocity of 50 rad/s, while the driven gear is at rest. There is no external torque acting on the gears. Initially the gears are at their neutral position as depicted in Figure 4-1 which means that there is an initial backlash *b*.

In the constant load mode, the pinion external torque is $T_1 = 1$ Nm and the gear resistance torque is $T_2 = -1$ Nm. The driver again has an initial angular velocity of 50 rad/sec while the driven gear is at rest.

Since value of the mesh stiffness is taken as constant in [18], the same simplification is made for comparison purposes. The average mesh stiffness is taken as 1.39 N/m and the damping coefficient is taken as 237.7 Ns/m.

In Simulink, a variable step size ode45 (Dormand-Prince) solution scheme is used with a relative tolerance of $1x10^{-8}$. The minimum step size is set to $1x10^{-6}$ and the

maximum step size is set to $1x10^{-4}$. A screenshot of the developed model is available at Appendix C, Figure C1.

The dynamic model with the same set of gear parameters was also constructed in a previous work of the author in the multi body dynamics environment MSC Adams to verify the validity of the contact parameters [29] and the numerical solution capability of MSC-Adams. The equations of motions do not need to be derived and solved in MSC-Adams. The user simply creates the gears in an external CAD program, imports them into MSC-Adams in parasolid (x.t) format, and assigns the revolute joints and the inertia values. The development of this model is significantly easier than a MATLAB-Simulink model.

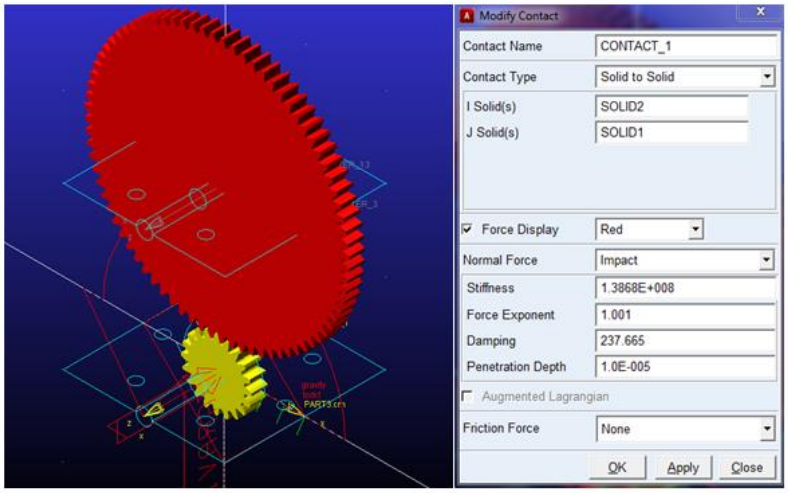

Figure 4-5 Screenshot of the MSC-Adams model [29]

The interaction of gears is provided by 3D contact command in MSC Adams. This command measures the instantaneous penetration depth $(x_0 - x)$ and the instantaneous penetration depth velocity $\dot{x}$ between two solids and the applied force is a function of those variables as well as the material related constants such as stiffness, damping, force exponent and penetration depth at which the damping value reaches its maximum.

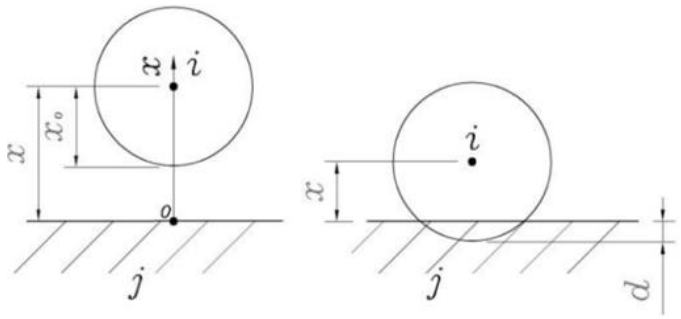

Figure 4-6 3D contact schematic in MSC Adams [30]

$$F_c = 0; (x - x_0) \geq 0 \tag{4.21}$$

$$F_c = K(x_0 - x)^e + c_{\max} \dot{x} STEP(x, x_0 - d, 1, x_0, 0); (x - x_0) < 0 \tag{4.22}$$

In order to equate Eq. (4.18) and (4.22), the force exponent *e* is taken as 1, and the penetration depth *d* is chosen a very small value so that c becomes constant rapidly. Stiffness and damping values are the same as the MATLAB model.

In MSC-Adams, simulation time is set as 0.02 seconds and number of steps is taken as 10000. Solver type is chosen as GSTIFF with a specified error of $1x10^{-8}$.The reason for selecting the step size so small is to be able to capture the transient dynamics accurately since the contact algorithm in MSC-Adams may sometimes yield inaccurate results due to the high stiffness of the system. The user should keep increasing the number of steps (or decrease the number of step size) until the response no longer varies with respect to the previous solution.

4.4 Simulation Results for Forward Dynamics

4.4.1 Free Oscillations

In Figure 4-7 and Figure 4-8, successive impacts (front side and back side contacts) and the effect of backlash can be clearly seen. In the separation regions, the angular velocities of both the driver and the driven gears remain constant. As time passes, the frequency of impacts becomes lower due to damping effects.

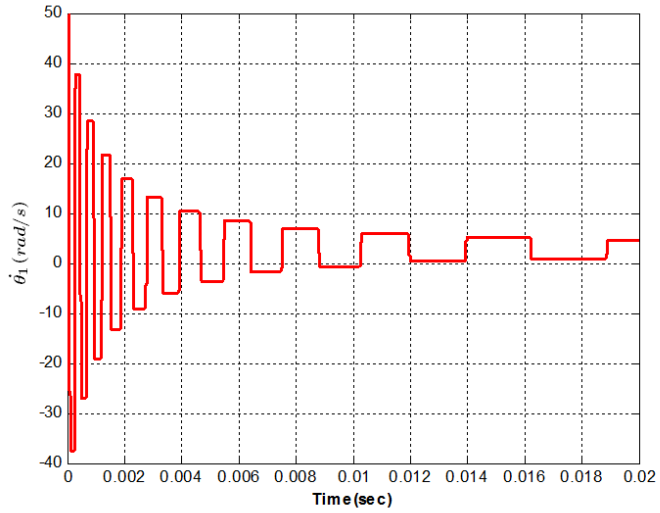

Figure 4-7 Angular velocity of gear 1 for free oscillation - MATLAB - Simulink

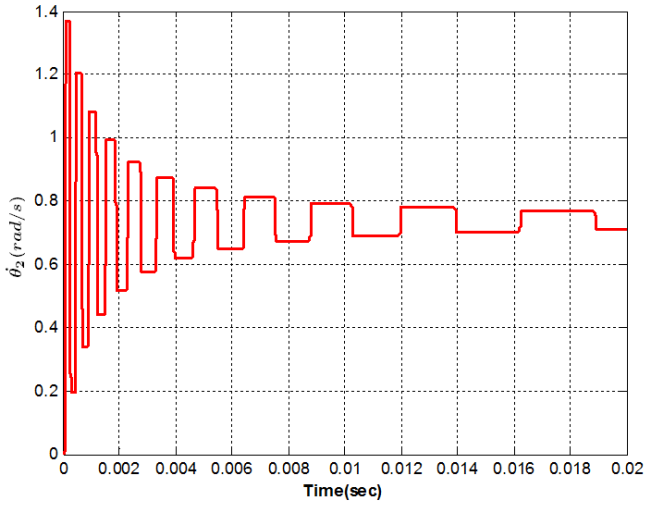

Figure 4-8 Angular velocity of gear 2 for free oscillation - MATLAB – Simulink

In Figure 4-9, the figures on the left are extracted from the developed MSC-Adams model, whereas the figures on the right side are taken from [18]. As can be seen, the results of the MATLAB-Simulink, MSC-Adams and the Reference [18] are very close to each other for the free oscillation case.

The difference between “Yang and Sun” and “Improved Model” taken from [18] is that “Yang and Sun” model considers only The Hertizan deformations whereas the

"Improved Model" uses the trapezoidal beam approximation method as was explained in Chapter 3.

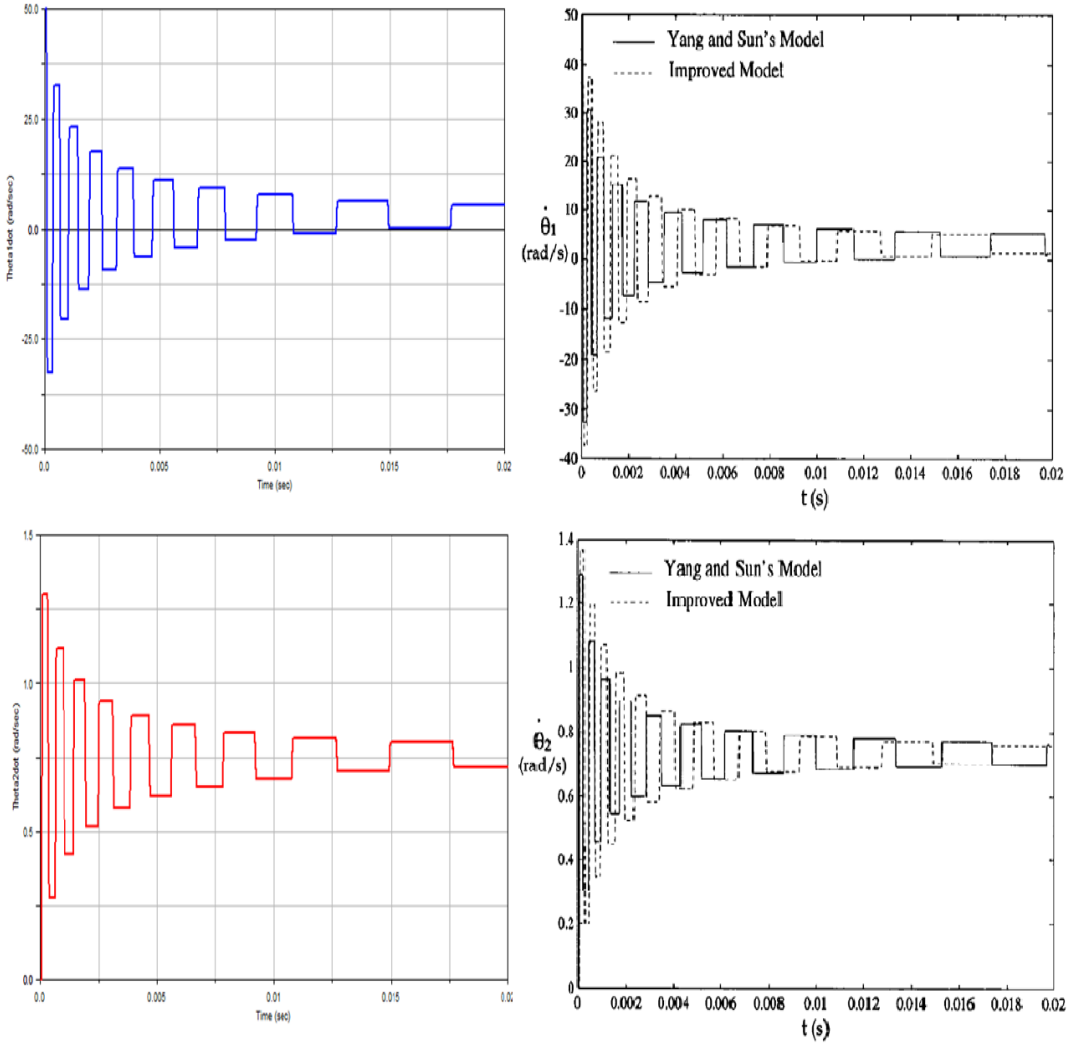

Figure 4-9 Angular velocities: MSC-Adams, Ref. [18]

4.4.2 Constant Load

Under a constant load, the driven gear is expected to have a constant acceleration and therefore a linear velocity if everything is rigid. The deviation from the straight line as can be observed in Figure 4-10, Figure 4-11 and Figure 4-12 is due to the contact deformations and backlash.

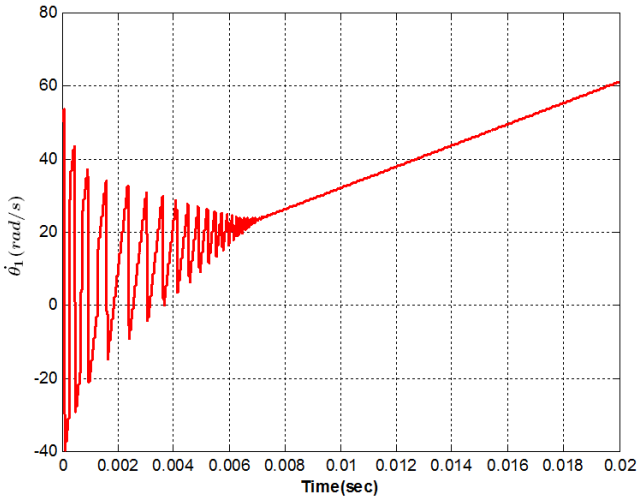

Figure 4-10 Angular velocity of gear 1for constant load - MATLAB - Simulink

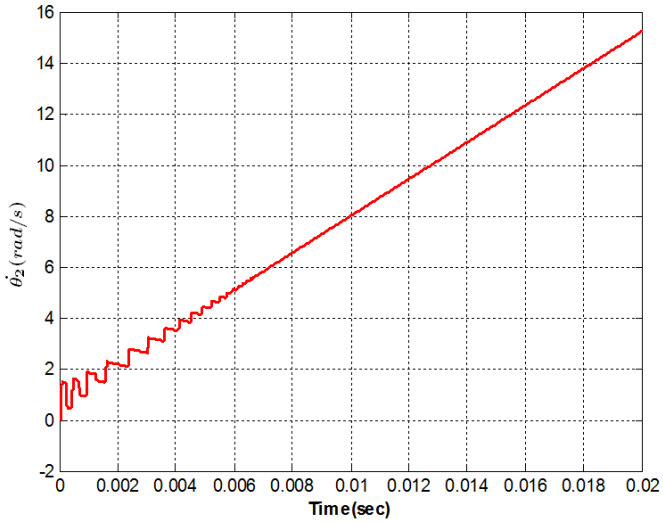

Figure 4-11 Angular velocity of gear 2 for constant load - MATLAB - Simulink

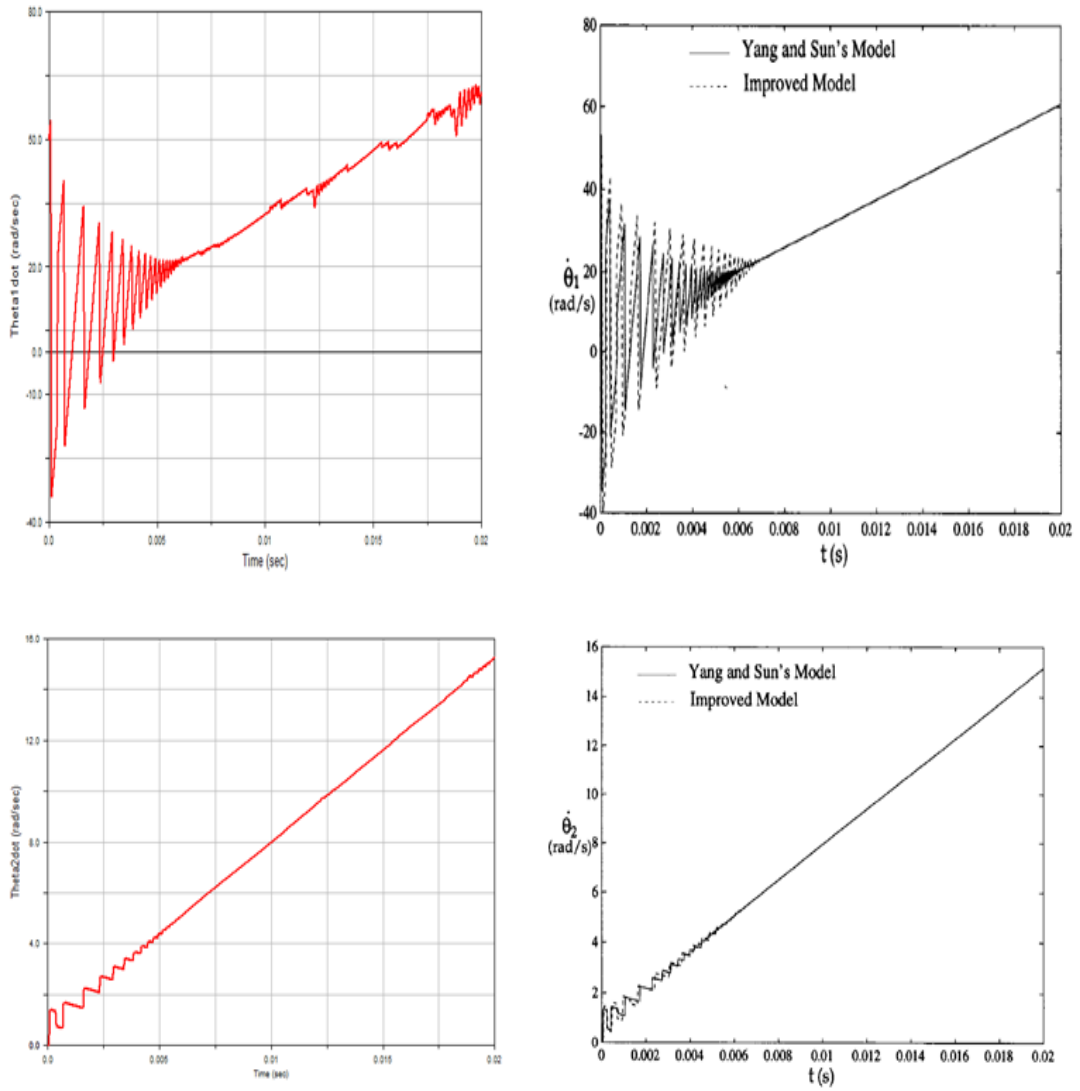

Figure 4-12 Angular velocities: MSC-Adams, Ref. [18]

Similarly, the figures on the left are from the developed MSC-Adams model, whereas the figures on the right side are taken from Reference [18]. Comparing the results, one can conclude that the trends are again very similar however MSC-Adams exhibits slight numerical errors in the driver angular velocity. That is judged to be due to the numerical convergence issue in contact algorithm, however the difference from a straight line is not much. Therefore, it can be concluded that with the correct selected contact parameters and a small enough step size, MSC-Adams is able to capture the transient dynamics quite sufficiently.

4.5 Incorporation of Friction into Model

Up to now, the equations of motions were derived for a gear pair excluding friction. However, there is always friction between mating teeth even if there is lubricant between them. Considering the possibility of front side contact, back side contact, double tooth, single tooth contact regions and forward or backward rotation, there are different modes of operation [18]. Obviously, the equations of motion are different for each mode. Furthermore, when the point of contact reaches the pitch point, the friction force changes its direction. The equations of motion will be written for each mode. For better visualization, free body diagrams of some of the modes are shown in the following figures. Note that the forces acting only on the pinion are shown for the sake of clarity. The forces on the gear are equal in magnitude but opposite in direction.

- If $\dot{\theta}_1$>0 (forward rotation)
  - ➢ Front side contact
    - ✓ Double tooth contact (Figure 4-13)

$$T_1 - r_{b1}P_1 - r_{b1}P_2 + \rho_{11}fP_1 - \rho_{12}fP_2 = I_1\ddot{\theta}_1 \tag{4.23}$$

$$T_2 + r_{b2}P_1 + r_{b2}P_2 - \rho_{21}fP_1 + \rho_{22}fP_2 = I_2\ddot{\theta}_2 \tag{4.24}$$

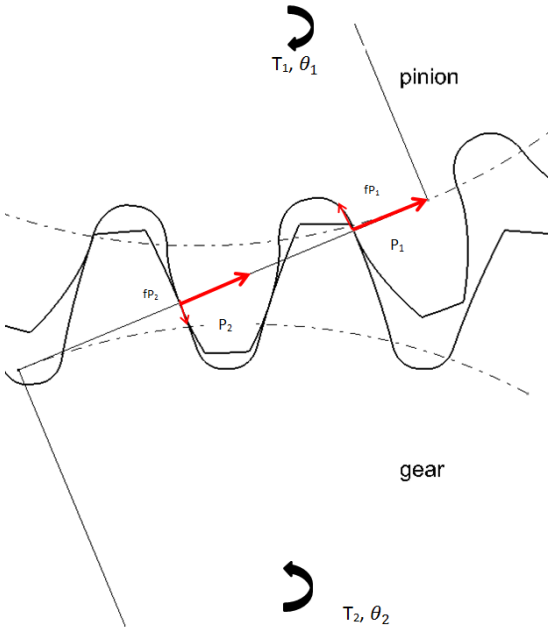

Figure 4-13 Forces acting on the pinion-double tooth zone

✓ Single tooth contact

If the point of contact is in approach region (i.e. before the pitch point-Figure 4-14)

$$T_1 - r_{b1}P_1 + \rho_{11} fP_1 = I_1\ddot{\theta}_1 \quad (4.25)$$

$$T_2 + r_{b2}P_1 - \rho_{21} fP_1 = I_2\ddot{\theta}_2 \quad (4.26)$$

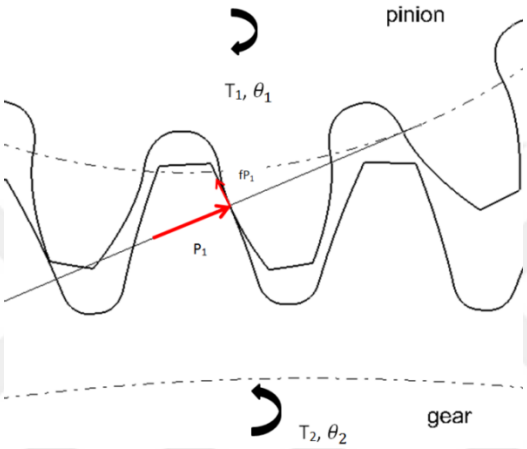

Figure 4-14 Forces acting on the pinion-single tooth zone before the pitch point

If the point of contact is in recess region (i.e. after the pitch point, Figure 4-15)

$$T_1 - r_{b1}P_1 - \rho_{11} fP_1 = I_1\ddot{\theta}_1 \quad (4.27)$$

$$T_2 + r_{b2}P_1 + \rho_{21} fP_1 = I_2\ddot{\theta}_2 \quad (4.28)$$

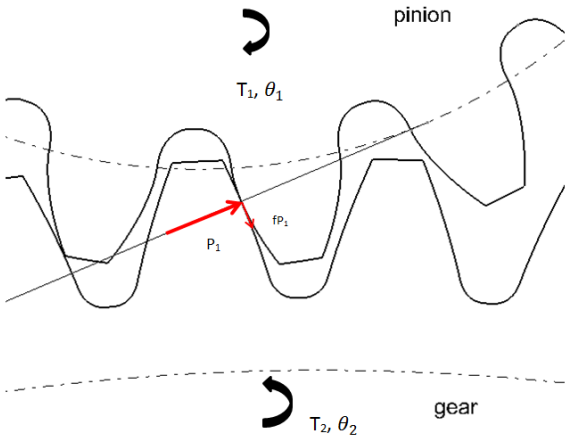

Figure 4-15 Forces acting on the pinion-single tooth zone after the pitch point

- Back side contact
  - ✓ Double tooth contact

$$T_1 + r_{b1}P_1 + r_{b1}P_2 - \rho_{11}fP_1 + \rho_{12}fP_2 = I_1\ddot{\theta}_1 \quad (4.29)$$

$$T_2 - r_{b2}P_1 - r_{b2}P_2 + \rho_{21}fP_1 - \rho_{22}fP_2 = I_2\ddot{\theta}_2 \quad (4.30)$$

  - ✓ Single tooth contact

If the point of contact is in approach region (i.e. before the pitch point)

$$T_1 + r_{b1}P_1 - \rho_{11}fP_2 = I_1\ddot{\theta}_1 \quad (4.31)$$

$$T_2 - r_{b2}P_{12} + \rho_{21}fP_2 = I_2\ddot{\theta}_2 \quad (4.32)$$

If the point of contact is in recess region (i.e. after the pitch point)

$$T_1 + r_{b1}P_1 + \rho_{11}fP_2 = I_1\ddot{\theta}_1 \quad (4.33)$$

$$T_2 - r_{b2}P_1 - \rho_{21}fP_2 = I_2\ddot{\theta}_2 \quad (4.34)$$

- If $\dot{\theta}_1$<0 (backward rotation)
  - Front side contact
    - ✓ Double tooth contact

$$T_1 - r_{b1}P_1 - r_{b1}P_2 - \rho_{11}fP_1 + \rho_{12}fP_2 = I_1\ddot{\theta}_1 \quad (4.35)$$

$$T_2 + r_{b2}P_1 + r_{b2}P_2 + \rho_{22}fP_1 - \rho_{21}fP_2 = I_2\ddot{\theta}_2 \quad (4.36)$$

    - ✓ Single tooth contact

If the point of contact is in approach region (i.e. before the pitch point)

$$T_1 - r_{b1}P_1 - \rho_{11}fP_1 = I_1\ddot{\theta}_1 \quad (4.37)$$

$$T_2 + r_{b1}P_1 + \rho_{21}fP_1 = I_2\ddot{\theta}_2 \quad (4.38)$$

If the point of contact is in recess region (i.e. after the pitch point)

$$T_1 - r_{b1}P_1 - \rho_{11}fP_1 = I_1\ddot{\theta}_1 \quad (4.39)$$

$$T_2 + r_{b1}P_1 + \rho_{21}fP_1 = I_2\ddot{\theta}_2 \tag{4.40}$$

- Back side contact
  - ✓ Double tooth contact

$$T_1 + r_{b1}P_1 + r_{b1}P_2 + \rho_{11}fP_1 - \rho_{12}fP_2 = I_1\ddot{\theta}_1 \tag{4.41}$$

$$T_2 - r_{b2}P_1 - r_{b2}P_2 - \rho_{21}fP_1 + \rho_{22}fP_2 = I_2\ddot{\theta}_2 \tag{4.42}$$

  - ✓ Single tooth contact

If the point of contact is in approach region (i.e. before the pitch point)

$$T_1 + r_{b1}P_1 + \rho_{11}fP_2 = I_1\ddot{\theta}_1 \tag{4.43}$$

$$T_2 - r_{b2}P_1 - \rho_{21}fP_2 = I_2\ddot{\theta}_2 \tag{4.44}$$

If the point of contact is in recess region (i.e. after the pitch point)

$$T_1 + r_{b1}P_1 - \rho_{11}fP_2 = I_1\ddot{\theta}_1 \tag{4.45}$$

$$T_2 - r_{b2}P_1 + \rho_{21}fP_2 = I_2\ddot{\theta}_2 \tag{4.46}$$

4.6 Equations of Motions for Inverse Dynamics

These set of equations are used when the driver angular velocity is assumed to be constant regardless of the output gear. There is a constant resistance torque at the output gear. Consequently, pinion torque and driven gear angular velocity are variable. The solutions are realized for the steady state response, therefore initial angular velocity of the output gear is computed as driver angular velocity multiplied by the gear ratio. This method has been the more conventional method for investigating variation of dynamic loads and the effect of friction on gears in the absence of backlash. It is also used commonly in frequency domain analysis for determining dynamic factor with respect to pinion angular velocity.

By referring to Figure 4-16, and using the notation given in [16],

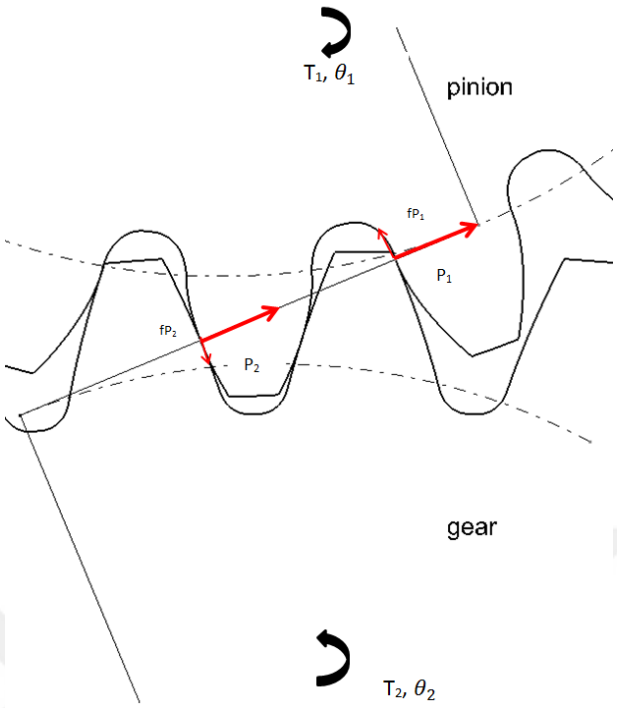

Figure 4-16 Free body diagram of gears

$$T_1 - r_{b1}(P_1 + P_2) + \rho_{11} f_1 P_1 - \rho_{12} f_2 P_2 = I_1 \ddot{\theta}_1 \tag{4.47}$$

$$T_2 + r_{b2}(P_1 + P_2) - \rho_{21} f_1 P_1 + \rho_{22} f_2 P_2 = I_2 \ddot{\theta}_2 \tag{4.48}$$

Since the angular velocity of the driver gear is constant, the right hand side of Eq. (4.47) becomes zero.

$$T_1 - r_{b1}(P_1 + P_2) + \rho_{11} f_1 P_1 - \rho_{12} f_2 P_2 = 0 \tag{4.49}$$

In the above equations P_1 and P_2 are the individual gear loads in the double tooth contact zone.

$$P_1 = k_1(r_{b1}\theta_1 - r_{b2}\theta_2) \tag{4.50}$$

$$P_2 = k_2(r_{b1}\theta_1 - r_{b2}\theta_2) \tag{4.51}$$

Note that if the point of contact is in single tooth contact zone P_2 becomes zero. The single tooth contact zone also includes the pitch point transition. Pitch point is the point at which the relative sliding velocities of gear teeth become zero. The friction force changes its direction while passing through the pitch point.

If the point of contact is in approach region and in single tooth zone,

$$T_1 - r_{b1}P_1 + \rho_{11} f_1 P_1 = 0 \tag{4.52}$$

$$T_2 + r_{b2}P_1 - \rho_{21} f_1 P_1 = I_2 \ddot{\theta}_2 \tag{4.53}$$

If the point of contact is in recess region and in single tooth zone,

$$T_1 - r_{b1}P_1 - \rho_{11} f_1 P_1 = 0 \tag{4.54}$$

$$T_2 + r_{b2}P_1 + \rho_{21} f_1 P_1 = I_2 \ddot{\theta}_2 \tag{4.55}$$

At this point, the usual practice is to introduce a new variable called transmission error [16] as;

$$x_r = (r_{b1}\theta_1 - r_{b2}\theta_2) \tag{4.56}$$

This transformation enables reduction of the coupled differential equations of motions into a single second order differential equation in terms of transmission error. However, in the developed model, this transformation has not been performed and the solution is obtained in a fully coupled form.

Due to the existence of lubrication between the gear teeth, the coefficient of friction is not constant and it is dependent on the relative velocities of gears. There are many gear friction models in the literature. One of models that has been widely accepted is the Benedict- Kelley friction model as given in AGMA 925-A03 [31].

According to this formulation, the instantaneous sliding and entraining velocities of the gear pairs should be known during the dynamic analysis. For the sake of coherence, the notation will be as explained until now although a slightly different notation has been used in AGMA 925-A03.

Rolling velocities;

$$V_{rp1} = \dot{\theta}_p \rho_{p1} \tag{4.57}$$

$$V_{rG1} = \dot{\theta}_G \rho_{G1} \tag{4.58}$$

Sliding velocity;

$$V_{s1} = \left| V_{rp1} - V_{rG1} \right| \tag{4.59}$$

Entraining velocity;

$$V_{e1} = \left| V_{rp1} + V_{rG1} \right| \tag{4.60}$$

The above equations are valid for the first gear pair in the mesh. For the second mesh;

$$\rho_{p2} = \rho_{p1} + p_b \tag{4.61}$$

$$\rho_{G2} = \rho_{G1} - p_b \tag{4.62}$$

Rolling velocities are;

$$V_{rp2} = \dot{\theta}_p \rho_{p2} \tag{4.63}$$

$$V_{rG2} = \dot{\theta}_G \rho_{G2} \tag{4.64}$$

Consequently the sliding velocities and the entraining velocities can be computed as;

$$V_{s2} = \left| V_{rp2} - V_{rG2} \right| \tag{4.65}$$

$$V_{e2} = \left| V_{rp2} + V_{rG2} \right| \tag{4.66}$$

Knowing the instantaneous sliding and entraining velocities; coefficient of friction of the *ith* pair as predicted by Benedict-Kelley [31] becomes;

$$\mu_{mi} = 0.0127 C_{Ravgx} \log_{10}\left(\frac{29700 X_{\Gamma i} w_n}{\eta_M V_{si} V_{ei}^2} \right) \tag{4.67}$$

where

η_M is dynamic viscosity of the oil at gear tooth temperature, θ_m. (mPa*s)

$X_{\Gamma i}$ is the load sharing factor for the *ith* pair.

w_n is the normal load per unit length, (N/mm)

C_{Ravgx} is the surface roughness constant which can be computed from,

$$1 \le C_{Ravgx} = \frac{1.13}{1.13 - R_{avgx}} \le 3 \tag{4.68}$$

where R_{avgx} is the average surface roughness of the pinion and gear surfaces. This value is usually available in handbooks of machinery for different types of manufacturing methods. Note that in the simulations, $C_{Ravgx}, \eta_M, X_{\Gamma i}$ are constants whereas w_n, V_{si}, V_{ei} should be calculated at each time step of the simulation.

4.7 Simulation Results for Inverse Dynamics

Dynamic load variation on a single tooth pair for a complete mesh cycle is plotted for different angular speeds of the driver gear in Figure 4-17 and Figure 4-19. The gear parameters used in the simulation are given in Table 3

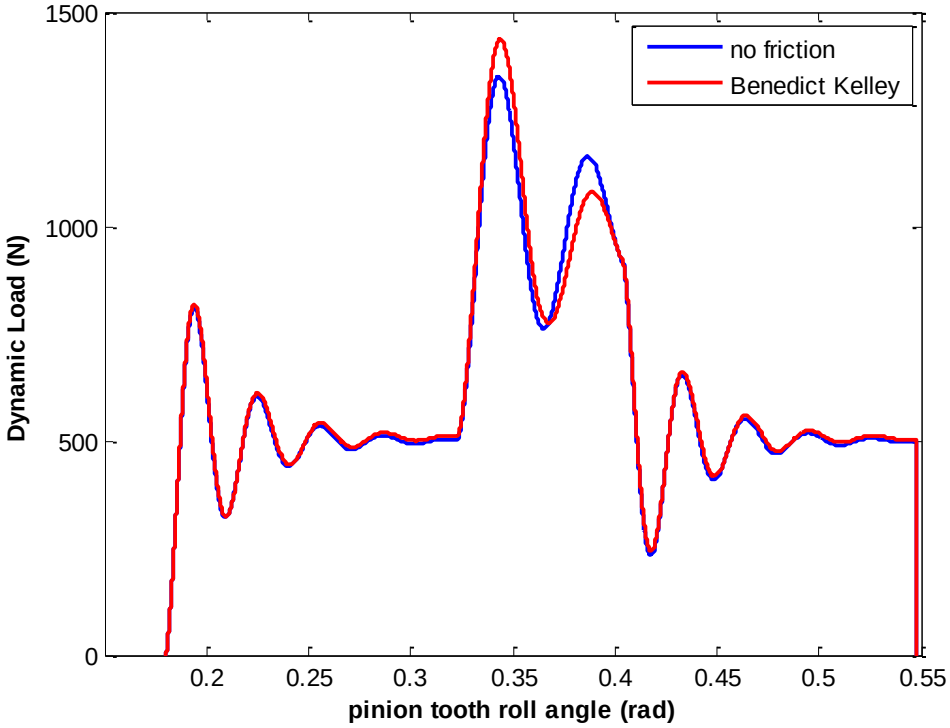

Figure 4-17 Variation of dynamic load on pinion tooth for 2000 rpm pinion speed

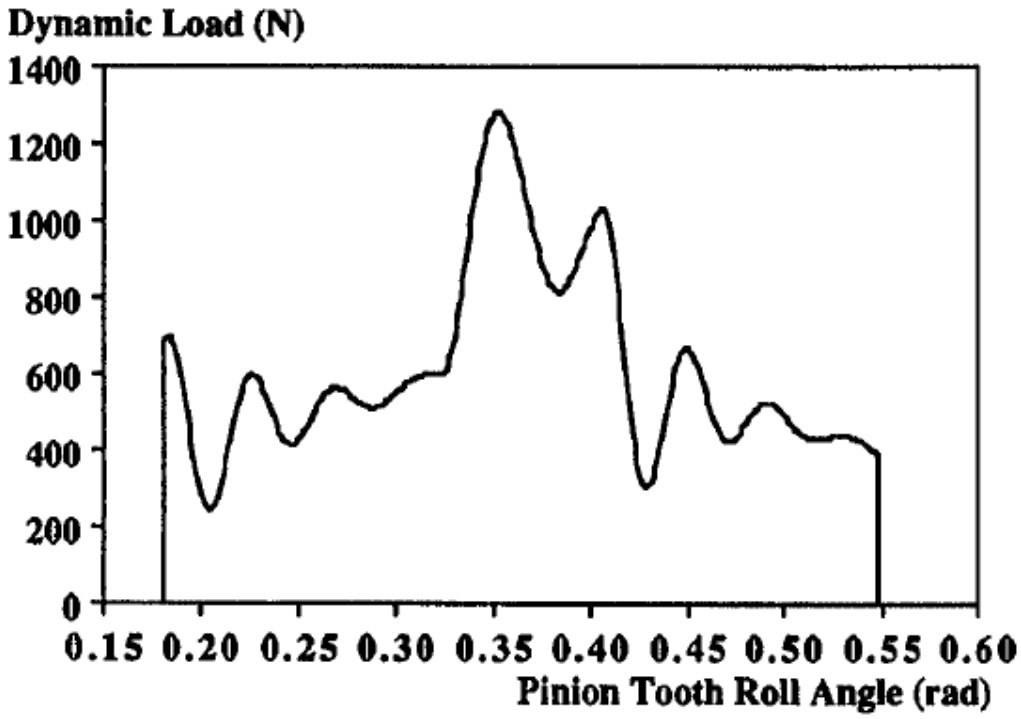

Figure 4-18 Variation of dynamic load on pinion tooth for 2000 rpm pinion speed, Ref. [16]

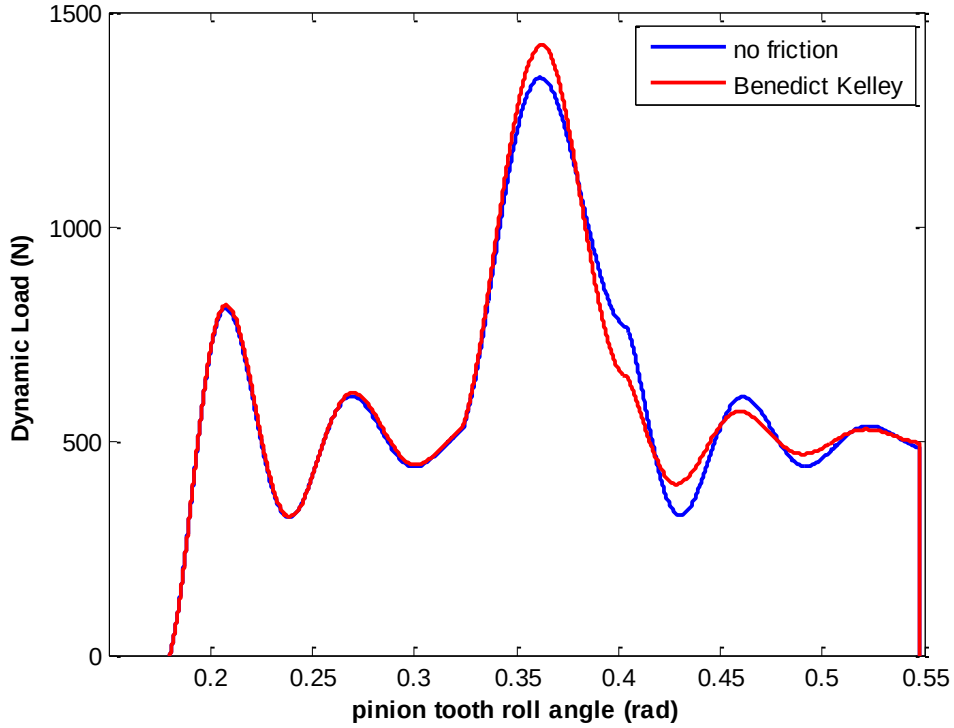

Figure 4-19 Variation of dynamic load on pinion tooth for 4000 rpm pinion speed

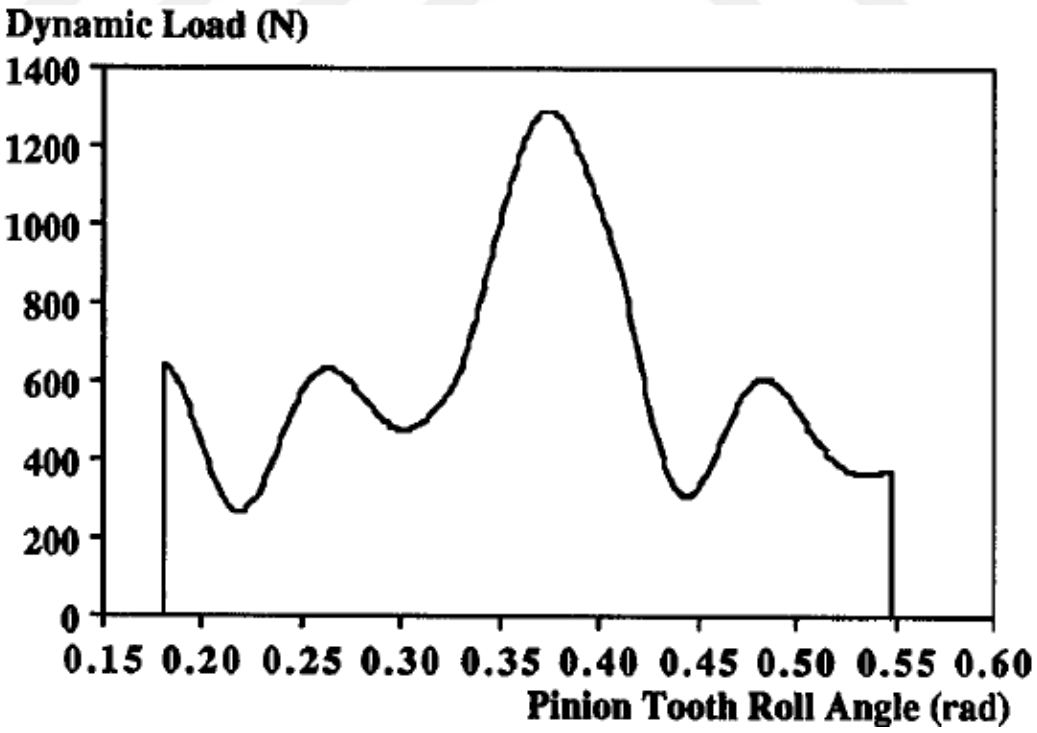

Figure 4-20 Variation of dynamic load on pinion tooth for 4000 rpm pinion speed, Ref. [16]

The similarity of the plots verify the developed model in the MATLAB Simulink environment. Based on this model, the required motor torques in order to realize the given motion are also plotted.

Table 3 Simulated gear parameters for inverse dynamics

Module	3.175 mm
Pressure angle	20°
Face width	6.35 mm
Pinion number of teeth	28
Gear ratio	1
Pinion inertia	5.234E-4 kgm^2
Gear inertia	5.234E-4 kgm^2

The required motor torque in order to provide the given motion is plotted in Figure 4-21 and Figure 4-22 for 2000 rpm and 4000 rpm pinion angular velocities respectively.

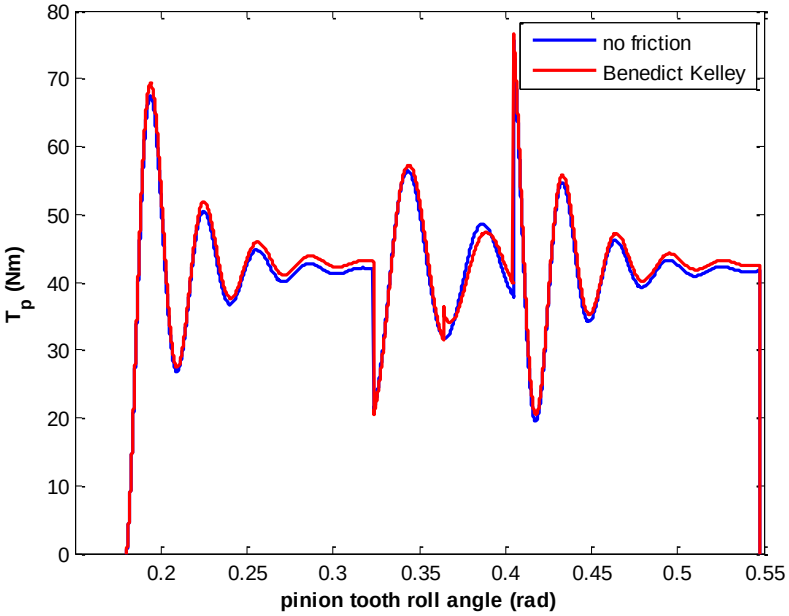

Figure 4-21 Required motor torque for 2000 rpm

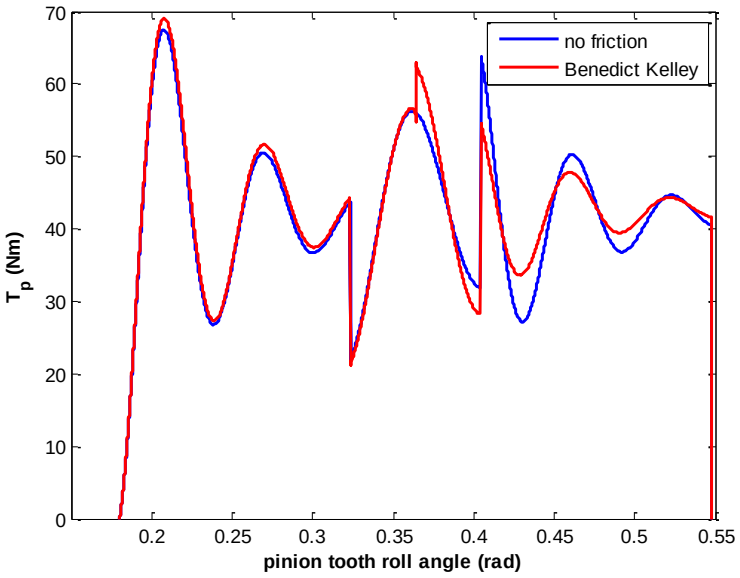

Figure 4-22 Required motor torque for 4000 rpm

The jumps in the motor torques are due to the sudden sign change of the friction force at the pitch point.

A screenshot of the developed Simulink model for inverse dynamics is available in Appendix C, Figure C2.

The variation of coefficient of friction for different angular speeds is also investigated for the given gear pair. The load sharing ratio $x_{\Gamma i}$ is taken as unity. R_{avgx} is taken as 0.40 micron for ground gear teeth, and finally dynamic viscosity η_m is taken as 100 mPas.

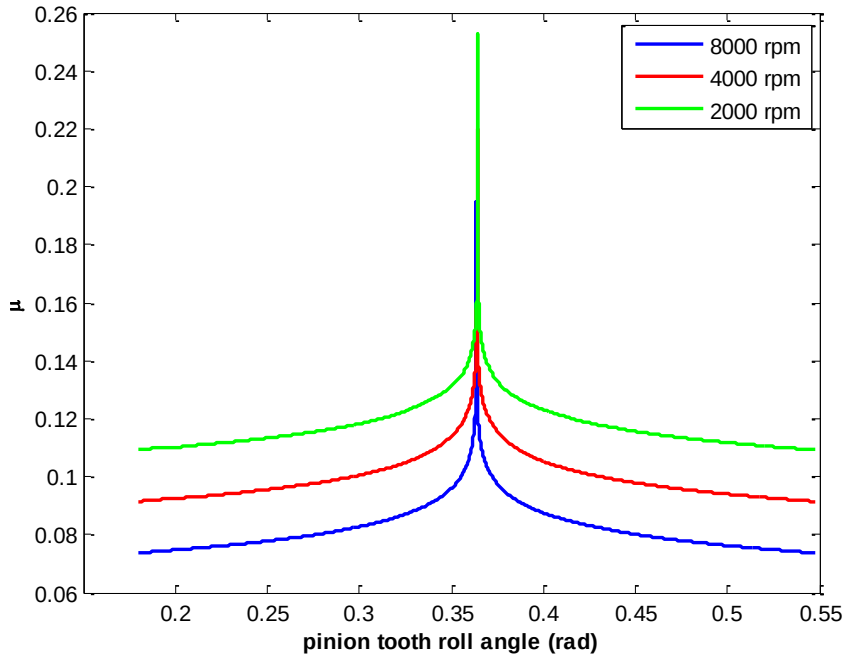

Figure 4-23 Friction coefficient for different driver angular velocities- for inverse dynamics

As can be seen in Figure 4-23, the friction coefficient decreases as the angular velocity of the driver gear increases.

CHAPTER 5

DYNAMIC MODELLING OF THE GUN TURRET ELEVATION AXIS

In this chapter, the theory of gear dynamics which has been developed in chapters 2 and 3 is applied to the elevation axis of a one man turret with target tracking capability. In order to observe the effect of backlash on the target tracking performance, several simulations are conducted for different backlash values in MATLAB Simulink.

Then the system is linearized which assumes front side contact, average mesh stiffness and no backlash. A PID controller has been designed for the linear system and then the performance of the controller is investigated for the real non-linear time varying system.

After tuning the PID parameters of the controller in MATLAB, these parameters are applied to the dynamic model in MSC Adams using Adams Controls toolkit.

The compliant and hinged anti-backlash mechanism is then incorporated into MSC-Adams. The turret dynamic model is improved by inserting the torsional elevation driveline stiffness into the structure.

The errors in target tracking and energy consumption in the motor are investigated for different anti-backlash characteristics such as spring preload and stiffness values using the complex and realistic dynamic model in MSC-Adams.

5.1 Incorporation of Gear Dynamics to the Model

The basic elements of the elevation axis of gun turret were introduced in chapter 2. In that chapter the gear train was treated as rigid therefore it was assumed to be acting as a simple speed reduction element. However, because of the reasons

explained in chapters 3 and 4, the gears also acts as springs and dampers within themselves. This brings another degree of freedom to the system as depicted in Figure 5-1.

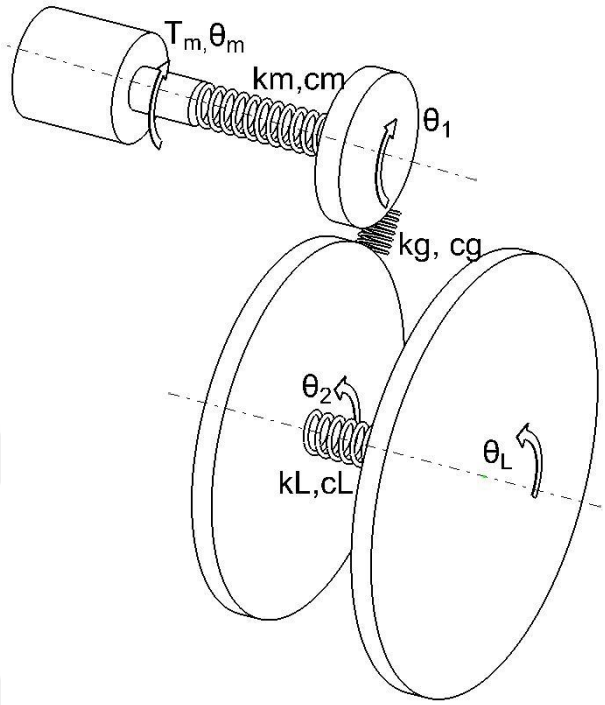

Figure 5-1 Schematic of the improved dynamic model

In the above figure, k_g and c_g represent the gear mesh stiffness and gear mesh damping coefficients. With the utilization of gear dynamics theory developed in chapter 4, assuming no backlash for the gears, the equations of motions can be written as;

$$I_m\ddot{\theta}_m + c_m\left(\dot{\theta}_m - \dot{\theta}_1\right) + k_m\left(\theta_m - \theta_1\right) = T_m \tag{5.1}$$

$$\begin{aligned} I_1\ddot{\theta}_1 + c_m\left(\dot{\theta}_1 - \dot{\theta}_m\right) + k_m\left(\theta_1 - \theta_m\right) + c_g r_{b1}\left(r_{b1}\dot{\theta}_1 - r_{b2}\dot{\theta}_m\right) \\ + k_g r_{b1}\left(r_{b1}\theta_1 - r_{b2}\theta_2\right) = 0 \end{aligned} \tag{5.2}$$

$$\begin{aligned} I_2\ddot{\theta}_2 + c_L\left(\dot{\theta}_2 - \dot{\theta}_L\right) + k_L\left(\theta_2 - \theta_L\right) + c_g r_{b2}\left(r_{b2}\dot{\theta}_2 - r_{b1}\dot{\theta}_1\right) \\ + k_g r_{b2}\left(r_{b2}\theta_2 - r_{b1}\theta_1\right) = 0 \end{aligned} \tag{5.3}$$

$$I_L\ddot{\theta}_L + c_L\left(\dot{\theta}_L - \dot{\theta}_2\right) + k_L\left(\theta_L - \theta_2\right) = 0 \tag{5.4}$$

When the equations are written in matrix form;

$$\begin{bmatrix} I_m & 0 & 0 & 0 \\ 0 & I_1 & 0 & 0 \\ 0 & 0 & I_2 & 0 \\ 0 & 0 & 0 & I_L \end{bmatrix} \begin{bmatrix} \ddot{\theta}_m \\ \ddot{\theta}_1 \\ \ddot{\theta}_2 \\ \ddot{\theta}_L \end{bmatrix} + \begin{bmatrix} c_m & -c_m & 0 & 0 \\ -c_m & c_m + c_g r_{b1}^2 & -c_g r_{b1} r_{b2} & 0 \\ 0 & -c_g r_{b1} r_{b2} & c_m + c_g r_{b2}^2 & -c_L \\ 0 & 0 & -c_L & c_L \end{bmatrix} \begin{bmatrix} \dot{\theta}_m \\ \dot{\theta}_1 \\ \dot{\theta}_2 \\ \dot{\theta}_L \end{bmatrix}$$
$$+ \begin{bmatrix} k_m & -k_m & 0 & 0 \\ -k_m & k_m + k_g r_{b1}^2 & -k_g r_{b1} r_{b2} & 0 \\ 0 & -k_g r_{b1} r_{b2} & k_L + k_g r_{b2}^2 & -k_L \\ 0 & 0 & -k_L & k_L \end{bmatrix} \begin{bmatrix} \theta_m \\ \theta_1 \\ \theta_2 \\ \theta_L \end{bmatrix} = \begin{bmatrix} 1 \\ 0 \\ 0 \\ 0 \end{bmatrix} T_m \tag{5.5}$$

Once the mass, stiffness and damping matrices are available, the system can be described fully by conversion to state space equations as was done in chapter 2.

$$A = \begin{bmatrix} [0]_{4x4} & [I]_{4x4} \\ -[M]^{-1}[K] & -[M]^{-1}[C] \end{bmatrix} \tag{5.6}$$

$$B = \begin{bmatrix} [0]_{4x1} \\ -[M]^{-1}[I_d] \end{bmatrix} \tag{5.7}$$

Where the state vector is;

$$x = \begin{bmatrix} \theta_m & \theta_1 & \theta_2 & \theta_L & \dot{\theta}_m & \dot{\theta}_1 & \dot{\theta}_2 & \dot{\theta}_L \end{bmatrix}^T \tag{5.8}$$

If the load side angular velocity is selected as the output;

$$C = \begin{bmatrix} 0 & 0 & 0 & 0 & 0 & 0 & 0 & 1 \end{bmatrix} \tag{5.9}$$

$$D = 0 \tag{5.10}$$

5.2 The Improved Dynamic Model in Simulink

The level of complexity of the developed dynamic models have been gradually increased throughout the thesis. Despite the dynamic model which is developed in section 5.1 includes the gear mesh stiffness and damping of the gear train; the model inherently includes two assumptions; namely no backlash and viscous damping in gears. However, backlash might be present if it is not mechanically eliminated. Furthermore, during high frequency oscillating movements, it may degrade the dynamic performance significantly

The Simulink gear dynamics model developed in Section 4.2 included backlash and realistic friction models. In order to complete the dynamic modeling, the driveline compliances in the gun turret are integrated to that Simulink model. The improved

and final model includes the driveline compliances, realistic gear friction and possible backlash. The screenshot of the developed final model can be seen in Appendix C, Figure C3.

5.3 Construction of the Dynamic Model in MSC-Adams

Construction of the turret dynamic model in MSC-Adams is relatively easy. The revolute joints and fixed joints should be assigned at the appropriate positions. Then the inertia of the rotating elements should be input. Care must be taken while specifying the inertia of the rotating elements because the inertia around the rotation axis might be different than the inertia with respect to center of mass. Hence the inertia should be input with respect to the rotation axis of the elements. All of the elevating parts' inertia is lumped to rotor body and the rotation axis of the rotor is specified as the inertia reference point.

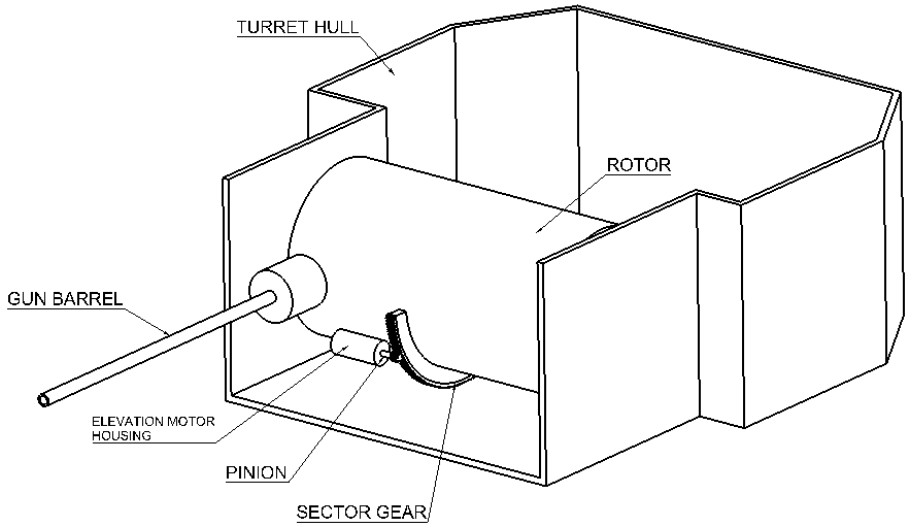

Figure 5-2 Isometric view of the turret (turret hull top and front not shown for clarity)

Table 4 System parameters

N_p	14
N_G	408
Module	1.5 mm
I_{motor}	3E-4 kgm^2
I_{pinion}	3E-4 kgm^2
I_{sector}	0.3 kgm^2
I_{load}	49.7 kgm^2
Ideal center distance of the gear pair	316.5 mm
Coordinates of the pinion center (mm)	0,0,0
Coordinates of the rotor center (mm)	278.80, 149.81,0

The individual representative bodies of the turret have been created in CATIA V5 and then imported into MSC-Adams environment in parasolid (x.t) format. Isometric and side view of the developed turret model can be seen in Figure 5-3 and Figure 5-4 respectively.

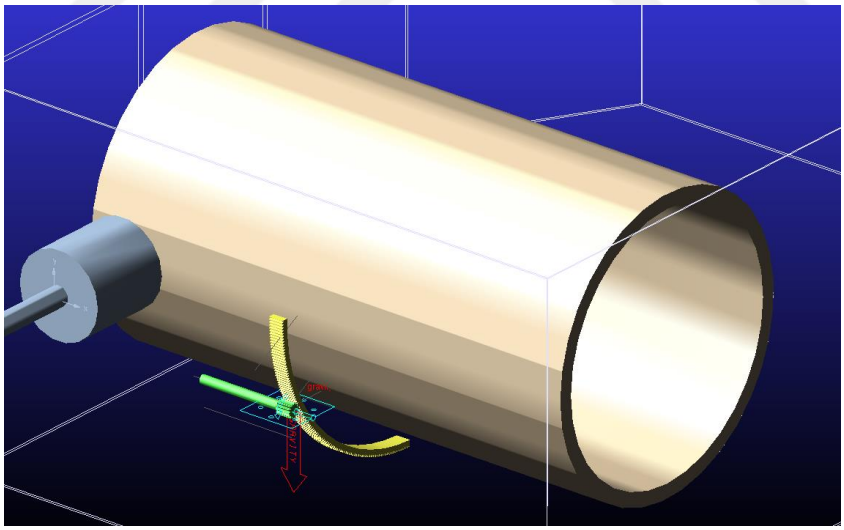

Figure 5-3 Isometric view of the turret in MSC Adams

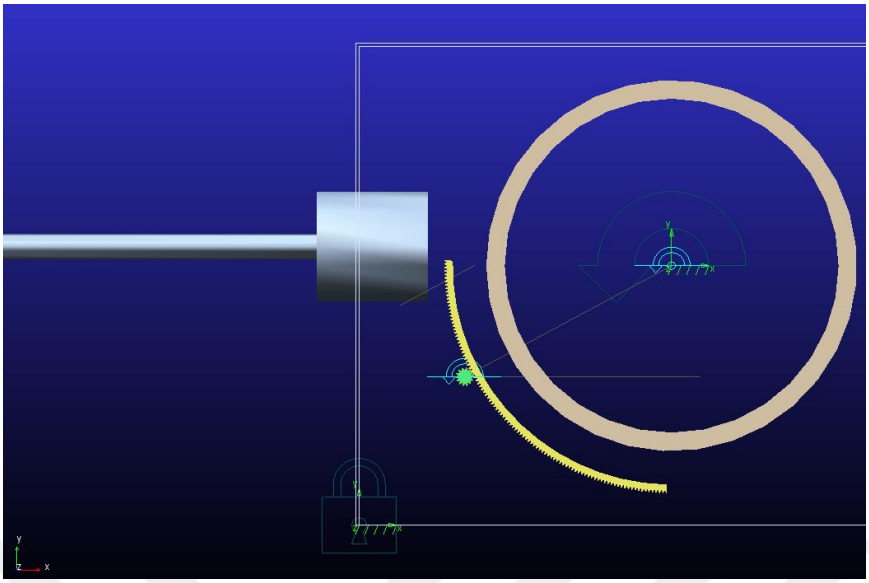

Figure 5-4 Side view of the elevation axis

5.4 Contact friction in MSC-Adams

Coulomb friction is a discontinuous function due to its nature. During a dynamical simulation, discontinuities, hence sudden changes in the system parameters, may cause the solutions to diverge. In order to prevent this, MSC-Adams uses a friction model [30] that is continuous and dependent on the slip velocities of the contacting surfaces.

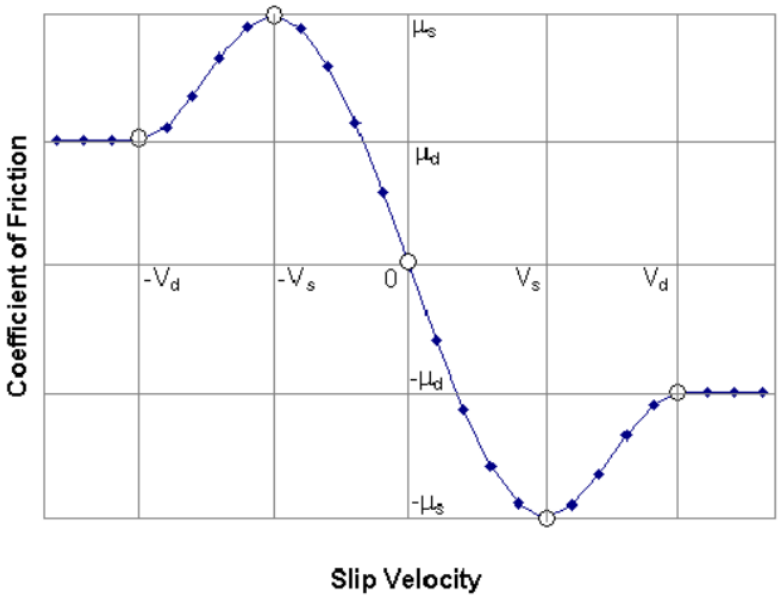

Figure 5-5 Friction model in MSC Adams [30]

In the above figure; μ_s and μ_d represent static and dynamic friction coefficients respectively. The transition from the static friction to dynamic friction coefficients are determined via the stiction transition velocity V_s and the dynamic transition velocity V_d. By choosing μ_s to μ_d; and V_s to V_d close to each other; the friction model converges to the regular Coulomb friction. For comparison purposes with MATLAB-Simulink model, this method has been applied so that the friction is almost Coulomb friction at the expense of computation time. In other words, solution step size needs to be decreased in order to prevent divergence that stems from the Coulomb discontinuity.

5.5 Integration of the anti-backlash mechanism

Spring preloaded, hinged anti-backlash mechanism is ready to be incorporated into the dynamic model as depicted in Figure 5-6 and Figure 5-7. As explained in chapter 1, the anti-backlash mechanism pushes the pinion gear into the sector gear by pivoting around the pivot axis. The motor chassis is fixed to the turret hull whereas the pivot bracket is able to pivot around the revolute joint.

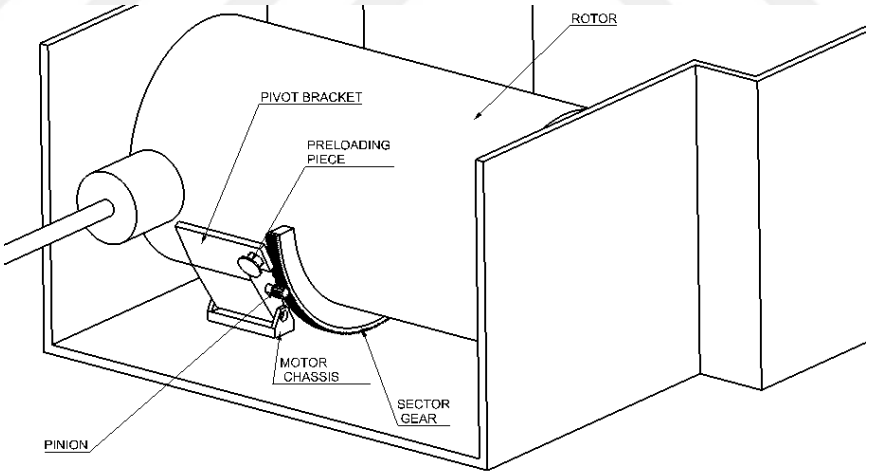

Figure 5-6 Isometric view of the integrated anti-backlash mechanism

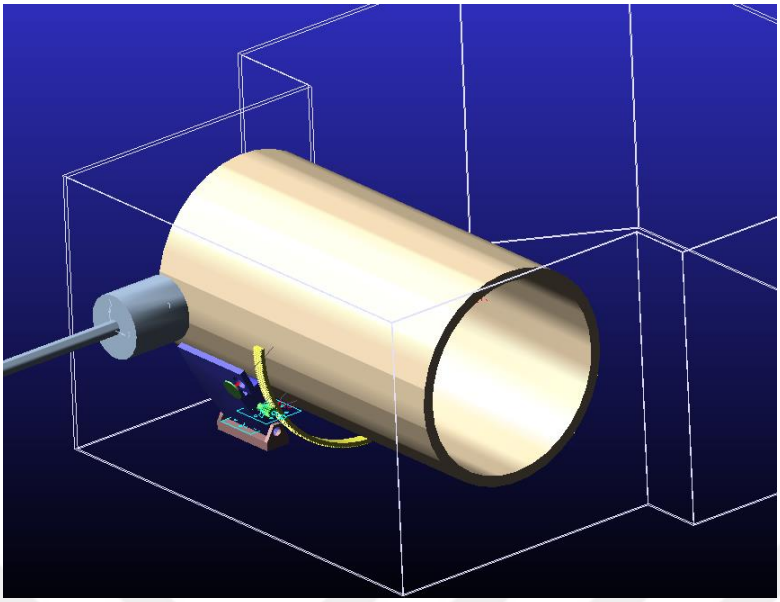

Figure 5-7 Isometric view of the integrated anti-backlash mechanism in MSC-Adams

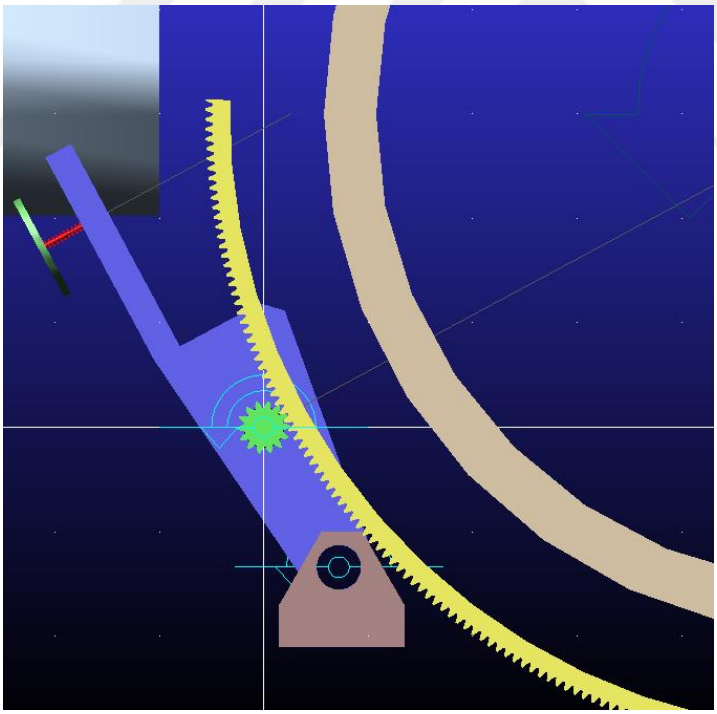

Figure 5-8 Side view of the anti-backlash mechanism

The preloaded springs constantly pushes the pivot bracket and the pinion shaft into the sector gear as shown in Figure 5-8.

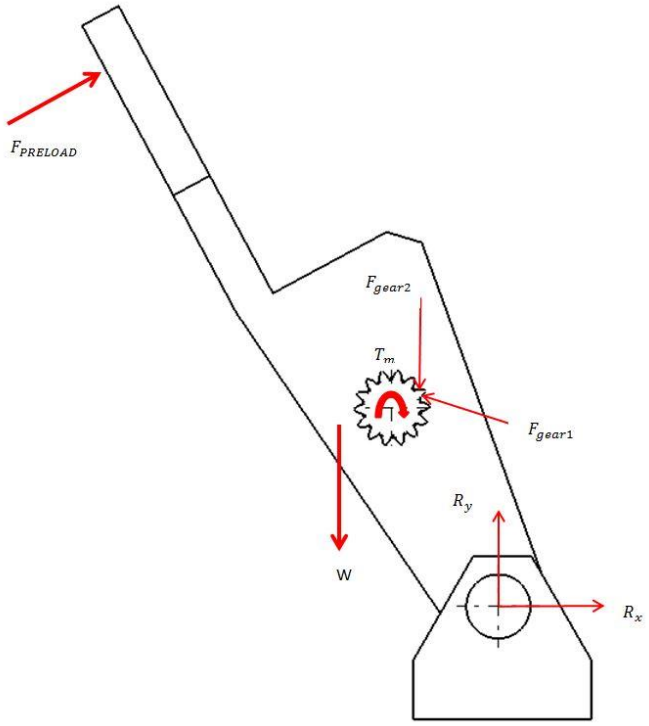

Figure 5-9 Free-body diagram of the anti-backlash mechanism

5.6 Target Tracking in MATLAB - Simulink

In order to track a given angular velocity command, the angular velocity of the load side is fed back into the system. This information is usually available from a gyroscope in a gun turret and the torque is regulated by means of a negative feedback controller. The sensor dynamics are neglected hence the system is a unity feedback system. The controller design was performed via MATLAB SISO toolbox.

The four degree of freedom state space model developed in section 5.1 is used for control purposes. The open loop transfer function $\dot{\theta}_L(s)/T_m(s)$ is determined with the command ss2tf in MATLAB.

For a 1 rad/s reference input; the requirements for the controller are,

- No overshoot is allowed
- Settling time to be less than 1.2 sec

By moving one of the closed loop poles along the imaginary axis, the desired performance specifications are achieved via simple P controller.

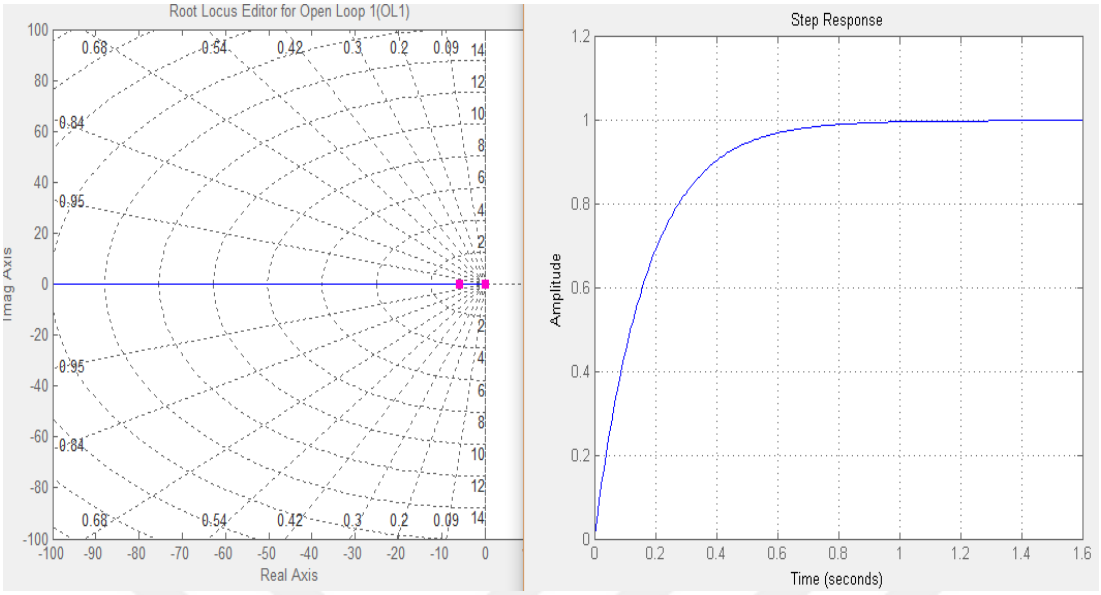

Figure 5-10 SISO tool screenshot

The designed P controller is also applied to the developed Simulink model.

5.7 Target Tracking in MSC-Adams

The MSC-Adams model which was constructed in section 5.3 is improved so that the MATLAB Simulink model and the MSC-Adams model can be compared. For this purpose, the control toolkit of MSC-Adams has been used. Instantaneous angular velocity of the rotor is fed back into the controller. The measured angular velocity is subtracted by the desired angular velocity which gives the tracking error. This error is then amplified by P controller which becomes the motor torque. This torque is the torque applied on the motor shaft.

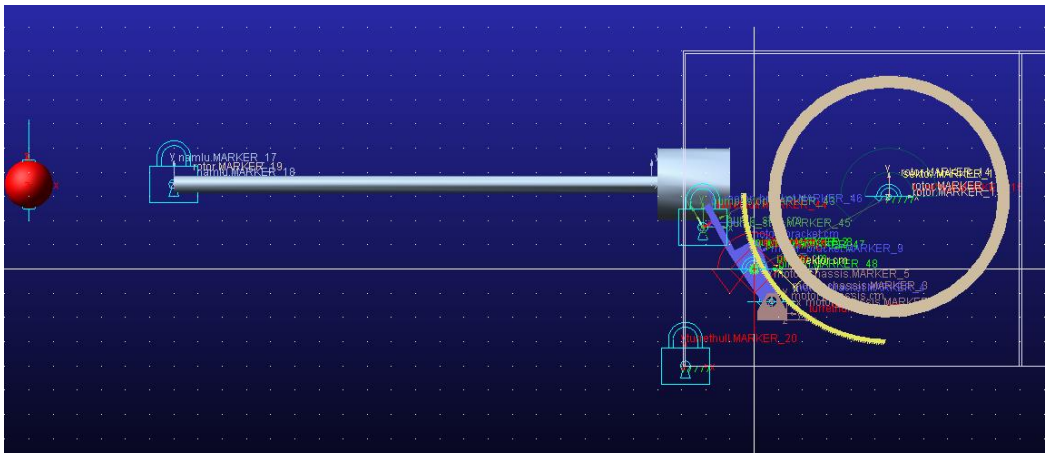

Figure 5-11 Target tracking in MSC-Adams

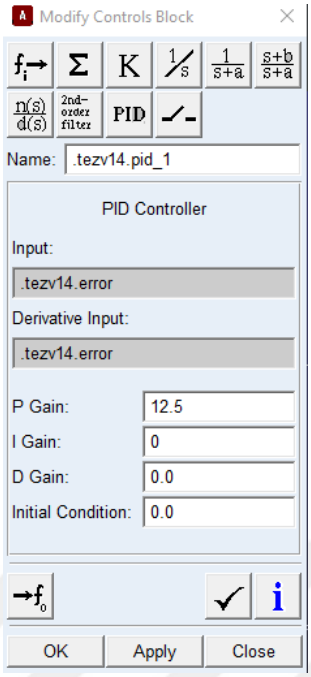

Figure 5-12 Controls toolkit interface in MSC-Adams

5.8 Simulation Results

5.8.1 Open Loop Frequency Domain Results in MATLAB-Simulink

The state space models for 2 d.o.f. The frequency response of the dynamic models with different degrees of freedoms are plotted for comparison purposes. The two and three d.o.f. systems explained in chapter 2 are compared with the four degree of freedom model that was developed in section 5.1. For the transfer function, $\frac{\dot{\vartheta}_L(s)}{T_m(s)}$, as shown in Figure 5-13 , the 4 d.o.f. model depicts an extra resonance. Similarly, for the transfer function, $\frac{\dot{\vartheta}_m(s)}{T_m(s)}$, there is one extra anti-resonance and resonance as shown in Figure 5-14.

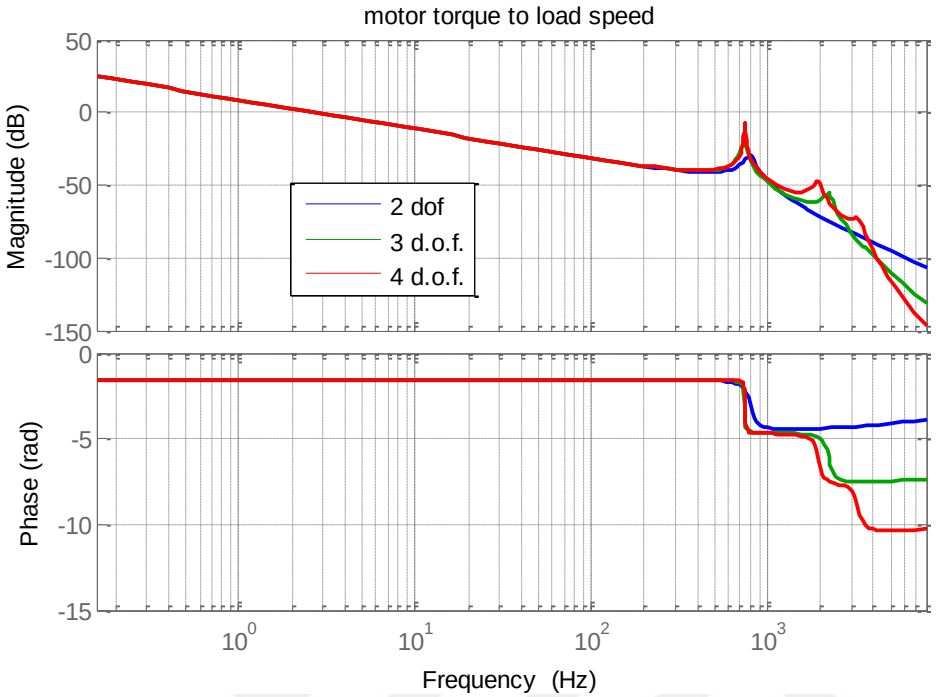

Figure 5-13 Bode plot of motor torque to load speed

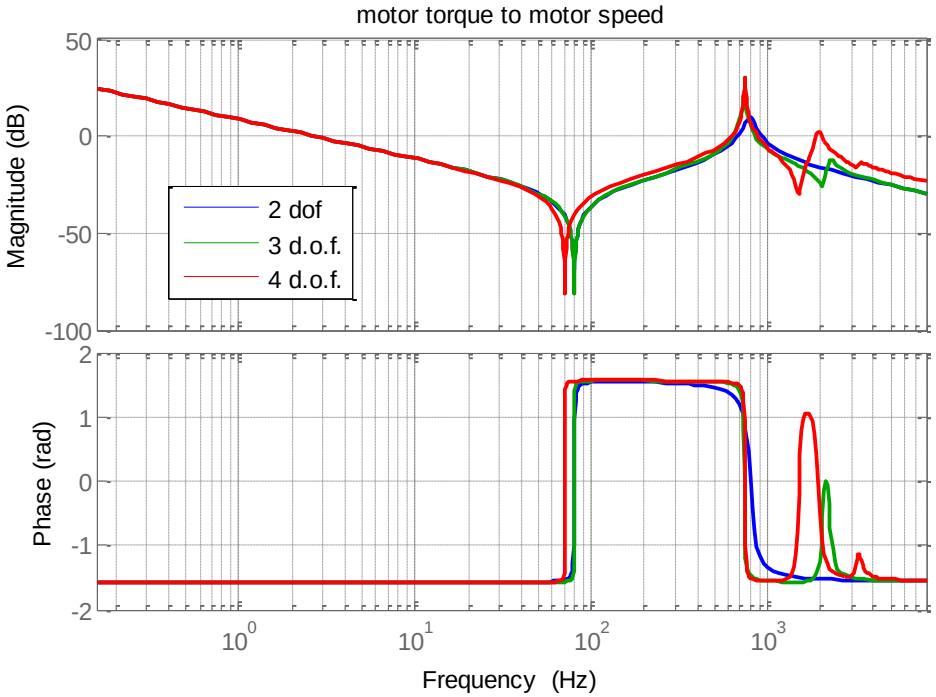

Figure 5-14 Bode plot of motor torque to motor speed

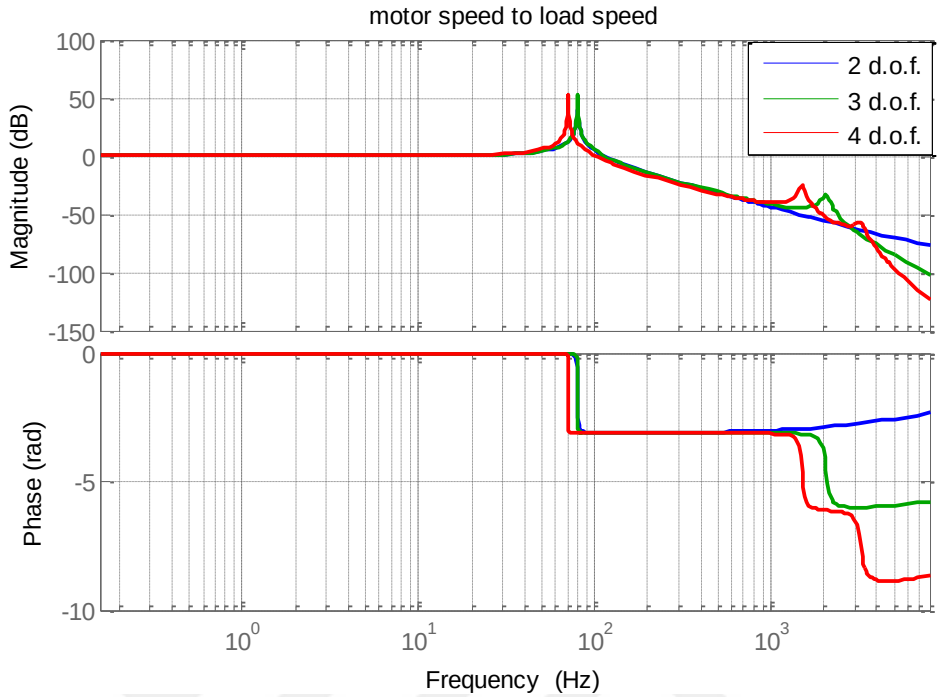

Figure 5-15 Bode plot of motor speed to load speed

The transfer function $\frac{\dot{\theta}_L(s)}{\dot{\theta}_m(s)}$ is also commonly used for determining the system's open loop characteristics. Figure 5-15 shows that when the mesh stiffness of the gear pair is included, the frequency at which the magnitude peak occurs is shifted towards left which means that the open loop system is more susceptible to resonance behavior when it is excited sinusoidally. Obviously, this amount of shift is dependent on stiffness and inertia matrices of the system and it can be significant for higher inertia and less stiff gun turrets.

5.8.2 Open Loop Time Domain Results in MATLAB-Simulink

With the developed models throughout the thesis, various types of simulations are performed.

5.8.2.1 Effect of Gear Friction

By using the methods developed in sections 4.5 and 4.6, the Simulink model can be used to compare the open loop responses of the gun turret for various friction models. Under a constant motor torque of 10 Nm, three different friction modes are investigated. The first mode assumes that Coulomb friction is zero in the gear mesh.

The second model is the classical Coulomb friction model as explained in section 4.5. Finally the last model is the more realistic Benedict-Kelley friction model as explained in section 4.6.

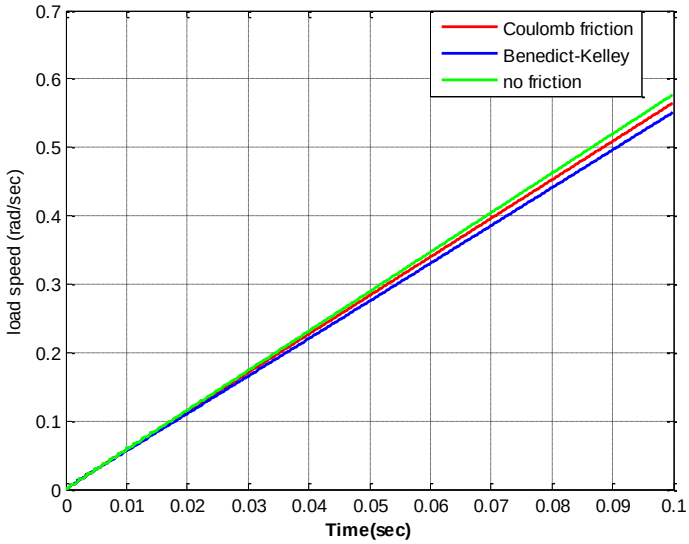

Figure 5-16 Comparison of different friction models on load speed vs. time

5.8.2.2 Effect of Drive-line Stiffness

Since the motor shaft stiffness is determined and usually fixed by the company that manufactures the electrical drives, the designer does not have a performance improvement capability on that parameter. However, the designer of a gun turret can influence the stiffness of the load side. Although it may seem desirable to keep the load side as rigid as possible, practical limitations on weight, volume and cost usually give the designers a very narrow margin on gun turrets. Therefore, the goal for the mechanical designer is usually to reach the sufficient stiffness without hindering controllability, but still to comply with the limitations mentioned above.

For a constant torque of 10 Nm, the system is simulated for different load side torsional stiffness (k_L) values in order to see the effect of load side stiffness on the open loop response of the system. In the below figure, k_1, k_2 and k_3 values stand for $2.5x10^7 Nm/rad$, $2.5x10^6 Nm/rad$, $2.5x10^5 Nm/rad$ respectively.

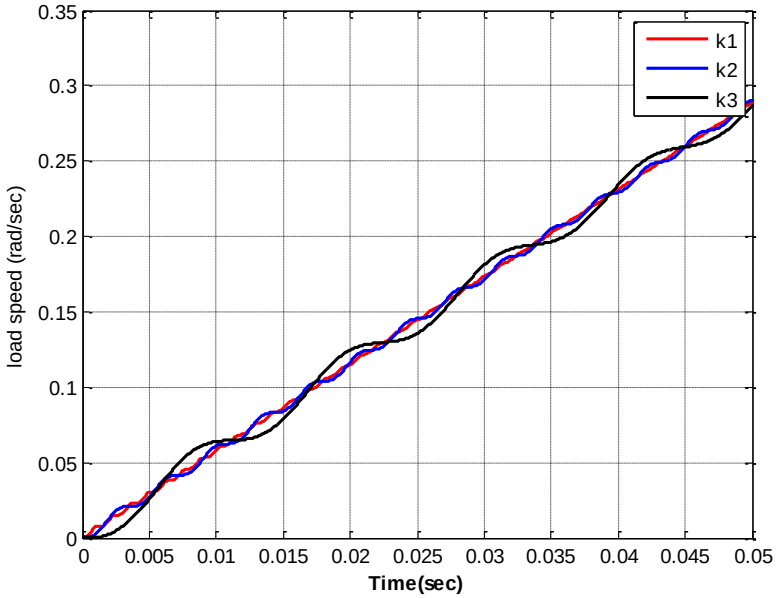

Figure 5-17 Comparison of different load side stiffness values

($k_1 = 2.5x10^7, k_2 = 2.5x10^6, k_3 = 2.5x10^5$ Nm/rad)

A softer driveline obviously causes the load side to have higher amplitude and lower frequency oscillations. It should be noted that if everything was rigid, one would expect a straight line for the load side angular velocity under a constant torque.

5.8.3 Closed Loop Results in MATLAB-Simulink

The simulation results for closed loop system are presented in this section. The purpose of the controller is to track a reference input speed. Different performance evaluations can be made in order to see the effect of different parameters on the overall system performance. One performance parameter is the tracking error which can be defines as the difference between the actual speed and the desired speed. This error is amplified by the P controller and becomes the torque applied by the motor.

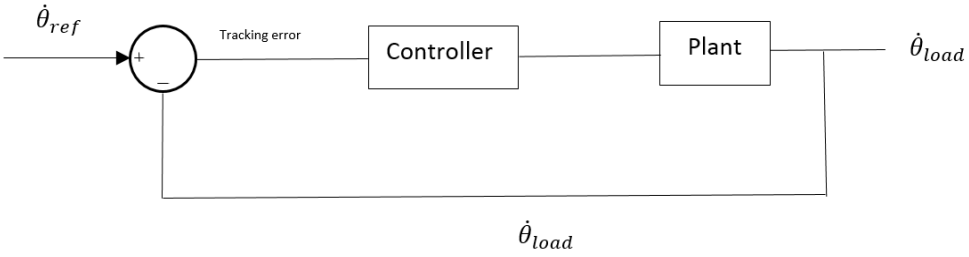

Figure 5-18 Block diagram of the system

5.8.3.1 Effect of Backlash on the Control System Performance

The possible effects of backlash on gear dynamics were investigated in chapter 4 in a detailed manner. Possibility of front side contact, separation and back side contact causes the system to be piece-wise continuous and therefore non-linear. The effect of backlash, on the performance of the gun turret under a simple proportional controller is investigated. A possible backlash value of 0.02 mm in the gear pairs is simulated and compared with the no backlash case. The reference input is 1 rad/s.

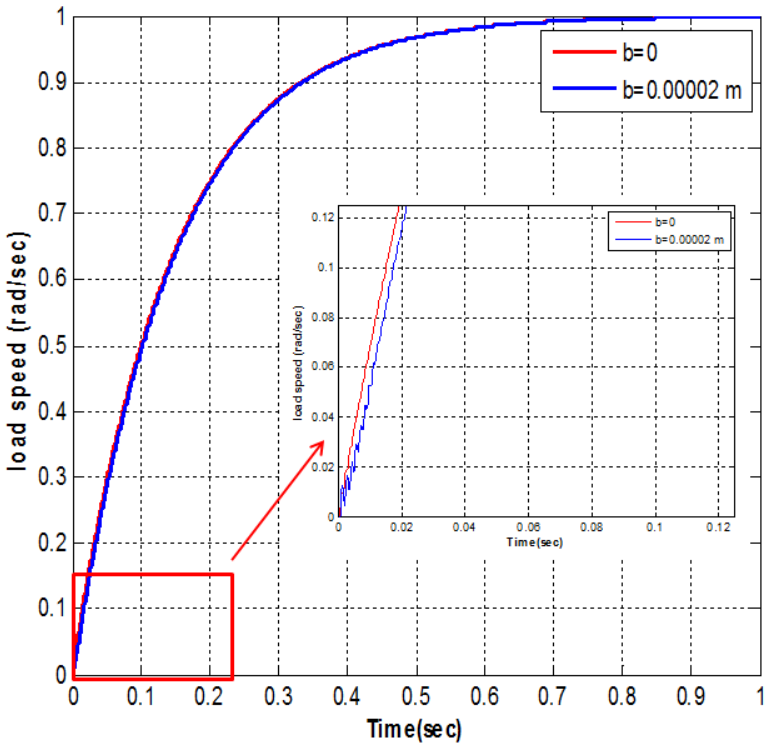

Figure 5-19 Load speed vs. time for zero and 0.02 mm backlash

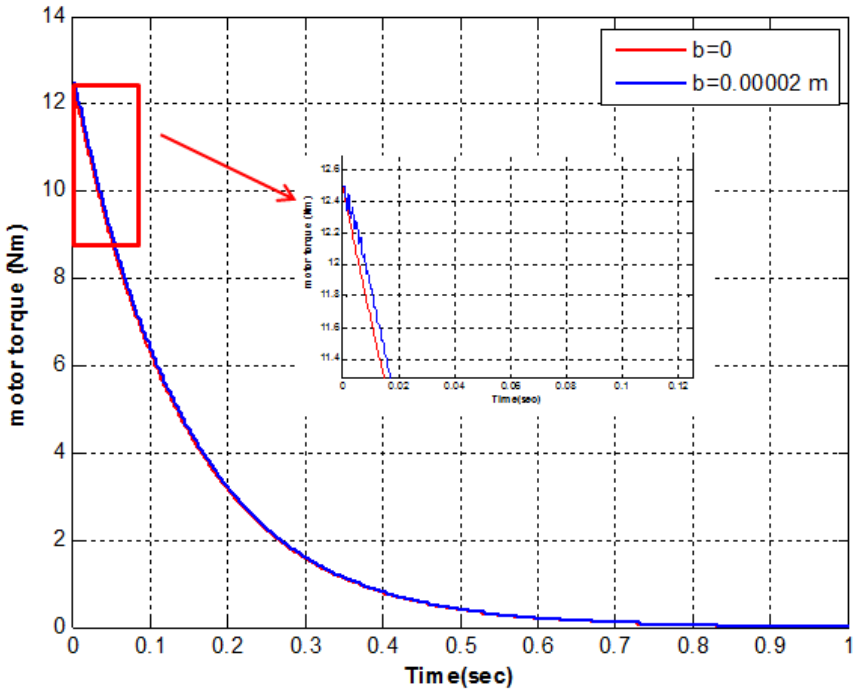

Figure 5-20 Motor torque vs. time for zero and 0.02 mm backlash

As can be easily seen from Figure 5-20; the existence of backlash yields undesirable transients at the load side for short time intervals. After the initial transients die out, the system tracks the given input accordingly. In order to compensate the transients, motor torque tries to provide the torque accordingly causing the non-smooth behavior.

When backlash is increased, the system can't track the given input reference speed and hence becomes unstable. For a backlash value of 0.1 mm, the instability of the load speed can be observed in Figure 5-21.

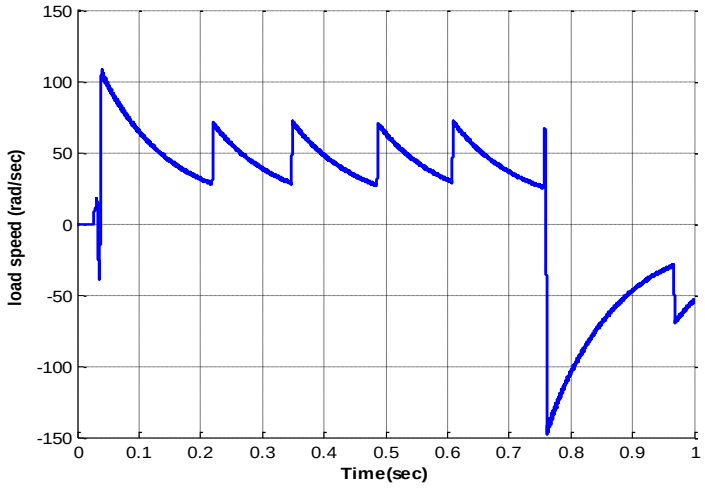

Figure 5-21 Load speed vs. time (b=0.0001 m)

Obviously, the instability mentioned above is due to the simple controller design, which can be solved by more advanced control algorithms. However, the fact remains same: Backlash causes transient errors and if not compensated, may cause a system to be unstable.

5.8.3.2 Effect of Gear Friction on the Control System Performance

In order to investigate the effect of friction models on the closed loop system performance, two main performance attributes are studied. The first attribute is naturally the response of the load side speed under the same control parameters. The second performance characteristic that is studied is the instantaneous power consumption of the motor. Power consumption is computed as;

$$P = \left| T_m \dot{\theta}_m \right| \tag{5.11}$$

When the system is operating in a closed loop, the controller compensates the differences that arise due to the physical nature of the friction models. As can be seen in the figures below; the response differences between the two friction models is small.

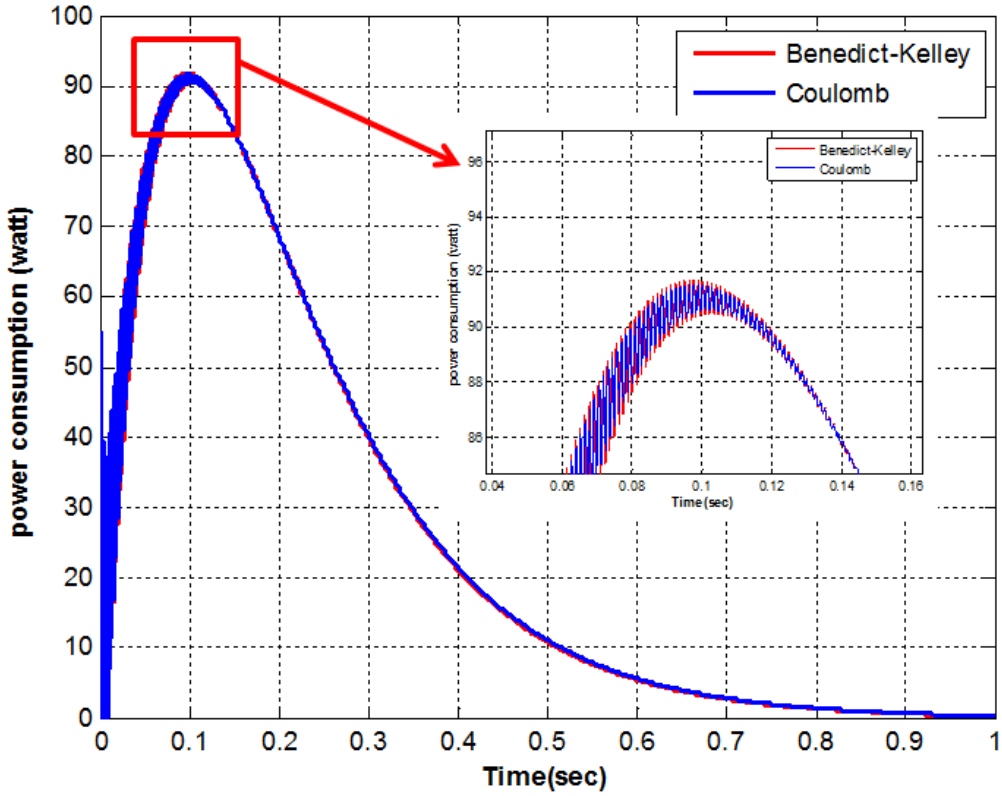

Figure 5-22 Power consumption vs. time

5.8.4 MSC-Adams Verifications

Throughout the thesis, the dynamic modeling in the MATLAB and Simulink environment was in conjunction with the MSC-Adams models. The level of complexities of dynamic systems have increased in a parallel manner in both programs. In this sense the MSC Adams serves as a verification tool to the rigorously developed complex models in MATLAB. Once the verified MSC-Adams model is available, the user can continue to add any kind of additional complexity to the multi-body dynamics environment.

A quick comparison of MSC Adams figures with the relevant MATLAB figures yields that the results are in agreement with each other for both open loop and closed loop systems.

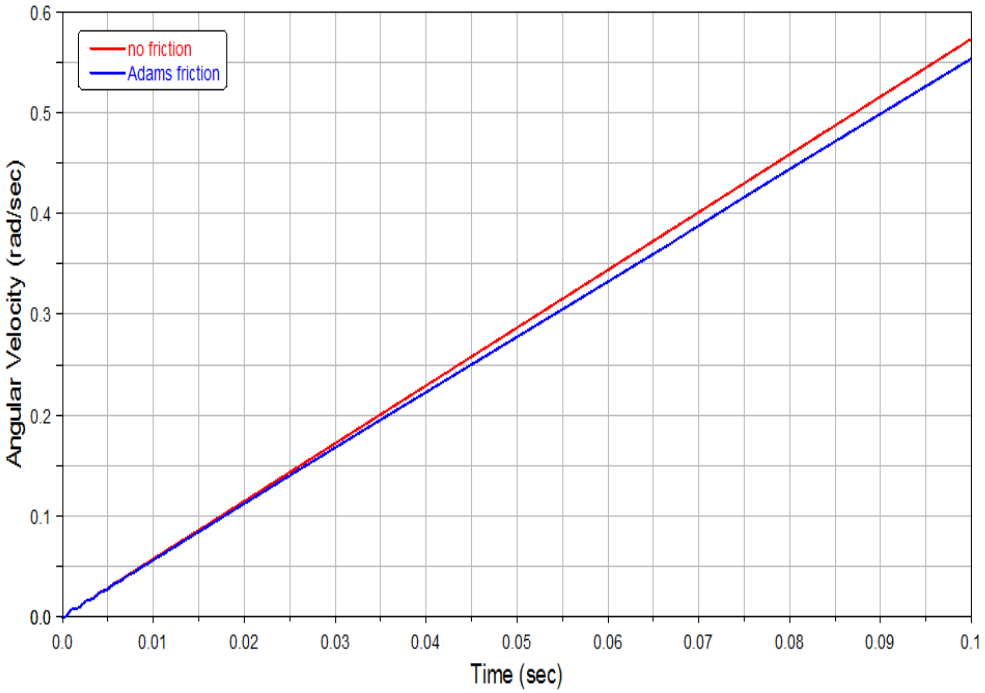

Figure 5-23 MSC-Adams for no friction and Adams contact friction

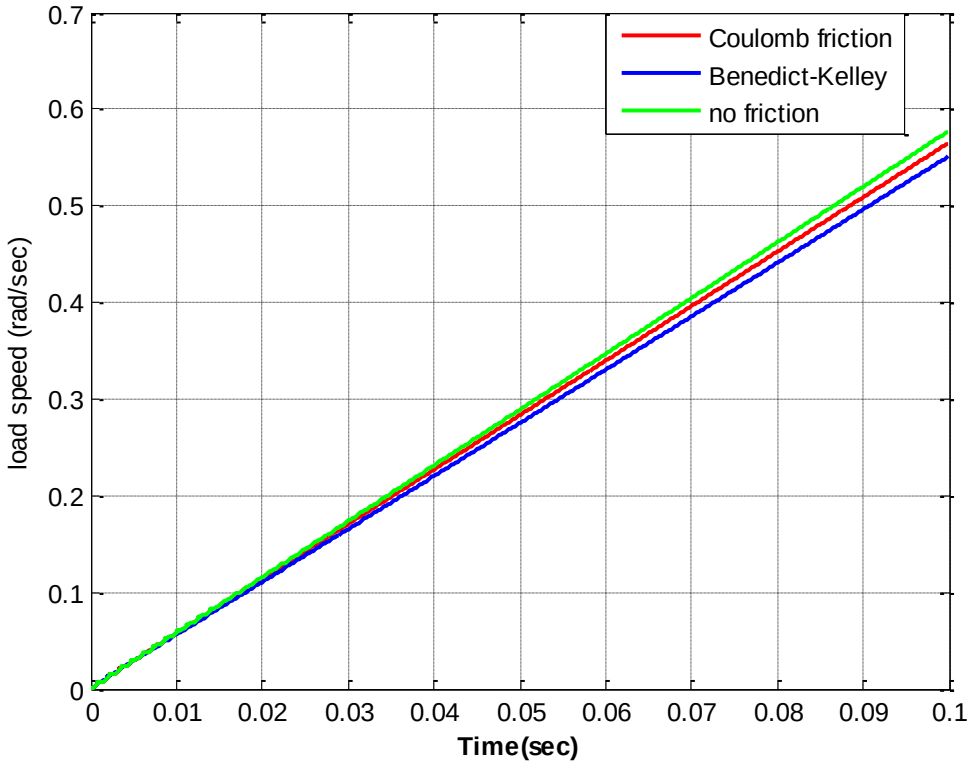

Figure 5-24 Comparison of different friction models in Matlab

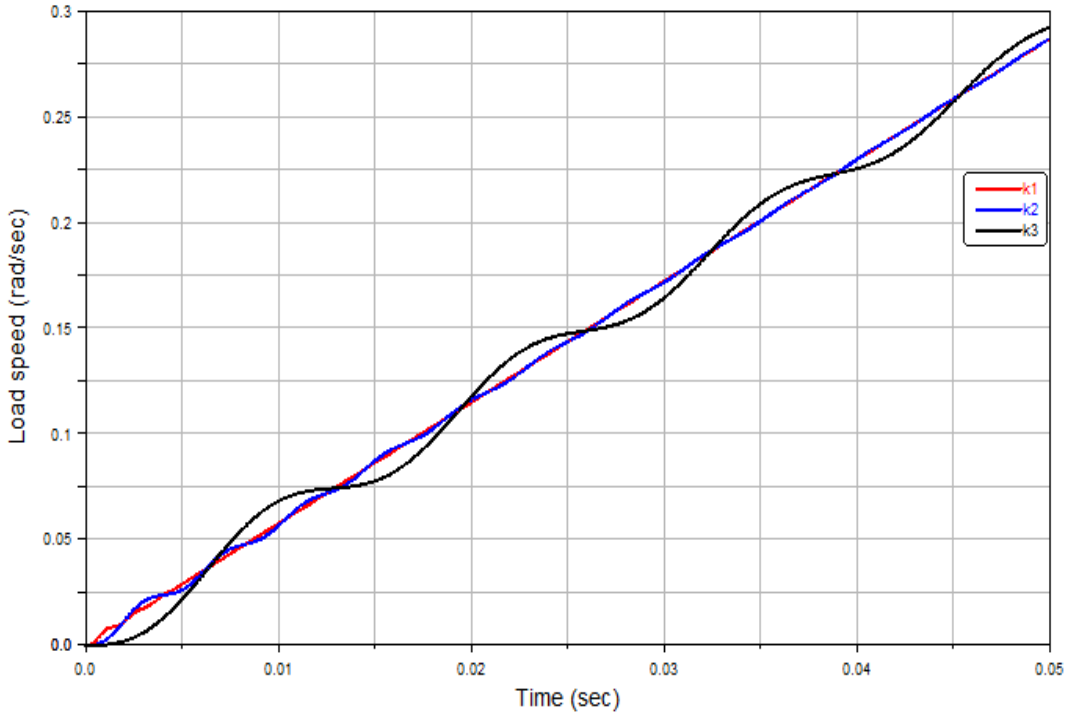

Figure 5-25 MSC-Adams plot for different load side stiffness values

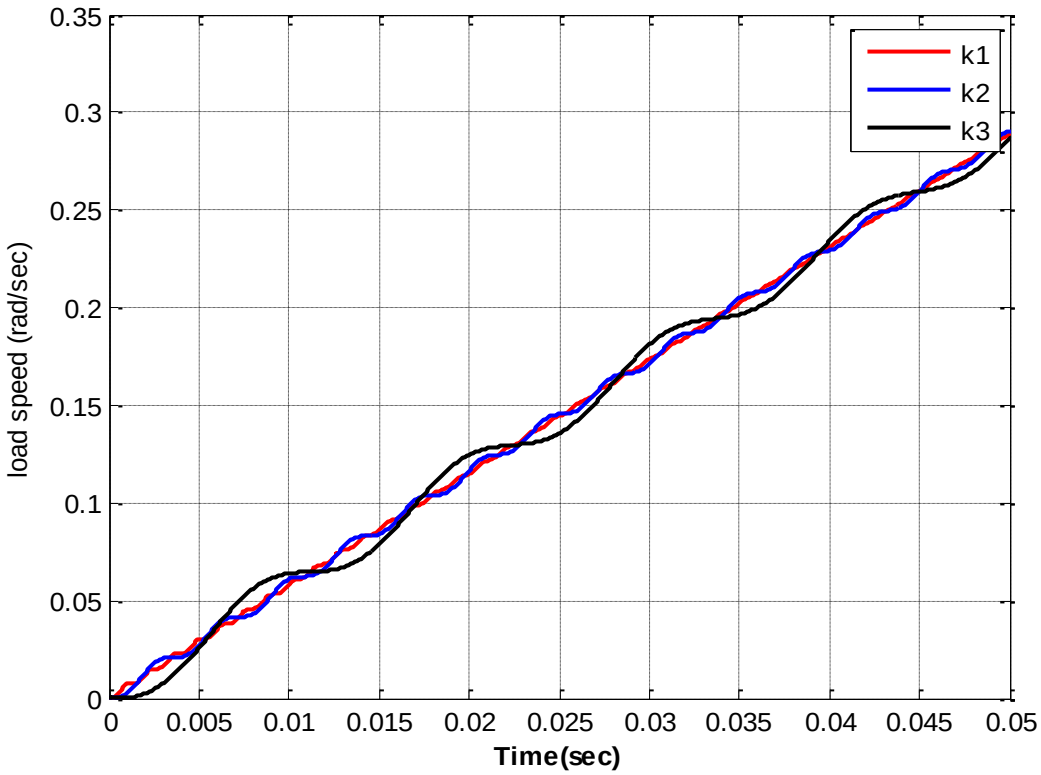

Figure 5-26 Matlab plot for different load side stiffness values

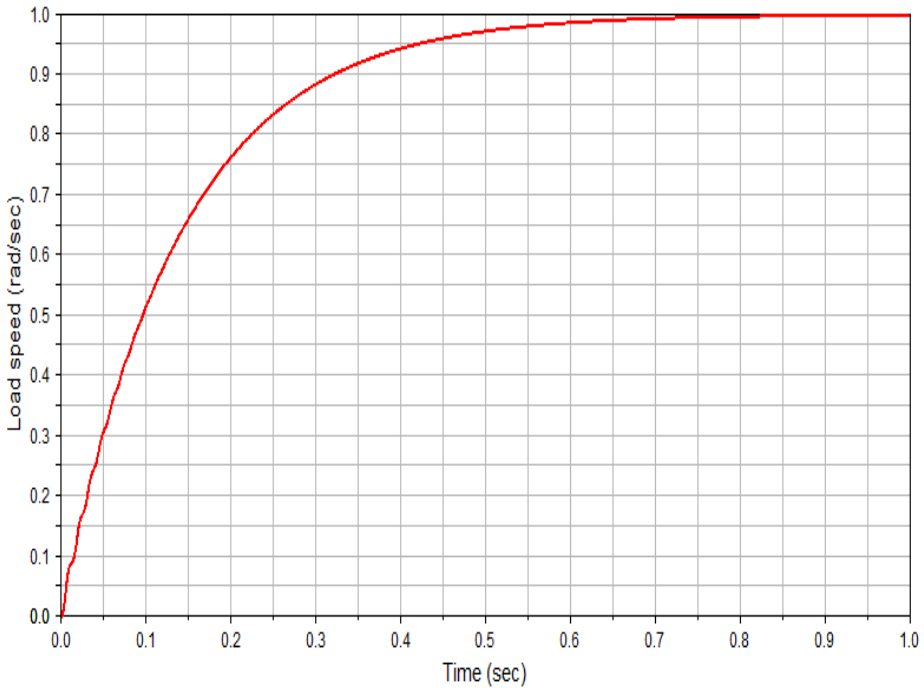

Figure 5-27 Step response of load side in MSC-Adams

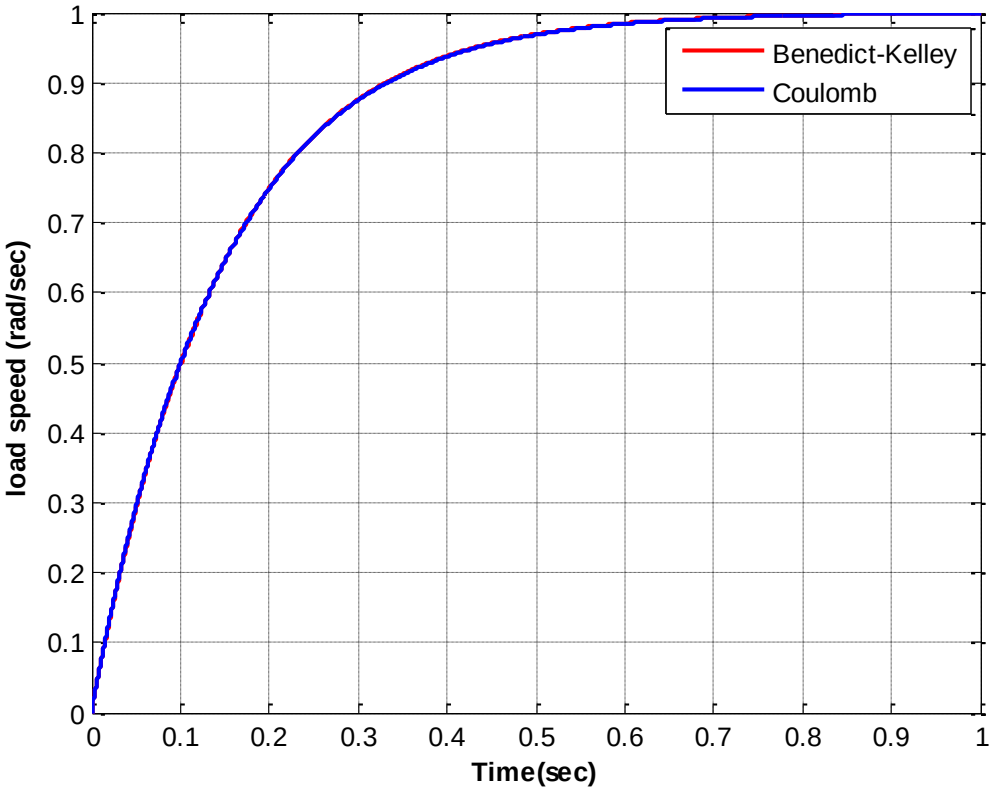

Figure 5-28 Step response of load side in Matlab

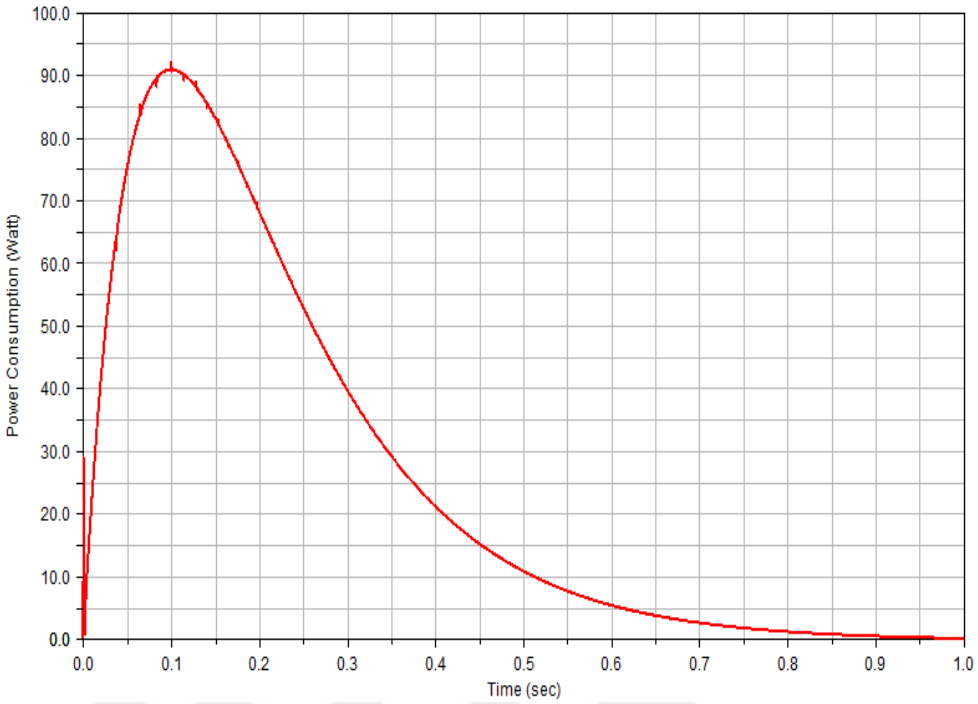

Figure 5-29 Power consumption plot in MSC-Adams

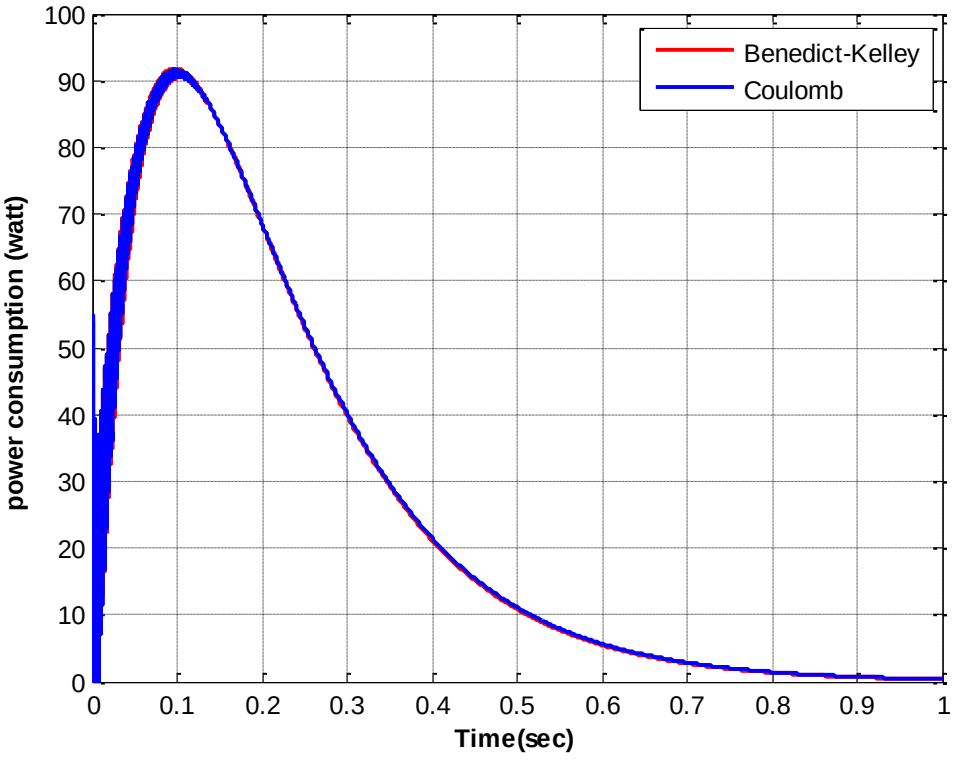

Figure 5-30 Power consumption plot in Matlab

5.8.5 Simulations with Anti-backlash Mechanism

In order to see the effect of anti-backlash mechanism on the target tracking performance, a simulation scenario is constructed. A target is assumed to have a translational sinusoidal known velocity in the form of $Vref(t) = \sin(3 \times 2\pi \times t)$.The objective of the gunner is to track this known velocity. The distance to target is also assumed to be known. This data is usually obtained via laser range finders, which is a part of the sight systems. The reference angular velocity is computed by dividing the translational target velocity by the distance to target. This reference angular velocity behaves as the input velocity, coming from the sight system.

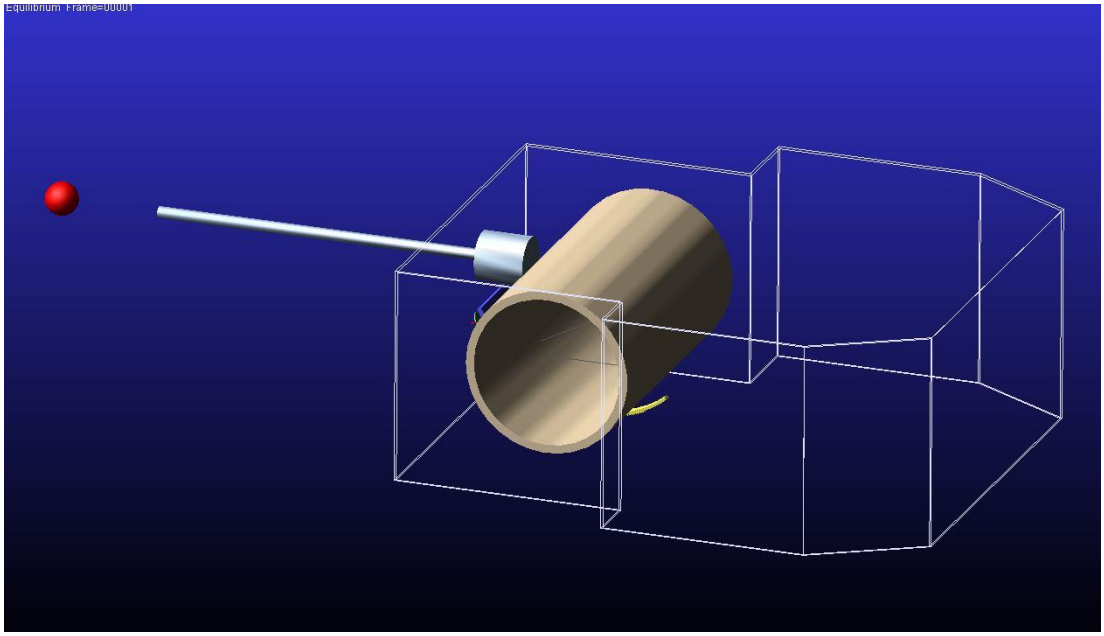

Figure 5-31 Isometric view of MSC-Adams model

The reference target velocity profile is given as in Figure 5-32.

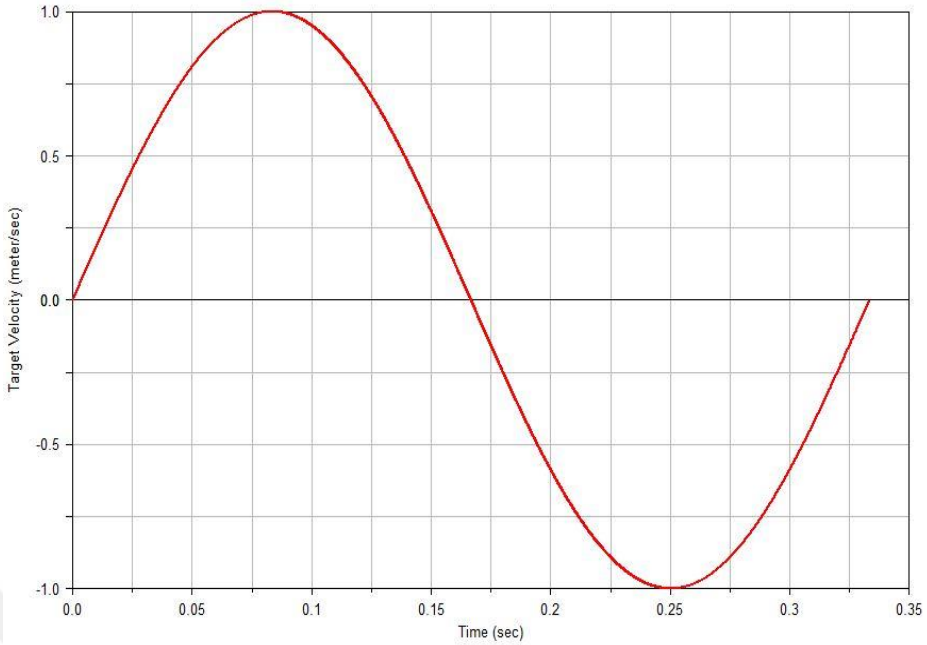

Figure 5-32 Reference target velocity

The system is simulated for different anti-backlash mechanism preload values. The tracking error and power consumption are plotted with respect to time.

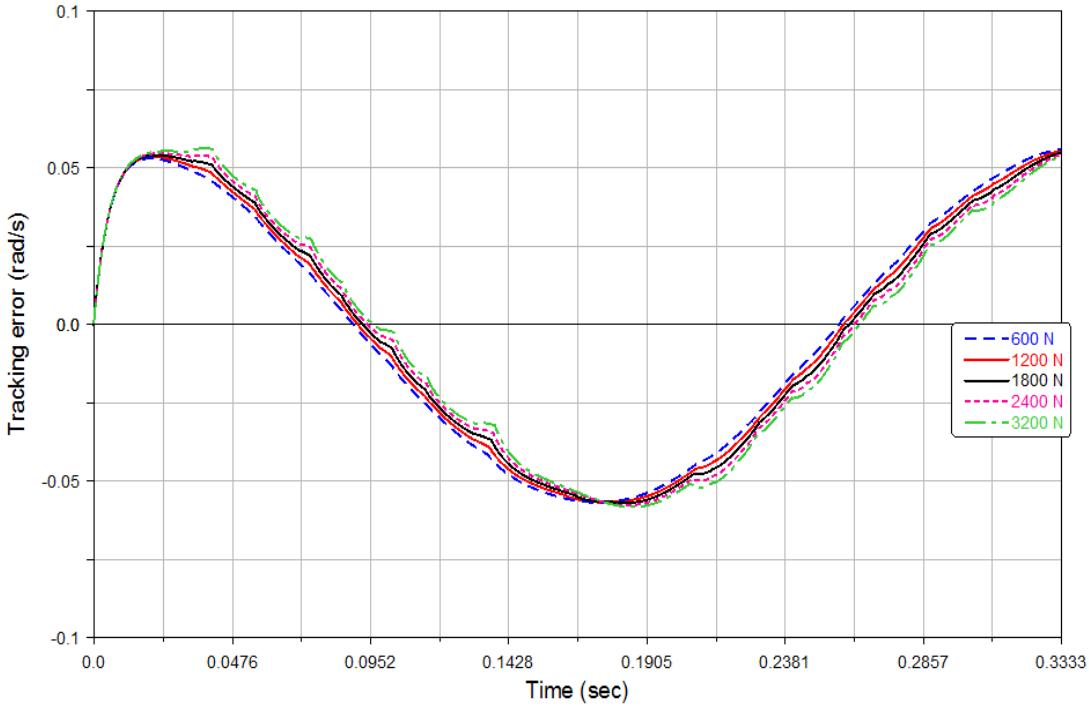

Figure 5-33 Tracking error vs. time for different anti-backlash mechanism preload values

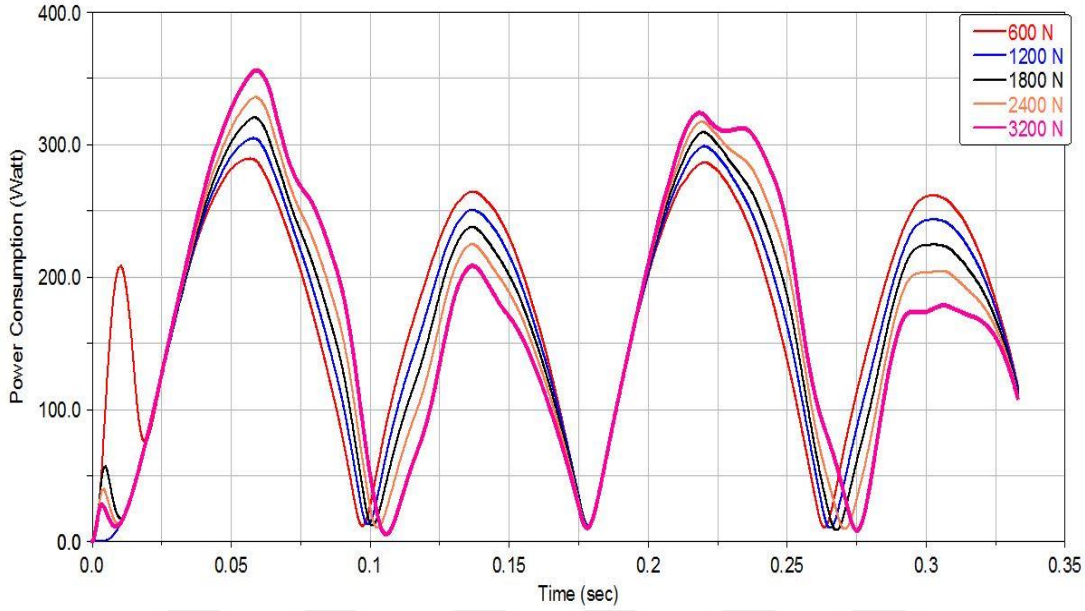

Figure 5-34 Power consumption vs. time for different anti-backlash mechanism preload values

Due to the sinusoidal nature of the input, increasing the preload has a variable effect on the tracking error as can be seen in Figure 5-33. In other words, for 600 N preload, tracking error is smaller compared to other preloads until 0.09 seconds. Then it stays larger until t = 0.15 seconds. This trend continues in a periodic manner. A similar trend can also be observed for the power consumption from the motor. Since increasing the preload increases the friction force in the gears, it also affects the consumed power. For the times, where the load side needs to accelerate, friction hinders the motion thereby increasing the power consumption of the motor to track the reference speed. However, for the deceleration period of the load, friction acts as a helping force thereby reducing the power consumption. The difference between the peaks for a given preload can be attributed to the dissipation of energy due to friction.

One important observation regarding the power consumption is that there is an optimal value for the preload if the initial power transients are to be minimized. For the 1200 N preload, the power consumption starts and keeps going as smooth however for other preloads, there is an initial jump in the power.

CHAPTER 6

CONCLUSION AND FUTURE WORK

6.1 Conclusions

The gun turrets on infantry fighting vehicles or main battle tanks must always have gear pairs in their driveline in order to satisfy the mobility requirements while keeping the motor sizes within reasonable limits. The ultimate goal of this thesis was to develop verified dynamic models of elevation axis of a gun turret. The developed model takes into account the driveline stiffnesses as well as the gear flexibilities and possible backlash. The utilized friction model for the gear mesh; that depends on lubricant viscosity, surface roughness and sliding velocities of gear teeth is believed to capture the complex dynamics more accurately. In the MSC-Adams model, a compliant adjustment type anti-backlash mechanism is simulated for the first time in the literature.

An introduction to elevation axis of a gun turret and its components is presented in chapter 2. An elementary dynamic model is constructed with driveline compliances and damping. The equations of motions are obtained by using Lagrange method. Then, an independent model in which the load side is reflected to the motor side is developed. Equivalent stiffnesses and equivalent inertia concepts are explained. The importance of the drive-line stiffness and how it changes the resonance values for the open loop system is shown. The transfer functions of interest are obtained by the state space model and open loop Bode plots are constructed. This enables to get a rough idea about the open loop bandwidth and natural frequencies of the system. Anti-resonance and resonance phenomenon are demonstrated. It is mathematically shown the reflection to motor side approximation is valid only at relatively low-moderate frequencies. It can be stated that when the system is excited at higher frequencies; the simplified and reflected model does not give accurate results.

In Chapter 3; mesh stiffness and damping characteristics of a gear pair are explained thoroughly. Gear deformations due to Hertzian, bending, shear and foundation deformations of a gear tooth are obtained as functions of the roll angle. The variation of these deflections as the point of contact travels along the line of action is investigated. To obtain Hertzian deformations, various cylinder to cylinder contact models are investigated for gear to gear contact. It is concluded that different Hertzian models yield significantly different results. It is also concluded that deflection due to Hertzian contact is small compared to the other deflections. The average combined mesh stiffness can be computed either from the ISO standard, a curve fit formulation or analytical functions derived from cantilever trapezoidal beam approximation of gear tooth. All of the formulations predict values with the same order of magnitude for the combined mesh stiffness. Considering the complexity of the involute gear profile, accurate estimation of mesh stiffness is an important work. It is observed that the trapezoidal beam approximation and the ISO standard predict similar values for the gear pair given/analyzed in the thesis.

Chapter 4 starts with the derivation of the equations of motion for a fixed center distance gear pair. The piecewise continuous differential equations of motions that can capture the front side contact, possible backlash and backside contact are embedded into MATLAB-Simulink model. Then the same dynamic model for the fixed gear pair is constructed in MSC-Adams environment. Similarity of the results with the literature demonstrate the fact that gear dynamics can be captured accurately in MSC-Adams provided that the correct contact parameters and appropriate resolution in solution time step is selected. It was shown that dynamic modeling of friction in gears is very complicated and there are numerous modes that yield different equations of motion depending on the direction of the rotation, front-side or back-side contact and single or double tooth contact. The developed dynamic model includes these different scenarios. Furthermore, in order to compute the variation of dynamic force on a single gear tooth, a different dynamic model has been developed and verified with the existing literature. The most important conclusion of chapter 4 is that possible backlash in gear drives may cause tooth separation due to gear teeth impact; which results in a non-smooth dynamic response. The chapter is ended by investigating the friction coefficient at different gear rotational speed values and it

was shown that as the gear speed is increased, the average friction coefficient decreases.

In Chapter 5; the complete elevation axis of a one man medium caliber turret is modeled by using three different methods. The first method is the derived state space representation of the system that includes gear flexibilities but no backlash. The second model is the improved Simulink model explained in chapter 4 which can take into account backlash as well. The third method is the multibody dynamics model which is constructed in MSC-Adams. The compliant adjustment type anti-backlash mechanism is included in the final model. The results are divided into two major categories; namely open loop simulation results and closed loop simulation results. Firstly, effect of different friction models on the overall system response is investigated and different models predicted different load responses for a constant torque. It can be concluded that Coulomb friction model is sufficient enough as a friction model when the system is excited by a constant torque at low to moderate speeds. However, at high speed operation, the difference between Benedict-Kelley and Coulomb frictions become more dominant. Secondly the effect of drive-line stiffness on the load speed is investigated. It was concluded that, the more compliant system exhibits higher amplitude and lower frequency oscillations.

MATLAB-SISO tool is used to design a proportional controller via root locus method for target tracking purposes. The required transfer functions are extracted from the four d.o.f. state space model. Adams Controls toolkit is used for controlling the gun velocity in MSC-Adams. For a step input, angular velocity of the gun for different backlash values are plotted. The effect of backlash, which is non-smooth transients on the gun velocity while tracking a target, is demonstrated for no backlash and backlash cases. The motor torque transient spikes are also shown when backlash is present. The simulation results with the realistic friction model and the simple Coulomb friction are plotted. The instantaneous power consumption of the motor shows slight differences for the two models. All of the simulations are also performed in MSC-Adams as a verification tool to the MATLAB models. Chapter 5 is ended with the integration of the anti-backlash mechanism. The tracking error and power consumption from the motor under different anti-backlash preload values are

plotted. It is concluded that for a sinusoidal reference input, there exists a preload value which minimizes the power consumption transients.

6.2 Future Work

In the light of the conducted work, the backlash and its effect on system instability can be investigated in a more rigorous fashion by construction of the piecewise continuous state space models. The possible backlash values that make the plant instable can be determined. Furthermore, the controllability matrix can be constructed as a function of backlash in order to calculate the maximum allowable backlash value.

The variable center distance gear pairs in the anti-backlash mechanism can also be constructed analytically. This analytical model should capture the complex contact phenomenon among gear pairs which does not follow the rules of conventional fixed center distance gear pair.

The dynamic model can be enhanced by taking into account the flexibility of the gun barrel, and inclusion of stick slip like friction models for the bearings in the rotor. The radial flexibilities of the bearings can also be included in the dynamic model as well.

REFERENCES

[1] KARAYUMAK T. Modeling and stabilization control of a main battle tank. PhD Thesis, Middle East Technical University, 2011

[2] Elements of Metric Gear Technology. Retrieved 31.12.2015, from https://www.sdp-si.com/D805/D805_PDFS/Technical/8050T119.pdf

[3] HALE L.C. and SLOCUM A.H. Design of anti-backlash transmissions for precision position controlled systems. Journal of American Society for Precision Engineering, 16,4:244-258, 1994

[4] PURDY D. Main battle tank stabilization ratio enhancement using hull rate feed-forward. Journal of Battlefield Technologies Vol.1 No.2, 1998

[5] PURDY D. Comparison of balance and out of balance main battle tank armaments. Journal of Shock and Vibration, 8:167-174, 2001

[6] PURDY D. Theoretical investigation into the modeling of a flexible beam with drive-line compliance. Proceedings of the Institution of Mechanical Engineers, Part C: Journal of Mechanical Engineering Science, 216:813-829, 2002

[7] AFACAN K. Modeling and Control of a Stabilization System. MSc Thesis, Middle East Technical University, 2004

[8] Methods to Minimize Gear Backlash, Retrieved 31.12.2015, from http://machinedesign.com/motion-control/methods-minimize-gear-backlash

[9] US Patent, US5085619 A, 04.02.1992

[10] US Patent, US2893257 A, 07.07.1959

[11] AGMA 2000-A.88, *Tolerances and Measuring Methods for Unassembled Spur and Helical Gears*, American National Standard, 2000

[12] YUMRUKÇAL Z. Dynamic modeling of high precision servo systems with gear backlash. MSc Thesis, Middle East Technical University, 2013

[13] Harmonic drive strain wave gears, Retrieved 31.12.2015, from http://harmonicdrive.de/en/technology/harmonic-drive-strain-wave-gears/

[14] OZGOREN K. ME 502 Advanced Dynamics Lecture Notes, Middle East Technical University, 2012

[15] SONG H. Effect of sliding friction on spur and helical gear dynamics and vibro-acoustics. PhD Thesis, The Ohio State University, 2008

[16] ARIKAN M.A.S. Computer aided dynamic modeling of spur gears. PhD Thesis, Middle East Technical University, 1986

[17] YANG D.C.H. and SUN Z.S. A Rotary model for spur gear dynamics. ASME Journal of Mechanisms, Transmissions, and Automation in Design,107:529-535,1985

[18] SHING T.K. Dynamics and control of geared servomechanisms with backlash and friction. PhD Thesis, University of Maryland, 1994

[19] CHAARI F., FAKHFAKH T., and HADDAR M. Analytical modeling of spur gear tooth crack and influence on gear mesh stiffness. European Journal of Mechanics A/Solids, 28:461-468, 2009

[20] PAREY A., BADAOUI M.E., GUILLET F., TANDON N. Dynamic modeling of spur gear pair and application of empirical mode decomposition-based

statistical analysis for early detection of localized tooth defect. Journal of Sound and Vibration, 294: 547-561,2006

[21] PEREIRA C.M., RAMALHO A.L. and AMBROSIO J.A. A critical overview of internal and external cylinder contact force models, Nonlinear Dynamics, Springer, 63:681-697, 2010

[22] ARIKAN M.A.S. Determination of addendum modification coefficients for spur gears operating at non-standard center distances. Design Engineering Technical Conferences and Computers and Information in Engineering Conference ASME, 2003

[23] RICHARDSON H. Static and dynamic load, stress and deflection cycles in spur gear systems. PhD Thesis, Massachusetts Institute of Technology, 1956

[24] KUANG J., YANG Y. An estimate of mesh stiffness and load sharing ratio of a spur gear pair. Advancing Power Transmission into the 21st century, 1-9,1992.

[25] ISO 6336-1. Calculation of load capacity of spur and helical gears Part1: Basic principles, introduction and general influence factors, 1996

[26] LANKARANI H.M. and NIKRAVESH P.E. A contact force model with hysteresis damping for impact analysis of multi-body systems. Journal of Mechanical Design 112:369-376, 1990

[27] AZAR R. C. and CROSSLEY F. R. E. Digital simulation of impact phenomenon in spur gear systems. ASME Journal of Engineering for Industry, 99(8):513-518, 1977

[28] DUBOWSKY S. and FREUDENSTEIN F. Dynamic analysis of mechanical systems with clearance Part 1 and 2.ASME Journal of Engineering for Industry 305-316, 1971

[29] CILOGLU C., ARIKAN M.A.S and EREN O. Effect of radial run-out on the transient response of a spur gear pair with backlash. Applied Mechanics and Materials, 799: 610-617, 2015

[30] MSC Adams-View User Manual, 2013

[31] AGMA 925-A03. Effect of Lubrication on Gear Surface Distress, 2003

APPENDIX A

ADAMS VIEW-FLEX SOLUTIONS

Adams View-Flex module which is an add-on package of MSC-Adams enables flexible solutions under dynamic loads during a simulation. The package is compatible with most of the major commercial finite element packages such as MSC-Nastran, Ansys or Abaqus. The user creates a file called modal neutral file (mnf) in one of those programs. This file contains the mesh geometry and boundary conditions of the imported geometry.

MSC-Nastran is used for creation of the mnf file in this study.The solid geometry that is intended to be flexible is then imported into Nastran for preprocessing. The pinion and sector gear are meshed with tetrahedral elements as shown in Figure A.1 and Figure A.2 respectively.

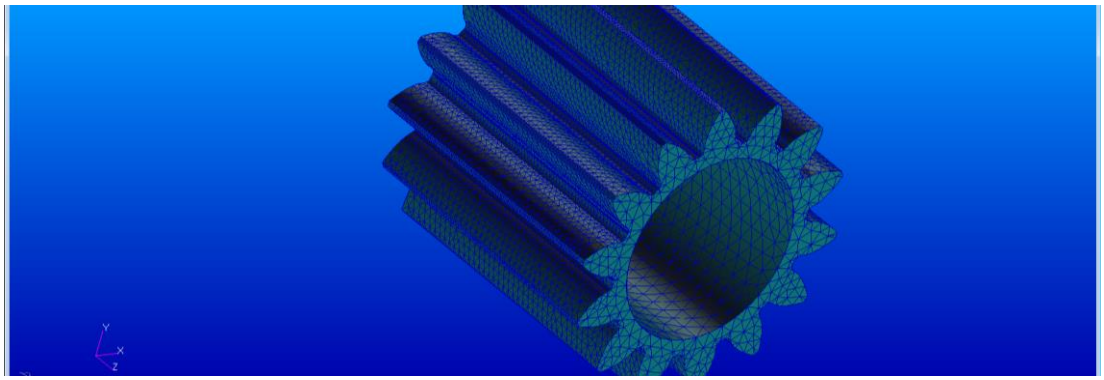

Figure A.1 Pinion meshing in MSC-Nastran

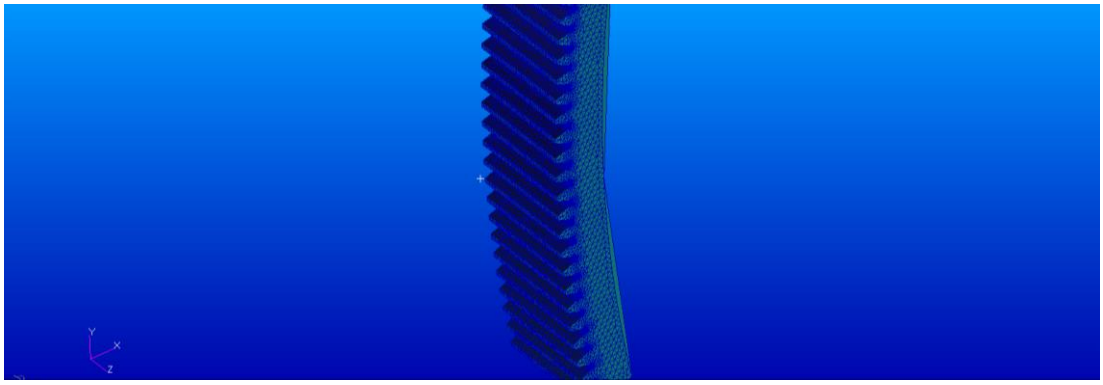

Figure A.2 Sector gear meshing in MSC-Nastran

The cylindrical surfaces of the pinion and the cylindrical inner surface of the sector gear are taken as fixed and the boundary condition is applied as RBE2 elements. The prepared model is sent into MSC-Patran for creation of the mnf file. Following the generation of the mnf file, the rigid parts are replaced with the corresponding flexible parts in MSC Adams.

Different mode shapes corresponding to the different modes can be inspected when the gears are modeled flexible. One example mode of the pinion shaft is given in Figure A.3 .

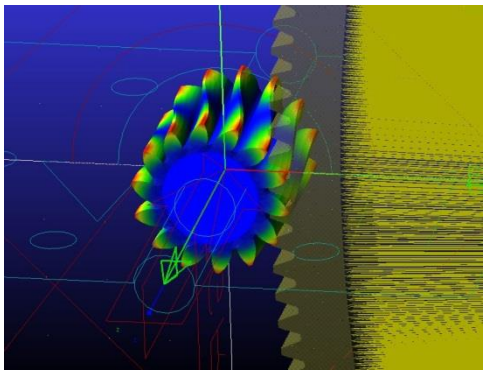

Figure A.3 Flexible pinion in MSC Adams

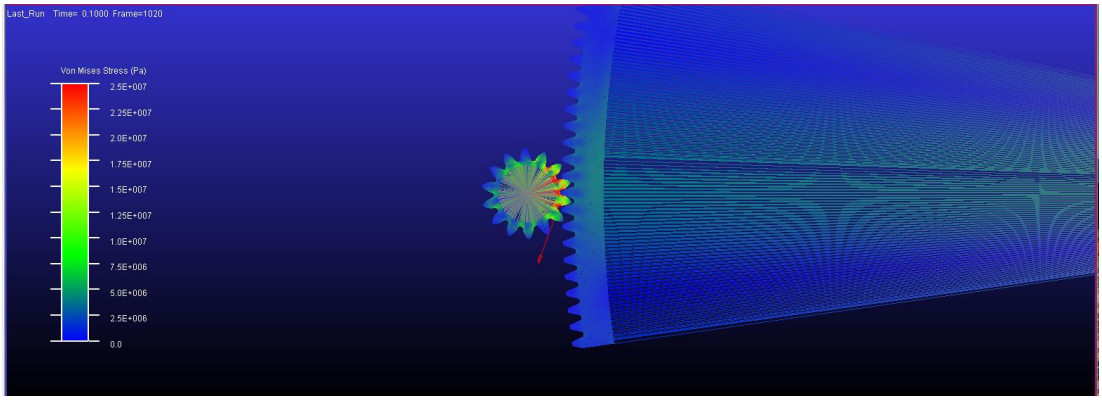

Figure A.4 Screenshot of the flexible gears simulation

Two different types of simulations are run for analyzing the differences between modeling the gears via Adams View Flex module and Adams contact. The first scenario is to apply a constant torque of 10 Nm to the pinion. The load side angular velocity is observed for flexible and normal gear pairs. The second simulation is applying sinusoidal torque to the pinion in the form of $T_m = 10\sin(3 \times 2\pi \times time)$.

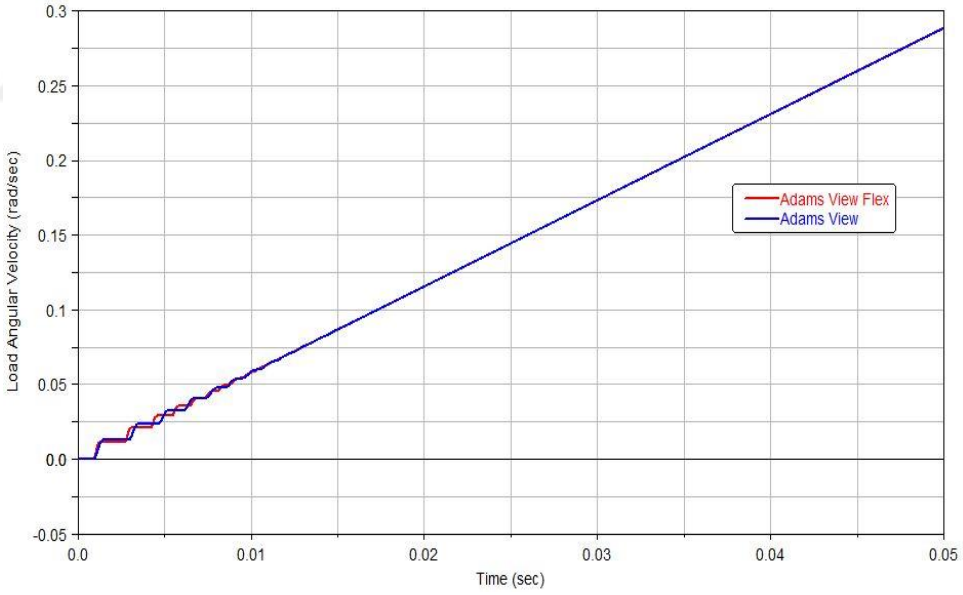

Figure A.5 Comparison of Adams View Flex and Adams View for constant torque

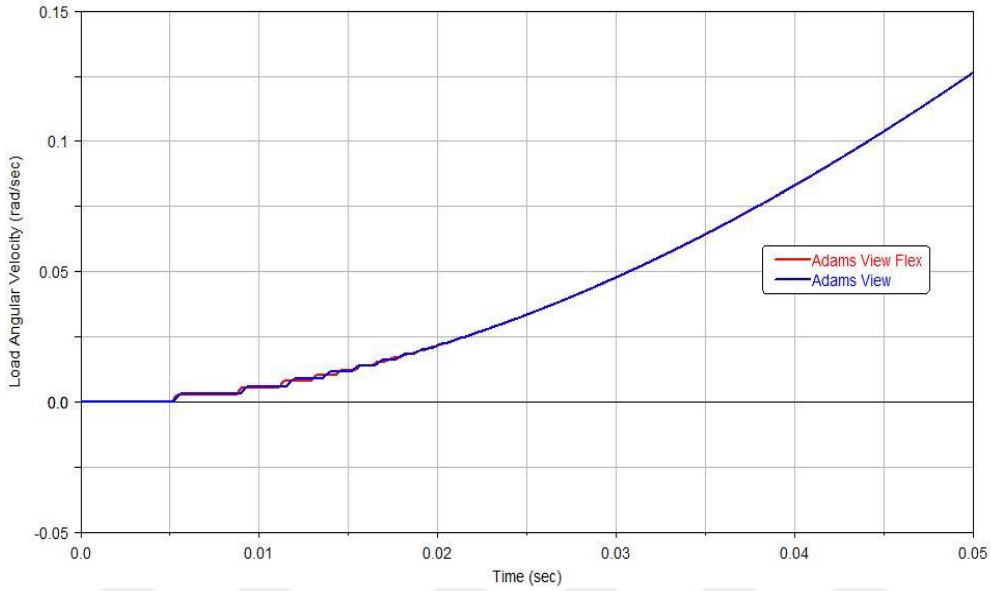

Figure A.6 Comparison of Adams View Flex and Adams View for sinusoidal torque

Since the differences between two models are small, the solution obtained by contact algorithm is used for the MSC-Adams solutions. Utilization of this module will be beneficial when the stresses in the gears are of concern. Under the realistic dynamic loading, the user can extract the predicted Von Mises stress values and design the gears accordingly.

APPENDIX B

SAMPLE MATLAB CODES

4 d.o.f. state space model

```
clc

clear all

close all

Im = 3*10^-4;

I1 = 3*10^-4;

I2 = 0.3;

IL = 49.7;

km = 3*10^4;

kL = 2.5*10^7;

cm = 0.3;

cL = 10;

m = 1.5*10^-3;

N1 = 14;

N2 = 408;

phi = 20;

Rb1 = m*N1/2*cosd(phi);

Rb2 = m*N2/2*cosd(phi);

kg = 5.5*10^8;

cg = 2300;

n = 408/14;

M = [Im 0 0 0;0 I1 0 0;0 0 I2 0;0 0 0 IL];

C = [cm -cm 0 0;-cm (cm+cg*Rb1^2) -cg*Rb1*Rb2 0; 0 -cg*Rb1*Rb2
cL+cg*Rb2^2 -cL;0 0 -cL cL];
```

```
K = [km -km 0 0;-km (km+kg*Rb1^2) -kg*Rb1*Rb2 0;0 -kg*Rb1*Rb2
kL+kg*Rb2^2 -kL;0 0 -kL kL];

Id = [1;0;0;0];

A = [zeros(4,4) eye(4,4);-M^-1*K -M^-1*C];

B = [zeros(4,1);M^-1*Id];

Css = [0 0 0 0 0 0 0 1];

D = 0;

[b1,a1] = ss2tf(A,B,Css,D);

G1 = tf(b1,a1);

bode(G1,{0.1,50000})

Css = [0 0 0 0 1 0 0 0];

D = 0;

[b2,a2] = ss2tf(A,B,Css,D);

G2 = tf(b2,a2);

figure(2)

bode(n*G1/G2,{0.1,50000})

nat_freq = [1/(2*pi)]*sqrt(eig(M^-1*K))
```

Calculation of gear tooth deformations

```
clc

clear all

close all

m=1.5*10^-3;

Np= 14;

Ng= 408;

xp = 0.5;

xg = -0.5;

E = 2.068*10^11;

G = 70*10^9;

nu = 0.3;

f = 0.0254;

Fn = 1;

phi_c = 20*(pi/180);

a_c = 1*m;

b_c = 1.25*m;

% SAHIR ARIKAN NOTATION

d = m*Np;

D = m*Ng;

do_s = m*Np+2*a_c;

Do_s = m*Ng+2*a_c;

dr_s = m*Np-2*b_c;

Dr_s = m*Ng-2*b_c;


d_b = m*Np*cos(phi_c);

D_b = m*Ng*cos(phi_c);
```

```
pb = pi*m*cos(phi_c);    %base pitch

do_m = do_s + 2*m*xp;

Do_m = Do_s+ 2*m*xg;

dr_m = do_m- 2*2.25*m;

Dr_m = Do_m- 2*2.25*m;

%disp(Do_m)

%% PHD THESIS NOTATION

%% base diameters
rb1 = d_b/2;

rb2 = D_b/2;

%% tip diameters
ra1 = do_m/2;

ra2 = Do_m/2;

%% root diameters
rd1 = dr_m/2;

rd2 = Dr_m/2;

%% CONTACT LOCATIONS
AB = (rb1+rb2)*tan(phi_c);

AC = AB -  sqrt(ra2^2-rb2^2);

AD = sqrt(ra1^2-rb1^2);

AE = AD - pb;

AF = AC + pb;

CE = AE - AC;



        if (dr_m < d_b)

  hb1 = rb1 - rd1;

  ha1 = ra1 - rd1;

        else

  hb1 = 0;
```

```
  ha1 = ra1-rd1;
        end
        if (Dr_m < D_b)
  hb2 = rb2 - rd2;
  ha2 = ra2 - rd2;
        else
  hb2 = 0;
  ha2 = ra2-rd2;
        end
rp1 = d/2;
rp2 = D/2;
%% CIRCULAR TOOTH THICKNESS AT PITCH DIAMETER
tp1 = (pi*m/2)+2*m*xp*tan(phi_c);
tp2 = (pi*m/2)+2*m*xg*tan(phi_c);
%% ROTATION ANGLES ALPHAS
phi_m_C = atan(AC/rb1);
alfa_11_C = tan(phi_m_C);
phi_m_E = atan(AE/rb1);
alfa_11_E = tan(phi_m_E);
theta_1_E = alfa_11_E-AC/rb1;
phi_m_F = atan(AF/rb1);
alfa_11_F = tan(phi_m_F);
theta_1_F = alfa_11_F-AC/rb1;
phi_m_D = acos(rb1/ra1);
alfa_11_D = tan(phi_m_D);
theta_1_D = alfa_11_D-AC/rb1;
```

```
n = theta_1_D/500;

theta1 = 0:0.001:theta_1_D;

alfa11 = theta1+AC/rb1;

alfa12 = alfa11 + pb/rb1;

alfa21 = (AB-alfa11*rb1)/rb2;

alfa22 = alfa21-pb/rb2;

%% CALCULATION OF HCJ



phi_m11 = atan(alfa11);

gama_m11 = 0.5*(tp1/rp1+2*((tan(phi_c)-phi_c)-(tan(phi_m11)-
phi_m11)));

phi_m12 = atan(alfa12);

gama_m12 = 0.5*(tp1/rp1+2*((tan(phi_c)-phi_c)-(tan(phi_m12)-
phi_m12)));

phi_m21 = atan(alfa21);

gama_m21 = 0.5*(tp2/rp2+2*((tan(phi_c)-phi_c)-(tan(phi_m21)-
phi_m21)));

phi_m22 = atan(alfa22);

gama_m22 = 0.5*(tp2/rp2+2*((tan(phi_c)-phi_c)-(tan(phi_m22)-
phi_m22)));




hc11 = (cos(gama_m11)./cos(atan(alfa11))-1)*rb1+hb1;

hc12 = (cos(gama_m12)./cos(phi_m12)-1)*rb1+hb1;

if rb2<rd2

hc21 = ((rb2*cos(gama_m21)./cos(phi_m21))-rd2);

else

hc21 = (cos(gama_m21)./cos(phi_m21)-1)*rb2+hb2;

end
```

```
hc22 = (cos(gama_m22)./cos(atan(alfa22))-1)*rb2+hb2;

phi_ded = acos(rb2/rd2);
dummy = tan(phi_ded)-phi_ded;

%% CALCULATION OF TBJ TAJ W


tb1 = 3.466*10^-3;

tb2 = 3.523*10^-3;

beta1 = acos(rb1/ra1);

beta2 = acos(rb2/ra2);

involute_phi_c = tan(phi_c)-phi_c;

involute_beta1 = tan(beta1)-beta1;

involute_beta2 = tan(beta2)-beta2;

ta1 = ra1*(tp1/rp1+2*(involute_phi_c-involute_beta1));

ta2 = ra2*(tp2/rp2+2*(involute_phi_c-involute_beta2));


w1 = (ha1*tb1-hb1*ta1)/(tb1-ta1);

w2 = (ha2*tb2-hb2*ta2)/(tb2-ta2);

% DEFLECTION CALCUATIONS


%% SHEAR DEFORMATION

delta_shear11 = ((1.2*Fn*cos(phi_c)^2)/(G*f*tb1))*(hb1+(w1-
hb1)*log((w1-hb1)./(w1-hc11)));

delta_shear12 = ((1.2*Fn*cos(phi_c)^2)/(G*f*tb1))*(hb1+(w1-
hb1)*log((w1-hb1)./(w1-hc12)));



delta_shear21 = ((1.2*Fn*cos(phi_c)^2)/(G*f*tb2))*(hb2+(w2-
hb2)*log((w2-hb2)./(w2-hc21)));
```

```
delta_shear22 = ((1.2*Fn*cos(phi_c)^2)/(G*f*tb2))*(hb2+(w2-
hb2)*log((w2-hb2)./(w2-hc22)));


%% HERTZIAN DEFORMATION

        delta_h = (4*Fn*(1-nu^2))/(pi*E*f);

        delta_h_m = zeros(length(theta1),1);

        delta_h1 = delta_h+delta_h_m;

        delta_h2 = delta_h+delta_h_m;


%% BENDING BP

        FIRST_TERM11 = 12*Fn*(cos(phi_c)^2)*hb1*(hc11.^2+hb1^2/3-
hc11*hb1)/(E*f*tb1^3);


        FIRST_TERM21 = 12*Fn*(cos(phi_c)^2)*hb2*(hc21.^2+hb2^2/3-
hc21*hb2)/(E*f*tb2^3);


        SECOND_TERM11 = (6*Fn*(cos(phi_c)^2)*(w1-
hb1)^3)/(E*f*tb1^3);


        SECOND_TERM21 = (6*Fn*(cos(phi_c)^2)*(w2-
hb2)^3)/(E*f*tb2^3);


        THIRD_TERM11  = ((w1-hc11)/(w1-hb1)).*(4-(w1-hc11)/(w1-
hb1))-2*log((w1-hc11)/(w1-hb1))-3;


        THIRD_TERM21  = ((w2-hc21)/(w2-hb2)).*(4-(w2-hc21)/(w2-
hb2))-2*log((w2-hc21)/(w2-hb2))-3;



delta_bp11 = FIRST_TERM11+SECOND_TERM11*THIRD_TERM11;


delta_bp21 = FIRST_TERM21+SECOND_TERM21*THIRD_TERM21;


%% BENDING BN

constant1=(3*Fn*cos(phi_c)*sin(phi_c))/(E*f*tb1^2);

constant2=(3*Fn*cos(phi_c)*sin(phi_c))/(E*f*tb2^2);
```

```
FIRST_TERMBN11 = hb1*(hb1-2*hc11).*(w1-hc11)/(w1-hb1);

FIRST_TERMBN12 = hb1*(hb1-2*hc12).*(w1-hc12)/(w1-hb1);

FIRST_TERMBN21 = hb2*(hb2-2*hc21).*(w2-hc21)/(w2-hb2);

FIRST_TERMBN22 = hb2*(hb2-2*hc22).*(w2-hc22)/(w2-hb2);

SECOND_TERMBN11 = (hc11-hb1).^2;

SECOND_TERMBN12 = (hc12-hb1).^2;

SECOND_TERMBN21 = (hc21-hb2).^2;

SECOND_TERMBN22 = (hc22-hb2).^2;

delta_bn11 = constant1*(FIRST_TERMBN11-SECOND_TERMBN11);

delta_bn12 = constant1*(FIRST_TERMBN12-SECOND_TERMBN12);

delta_bn21 = constant2*(FIRST_TERMBN21-SECOND_TERMBN21);

delta_bn22 = constant2*(FIRST_TERMBN22-SECOND_TERMBN22);

%% FOUNDATION DEFLECTION

delta_f11 = (24*Fn*cos(phi_c)^2*hc11.^2)/(pi*E*f*tb1^2);

delta_f12 = (24*Fn*cos(phi_c)^2*hc12.^2)/(pi*E*f*tb1^2);

delta_f21 = (24*Fn*cos(phi_c)^2*hc21.^2)/(pi*E*f*tb2^2);

delta_f22 = (24*Fn*cos(phi_c)^2*hc22.^2)/(pi*E*f*tb2^2);



delta_total_11 = delta_f11+delta_bn11+delta_bp11+delta_shear11+
delta_h2';

delta_total_21 = delta_f21+delta_bn21+delta_bp21+delta_shear21+
delta_h2';

k_11 = Fn./delta_total_11;

k_21 = Fn./delta_total_21;

hold on
grid on
 plot(theta1,delta_f11,'c')
 plot(theta1,delta_shear11,'r')
 plot(theta1,delta_bn11,'b')
 plot(theta1,delta_bp11)
 plot(theta1,delta_h,'g')
```

```
plot(theta1,delta_total_11,'LineWidth',2)

xlabel('\theta1(rad)')
ylabel('\delta_1_1')

figure(2)
hold on
grid on

 plot(theta1,delta_f21,'c','LineWidth',2)
 plot(theta1,delta_shear21,'r')
  plot(theta1,delta_bn21,'b')
  plot(theta1,delta_bp21)
  plot(theta1,delta_h,'g')
%
 plot(theta1,delta_total_21,'LineWidth',2)

xlabel('\theta1(rad)')
ylabel('k_2_1')

 jE = floor(theta_1_E/0.001);
 jF = floor(theta_1_F/0.001);

for i=1:jE;

    theta_1_CE_ar(i) = theta1(i);

    k_11dt(i) = k_11(i);

    k_21dt(i) = k_21(i);

    k_12dt(i) = k_11(i+jF);

    k_22dt(i) = k_21(i+jF);

    kdt(i) =  (k_11dt(i)* k_21dt(i))/(k_11dt(i)+k_21dt(i))+ ...
        (k_12dt(i)*k_22dt(i))/(k_12dt(i)+k_22dt(i));



    delta_shear11dt(i) = delta_shear11(i);
    delta_shear12dt(i) = delta_shear11(i+jF);

end

delta_shear1dt = delta_shear11dt+delta_shear12dt;

 figure(3)
hold on
grid on

delta11_dt = Fn./k_11dt;
delta12_dt = Fn./k_12dt;
```

```
delta1 = delta11_dt+delta12_dt;

delta21_dt = Fn./k_21dt;
delta22_dt = Fn./k_22dt;

delta2 = delta21_dt+delta22_dt;



plot( theta1,k_11,'b')
plot(theta1,k_21,'r')

xlabel('\theta1(rad)')
ylabel('Stiffness')



for i=1:jF-jE+1

    theta_1_EF_ar(i) = theta1(i+jE);

    k_11st(i) = k_11(i+jE);

    k_21st(i) = k_21(i+jE);


    kst(i) = (k_11st(i)*k_21st(i))/(k_11st(i)+k_21st(i));

    delta_bp11_st(i) = delta_bp11(i+jE);

    delta_f11_st(i) = delta_f11(i+jE);

    delta_shear11_st(i) = delta_shear11(i+jE);

end

k_eq = [kdt kst];

theta1_eq = 0:0.001:theta_1_F;

figure(4)
hold on
grid on

plot(theta1_eq,k_eq,'LineWidth',2)
xlabel('\theta_1(rad)')
ylabel('k_e_q')
```

APPENDIX C

SIMULINK SCREENSHOTS

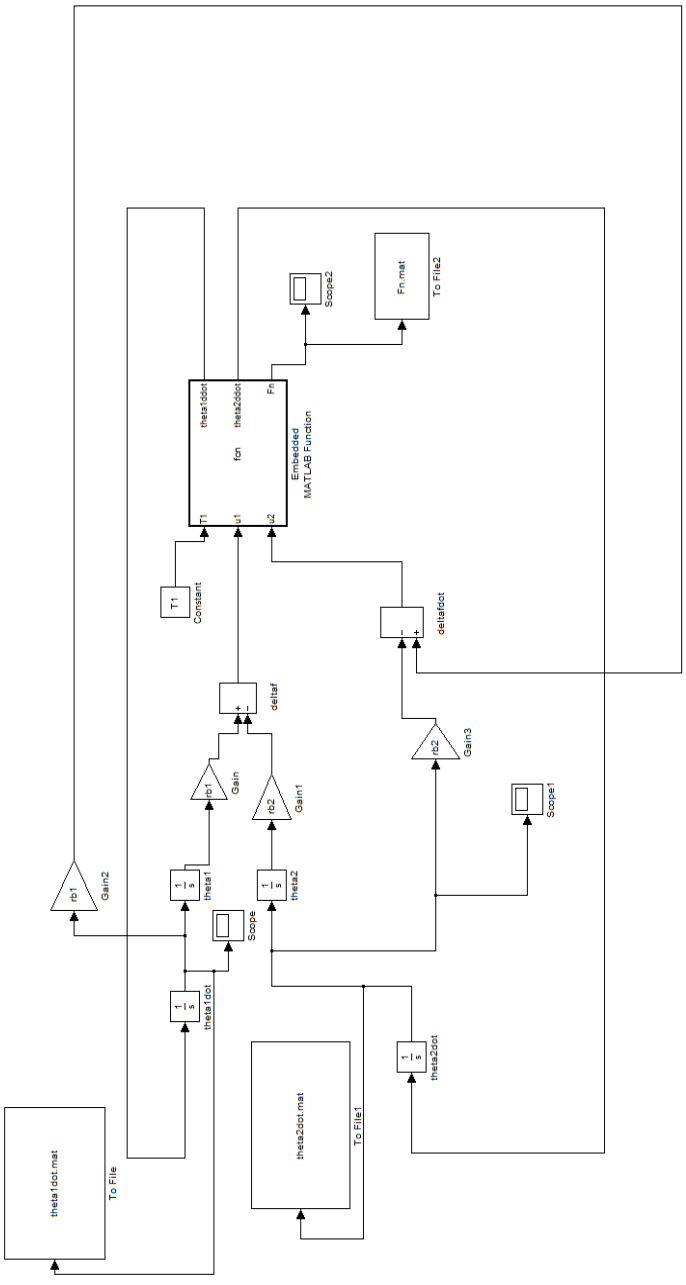

Figure C.1 Simulink model cited in section 4.3

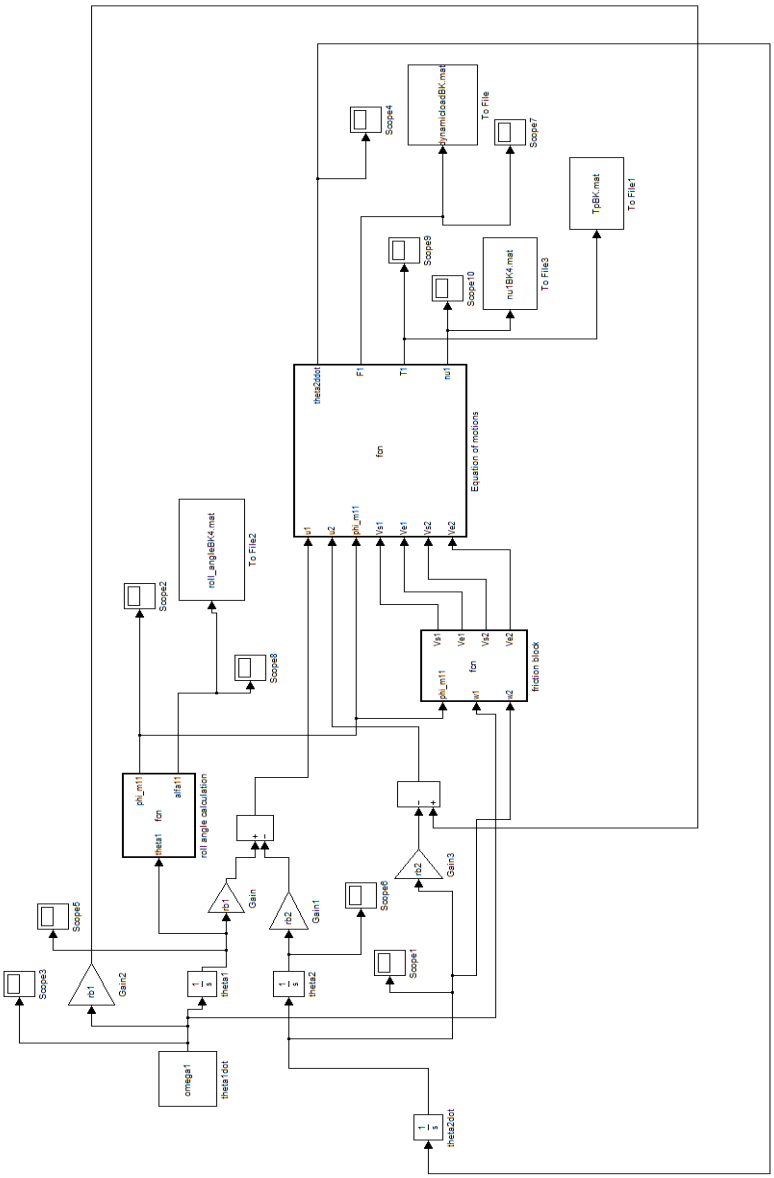

Figure C.2 Simulink model cited in section 4.6

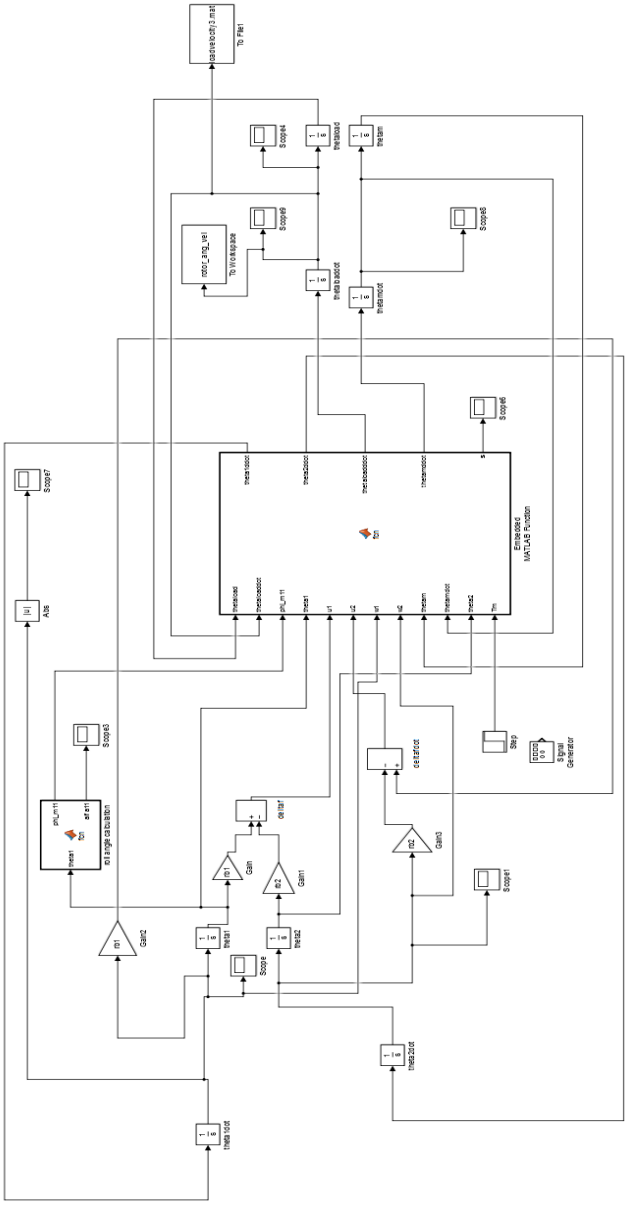

Figure C.3 Simulink model cited in section 5.2